APPENDIX B

SHEAR-MOMENT CAPACITY OF CRC BRIDGE GIRDERS SUBJECTED TO MOVING LOADS

SHEAR-MOMENT CAPACITY OF CRC BRIDGE GIRDERS SUBJECTED TO MOVING LOADS

TABLE OF CONTENTS

1.0 INTRODUCTION 1

2.0 BACKGROUND 3

2.1 SHEAR CAPACITY OF CRC BRIDGE GIRDERS 3
2.2 STRUCTURAL MODEL 3
2.3 MOVING LOAD HISTORY 6

3.0 SPECIMEN DESIGN 9

3.1 C11T16.5-B2-ML 9
3.2 C11T22-B3-ML 11
3.3 C11T22-B4-ML 11
3.4 C10T12-B2-ML 13
3.5 C11IT16-B1-ML 15

4.0 TESTING APPARATUS DESIGN 21

5.0 TESTING PROCEDURES 29

5.1 LOADING PROTOCOL 29
5.2 C11T22-B3-ML 30
5.3 C11T22-B4-ML 35
5.4 C11T16.5-B2-ML 39
5.5 C10T16-B2-ML 42
5.6 C11IT16-B1-ML 45
5.7 INSTRUMENTATION 46

6.0 TEST RESULTS AND DISCUSSION 49

6.1 CRACK PATTERNS 49
6.2 PREDICTED MOVING LOAD SHEAR-MOMENT CAPACITY 53
6.2.1 C11T22-B3-ML 54
6.2.2 C11T22-B4-ML 59
6.2.3 C11T16.5-B2-ML 66
6.2.4 C10T12-B2-ML 73
6.2.5 C11IT16-B1-ML 79
6.3 COMPARISON OF MOVING LOAD AND STATIONARY LOAD SPECIMEN CAPACITIES 90
6.4 CRACK MOTION 92
6.5 STIRRUP COMPRESSION DUE TO MOVING LOADS 94

7.0 CONCLUSIONS 97

8.0 REFERENCES 99

LIST OF TABLES

Table 3.1: Beam cross-sectional and material properties.....9
Table 6.1: Statistical analysis of moving load shear-moment capacities. The ratio of peak applied shear to predicted shear was compared for five previously tested monotonic specimens, the moving load control specimen(C11IT16-B1-ML) and three moving load specimens using Response 2000™, MCFT and ACI 318-02.....91

LIST OF FIGURES

Figure 1.1: Typical crack patterns measured in (a) a laboratory specimen with stationary load and fixed shear-to-moment ratio and (b) an existing girder from ODOT Bridge No. 08175N, Spores Bridge, subjected to moving loads and constantly varying shear-to-moment ratios. The cracks in the existing bridge girder tend to be more vertically oriented and more widely spaced along the girder length. 2
Figure 2.1: Springfield Bridge, ODOT Bridge No. 08051, (a) vicinity map and (b) plan and elevation views. Laboratory specimens were modeled after the three-span-continuous west approach spans. 4
Figure 2.2: Plan view, elevation view and reinforcing details for the west approach spans of Springfield Bridge, ODOT Bridge No. 08051. 5
Figure 2.3: Shear-moment interactions for HL-93 truck model with 14 ft (4.27 m) axle spacing at locations near simply supported girder ends, Springfield Bridge.....7
Figure 2.4: Shear-moment interactions for HL-93 truck model with 14 ft (4.27 m) axle spacing at locations near interior continuous supports, Springfield Bridge. 7
Figure 2.5: Shear-moment interactions for HL-93 truck model with 14 ft (4.27 m) axle spacing at locations near interior continuous supports including permanent load and wearing surface (dead load) effects.....8
Figure 3.1: Dimensions and reinforcing details for Specimen C11T16.5-B2-ML 10
Figure 3.2: Dimensions and reinforcing details for Specimens C11T22-B3-ML and C11T22-B4-ML 12
Figure 3.3: Dimensions and reinforcing details for Specimen C10T12-B2-ML 14
Figure 3.4: Dimensions and reinforcing details for Specimen C11IT16-B1-ML 16
Figure 3.5: ACI 318-02 shear capacity and stirrup pressures at the simply supported ends of the Springfield Bridge (red) and Specimen C10T12-B2-ML (green). The shear capacity of the Springfield Bridge was based on the specified concrete compressive strength f'c =3300 psi. The stirrup spacing of the specimen was increased by a factor of 1.3 to approximate the shear capacity and stirrup pressures of the Springfield Bridge. In this figure, stirrup pressure is defined as (Av Fyv / s bw).....17
Figure 3.6: ACI 318-02 shear capacity and stirrup pressures over continuous supports of the Springfield Bridge (red), Specimen C11T16.5-B2-ML (blue), and Specimens C11T22-B3-ML, C11T22 B4 ML and C11IT16-B1-ML (green). The shear capacity of the Springfield Bridge was based on the specified concrete compressive strength f'c = 3300 psi. The stirrup spacing of Specimens C11T22-B3-ML, C11T22-B4-ML and C11IT16-B1-ML were increased by a factor of 1.3 to approximate the shear capacity and stirrup pressures of the Springfield Bridge. In this figure, stirrup pressure is defined as (Av Fyv / s bw). 18
Figure 3.7: ACI 318-02 moment capacities and dowel steel cross-sectional area at simply supported ends of the Springfield Bridge and Specimen C10T12-B2-ML. 18
Figure 3.8: ACI 318-02 moment capacities and dowel steel cross-sectional area at continuous supports of the Springfield Bridge and Specimens C11T16.5-B2-ML, C11T22-B3-ML, C11T22-B4-ML and C11IT16-B1-ML. 19

Figure 4.1: Schematic of the moving load apparatus, including horizontal rail (light blue), moving load dolly (red), support frames (purple), dead-load cylinder (orange), telescoping push-pull cylinder (grey), dead end reaction beam (yellow), reaction load cells (green) and dead-load load cell (dark blue). (a) Specimens C11T16.5-B2-ML, C11T22-B3-ML and C11T22-B4-ML were tested as cantilevered specimens. (b) Specimens C10T12-B2-ML and C11IT16-B1-ML were tested using simple supports. 22
Figure 4.2: Cantilevered Specimens C11T16.5-B2-ML, C11T22-B3-ML and C11T22-B4-ML were configured to model the shear-moment behavior of continuous girders in the Springfield Bridge. The vertical support near the center of the specimen models the dead load shear in the existing bridge at the dead load point of inflection. Note that the applied moment is zero at the cantilever tip, which approximates the combined live and dead load moments at the dead load point of inflection. The moving load dolly models a moving tire patch load. 23
Figure 4.3: Moving load apparatus with cantilever supports 24
Figure 4.4: Moving load apparatus with cantilever supports 24
Figure 4.5: Moving load apparatus with simple supports 25
Figure 4.6: Moving load dolly (red) and telescoping push-pull cylinder 26
Figure 4.7: Moving load dolly and hydraulic connections, including the *Sensotec TGE* 3000 psi rated pressure transducers (circled) that enabled closed-loop servo-hydraulic force control. 26
Figure 4.8: 500 kip load cell simulating the bent cap reaction in the Springfield Bridge. The pinned bearing allowed the specimen to rotate under load. 27
Figure 4.9: Dead load cylinder (orange) and hydraulic accumulator (arrow) used to maintain preset dead load as the beam deflected under live load. Roller bearing plate affixed to bottom of dead load cylinder to allowed flange to deflect without restriction of movement. 28
Figure 5.1: Dead load shear for an individual girder of the Springfield Bridge 29
Figure 5.2: Dead load moments for an individual girder of the Springfield Bridge. 30
Figure 5.3: Typical imposed dead and live load protocols and specimen response for (a) cantilever supports and (b) simple supports. 30
Figure 5.4: Support, loading conditions and instrumentation for Specimen C11T22-B3-ML. 31
Figure 5.5: Live load history for Specimen C11T22-B3-ML as a function of live load position and load step. 32
Figure 5.6: Dead load history for Specimen C11T22-B3-ML as a function of live load position and load step. 33
Figure 5.7: Centerline support reaction for Specimen C11T22-B3-ML as a function of live load position and load step. 34
Figure 5.8: Dead end support reaction for Specimen C11T22-B3-ML as a function of live load position and load step. 34
Figure 5.9: Corrected cantilever deflection for Specimen C11T22-B3-ML as a function of live load position and load step. 35
Figure 5.10: Support, loading conditions and instrumentation for Specimen C11T22-B4-ML 36
Figure 5.11: Live load history for Specimen C11T22-B4-ML as a function of live load position and load step. 36
Figure 5.12: Dead load history for Specimen C11T22-B4-ML as a function of live load position and load step. 37
Figure 5.13: Centerline support reaction for Specimen C11T22-B4-ML as a function of live load position and load step. 37
Figure 5.14: Dead end support reaction for Specimen C11T22-B4-ML as a function of live load position and load step. 38
Figure 5.15: Corrected cantilever deflection for Specimen C11T22-B4-ML as a function of live load and load step. 38
Figure 5.16: Supports, loading conditions and instrumentation for Specimen C11T16.5-B2-ML. 39
Figure 5.17: Live load history for Specimen C11T16.5-B2-ML as a function of live load position and load step. 40
Figure 5.18: Centerline support reaction for Specimen C11T16.5-B2-ML as a function of live load position and load step. 40
Figure 5.19: Dead end support reaction for Specimen C11T16.5-B2-ML as a function of live load position and load step. 41

Figure 5.20: Corrected cantilever deflection for Specimen C11T16.5-B2-ML as a function of live load position and load step. 41
Figure 5.21: Supports, loading conditions and instrumentation for Specimen C10T12-B2-ML. 42
Figure 5.22: Live load history for Specimen C10T12-B2-ML as a function of live load position and load step. 43
Figure 5.23: Dead load history for Specimen C10T12-B2-ML as a function of live load position and load step. 43
Figure 5.24: Left hand support reaction for Specimen C10T12-B2-ML as a function of live load position and load step. 44
Figure 5.25: Corrected centerline deflection for Specimen C10T12-B2-ML as a function of live load position and load step. 44
Figure 5.26: Support, loading conditions and instrumentation for Specimen C11IT16-B1-ML 45
Figure 5.27: Loading and centerline deflection history for Specimen C11IT16-B1-ML. 46
Figure 5.28: Exposed strain gage (red arrow) and 1 inch extensometer (blue arrow) located at a crack of interest. 47
Figure 5.29: Instrumentation of a cantilevered specimen. Displacement transducers (red arrow) measure the diagonal deformations within groups of stirrups with equal spacing. Displacement sensors (blue arrow) were also used to measure support deflections. Specimen rotations were measured using tilt meters (white arrow) 48
Figure 6.1: Support and loading conditions, instrumentation and crack map for Specimen C11IT16-B1-ML. Bold blue line denotes failure crack 50
Figure 6.2: Support and loading conditions, instrumentation and crack map for Specimen C11T22-B3-ML. Bold blue line denotes failure crack. 51
Figure 6.3: Support and loading conditions, instrumentation and crack map for Specimen C10T12-B2-ML. Bold blue line denotes failure crack. 52
Figure 6.4: Similarity of cracking patterns in (a) Specimen C11T22-B3-ML and (b) a typical continuous bridge girder (Spores Bridge, Eugene, Oregon), with red lines denoting primary diagonal cracks. 53
Figure 6.5: Shear-moment interaction diagram for Specimen C11T22-B3-ML for cut section located at face of support. 54
Figure 6.6: Shear-moment interaction diagram for Specimen C11T22-B3-ML for cut section located 1 foot from face of support. 55
Figure 6.7: Shear-moment interaction diagram for Specimen C11T22-B3-ML for cut section located 2 feet from face of support. 55
Figure 6.8: Shear-moment interaction diagram for Specimen C11T22-B3-ML for cut section located 3 feet from face of support. 56
Figure 6.9: Shear-moment interaction diagram for Specimen C11T22-B3-ML for cut section located 4 feet from face of support. 56
Figure 6.10: Shear-moment interaction diagram for Specimen C11T22-B3-ML for cut section located 5 feet from face of support. 57
Figure 6.11: Shear-moment interaction diagram for Specimen C11T22-B3-ML for cut section located 6 feet from face of support. 57
Figure 6.12: Shear-moment interaction diagram for Specimen C11T22-B3-ML for cut section located 7 feet from face of support. 58
Figure 6.13: Shear-moment interaction diagram for Specimen C11T22-B3-ML for cut section located 8 feet from face of support. 58
Figure 6.14: Support and loading conditions, instrumentation and crack map for Specimen C11T22-B4-ML. Bold blue line denotes failure crack. 60
Figure 6.15: Shear-moment interaction diagram for Specimen C11T22-B4-ML for cut section located at face of support. 61
Figure 6.16: Shear-moment interaction diagram for Specimen C11T22-B4-ML for cut section located 1 foot from face of support. 61
Figure 6.17: Shear-moment interaction diagram for Specimen C11T22-B4-ML for cut section located 2 feet from face of support. 62
Figure 6.18: Shear-moment interaction diagram for Specimen C11T22-B4-ML for cut section located 3 feet from face of support. 62

Figure 6.19 Shear-moment interaction diagram for Specimen C11T22-B4-ML for cut section located 4 feet from face of support. 63
Figure 6.20: Shear-moment interaction diagram for Specimen C11T22-B4-ML for cut section located 5 feet from face of support. 63
Figure 6.21: Shear-moment interaction diagram for Specimen C11T22-B4-ML for cut section located 6 feet from face of support. 64
Figure 6.22: Shear-moment interaction diagram for Specimen C11T22-B4-ML for cut section located 7 feet from face of support. 64
Figure 6.23: Shear-moment interaction diagram for Specimen C11T22-B4-ML for cut section located 8 feet from face of support. 65
Figure 6.24: Shear-moment interaction diagram for Specimen C11T22-B4-ML for cut section located 9 feet from face of support. 65
Figure 6.25: Support and loading conditions, instrumentation and crack map for Specimen C11T16.5-B2-ML. Bold blue line denotes failure crack. 67
Figure 6.26: Shear-moment interaction diagram for Specimen C11T16.5-B2-ML at cut section located at face of support. 68
Figure 6.27: Shear-moment interaction diagram for Specimen C11T16.5-B2-ML at cut section located 1 foot from face of support. 68
Figure 6.28: Shear-moment interaction diagram for Specimen C11T16.5-B2-ML at cut section located 2 feet from face of support. 69
Figure 6.29: Shear-moment interaction diagram for Specimen C11T16.5-B2-ML at cut section located 3 feet from face of support. 69
Figure 6.30: Shear-moment interaction diagram for Specimen C11T16.5-B2-ML at cut section located 4 feet from face of support. 70
Figure 6.31: Shear-moment interaction diagram for Specimen C11T16.5-B2-ML at cut section located 5 feet from face of support. 70
Figure 6.32: Shear-moment interaction diagram for Specimen C11T16.5-B2-ML at cut section located 6 feet from face of support. 71
Figure 6.33: Shear-moment interaction diagram for Specimen C11T16.5-B2-ML at cut section located 7 feet from face of support. 71
Figure 6.34: Shear-moment interaction diagram for Specimen C11T16.5-B2-ML at cut section located 8 feet from face of support. 72
Figure 6.35: Shear-moment interaction diagram for Specimen C11T16.5-B2-ML at cut section located 9 feet from face of support. 72
Figure 6.36: Shear-moment interaction diagram for Specimen C10T12-B2-ML at cut section located at face of support. 73
Figure 6.37: Shear-moment interaction diagram for Specimen C10T12-B2-ML at cut section located 1 foot from face of support. 74
Figure 6.38: Shear-moment interaction diagram for Specimen C10T12-B2-ML at cut section located 2 feet from face of support. 74
Figure 6.39: Shear-moment interaction diagram for Specimen C10T12-B2-ML at cut section located 3 feet from face of support. 75
Figure 6.40: Shear-moment interaction diagram for Specimen C10T12-B2-ML at cut section located 4 feet from face of support. 75
Figure 6.41: Shear-moment interaction diagram for Specimen C10T12-B2-ML at cut section located 5 feet from face of support. 76
Figure 6.42: Shear-moment interaction diagram for Specimen C10T12-B2-ML at cut section located 6 feet from face of support. 76
Figure 6.43: Shear-moment interaction diagram for Specimen C10T12-B2-ML at cut section located 7 feet from face of support. 77
Figure 6.44: Shear-moment interaction diagram for Specimen C10T12-B2-ML at cut section located 8 feet from face of support. 77
Figure 6.45: Shear-moment interaction diagram for Specimen C10T12-B2-ML at cut section located 9 feet from face of support. 78

Figure 6.46: Strut and Tie used to estimate shear-dominated capacity near simple support of Specimen C10T16-B2-ML. Model A used a straight, prismatic strut. Model B used a series of struts restrained by stirrups.....79
Figure 6.47: Shear-moment interaction diagram for the right-hand side of Specimen C11IT16-B1-ML at cut section located at the face of support 80
Figure 6.48: Shear-moment interaction diagram for the right-hand side of Specimen C11IT16-B1-ML at cut section located 1 foot from the face of support.....80
Figure 6.49: Shear-moment interaction diagram for the right-hand side of Specimen C11IT16-B1-ML at cut section located 2 feet from the face of support 81
Figure 6.50: Shear-moment interaction diagram for the right-hand side of Specimen C11IT16-B1-ML at cut section located 3 feet from the face of support 81
Figure 6.51: Shear-moment interaction diagram for the right-hand side of Specimen C11IT16-B1-ML at cut section located 4 feet from the face of support 82
Figure 6.52: Shear-moment interaction diagram for the right-hand side of Specimen C11IT16-B1-ML at cut section located 5 feet from the face of support 82
Figure 6.53: Shear-moment interaction diagram for the right-hand side of Specimen C11IT16-B1-ML at cut section located 6 feet from the face of support 83
Figure 6.54: Shear-moment interaction diagram for the right-hand side of Specimen C11IT16-B1-ML at cut section located 7 feet from the face of support 83
Figure 6.55: Shear-moment interaction diagram for the right-hand side of Specimen C11IT16-B1-ML at cut section located 8 feet from the face of support 84
Figure 6.56: Shear-moment interaction diagram for the right-hand side of Specimen C11IT16-B1-ML at cut section located 9 feet from the face of support 84
Figure 6.57: Shear-moment interaction diagram for the right-hand side of Specimen C11IT16-B1-ML at cut section located 10 feet from the face of support 85
Figure 6.58: Shear-moment interaction diagram for left-hand side of Specimen C11IT16-B1-ML at cut section located at face of support. 85
Figure 6.59: Shear-moment interaction diagram for left-hand side of Specimen C11IT16-B1-ML 1 foot from cut section located at face of support.....86
Figure 6.60: Shear-moment interaction diagram for left-hand side of Specimen C11IT16-B1-ML 2 feet from cut section located at face of support.....86
Figure 6.61: Shear-moment interaction diagram for left-hand side of Specimen C11IT16-B1-ML 3 feet from cut section located at face of support.....87
Figure 6.62: Shear-moment interaction diagram for left-hand side of Specimen C11IT16-B1-ML 4 feet from cut section located at face of support.....87
Figure 6.63: Shear-moment interaction diagram for left-hand side of Specimen C11IT16-B1-ML 5 feet from cut section located at face of support.....88
Figure 6.64: Shear-moment interaction diagram for left-hand side of Specimen C11IT16-B1-ML 6 feet from cut section located at face of support.....88
Figure 6.65: Shear-moment interaction diagram for left-hand side of Specimen C11IT16-B1-ML 7 feet from cut section located at face of support.....89
Figure 6.66: Shear-moment interaction diagram for left-hand side of Specimen C11IT16-B1-ML 8 feet from cut section located at face of support.....89
Figure 6.67: Shear-moment interaction diagram for left-hand side of Specimen C11IT16-B1-ML 9 feet from cut section located at face of support.....90
Figure 6.68: Shear crack motion under moving load. (a) Initial crack position. (b) Crack compression as the moving load approaches the test position. Crack features are forced into bearing. (c) Transverse and longitudinal crack motion as the load moves away from the test position. Note the spalling along points of bearing. (d) Final crack position at the end of live load travel. Green arrows denote relative crack motion parallel and transverse to the crack. 93
Figure 6.69: Moving load stirrup behavior in (a) a moving load specimen subjected to loads of increasing magnitude, and (b) an existing bridge subjected to ambient truck traffic. Stirrup compression accounted for 8% to 15% of the total elastic stirrup strain measured in the field (red arrow) and 40% to 90% of the total elastic stirrup strain measured in the laboratory (blue arrow). 95

1.0 INTRODUCTION

Laboratory tests have been performed to assess the combined shear and moment capacity of conventionally reinforced concrete (CRC) girders with stationary loads and fixed shear-to-moment ratios. Different shear-to-moment ratios have previously been achieved by changing the span lengths and support locations relative to the loading point(s) for different specimens. These laboratory conditions differ from actual bridge girders that are subject to both stationary loads (dead load) and moving loads. Moving loads produce varying shear-moment interactions that depend on the structural indeterminacy of the bridge, the location of the girder within the bridge, and the truck load (position and axle configurations). Previous work on moving loads has been done in Japan, for small-sized specimens with flexural dominated behavior (*Kawguchi 1992; Tadashi1999; Tadashi 2000*) Currently, there is no published research that addresses failure of girders subjected to large-sized varying shear-to-moment ratios under moving load.

Laboratory experiments with invariant shear-to-moment ratios tend to generate crack patterns that concentrate or fan about the loading points. These crack patterns generally differ from those observed in existing CRC bridges (Figure 1.1). In the field, diagonal tension cracks tend to be more widely spaced and more vertically oriented, with crack angles determined by principal stresses resulting from the combination of moving truck loads, dead loads, shrinkage strains and thermally induced deformations. Cracking of the concrete alters the mechanisms by which stresses are carried through the beam resulting in a redistribution of internal stresses. Prior to diagonal cracking, the concrete carries the majority of the load with the reinforcing steel participating to a very small degree. After diagonal cracking, the reinforcing steel begins to carry a larger share of the load. This stress redistribution is influenced by the pattern of concrete cracks, resulting in different stress fields for the laboratory specimens described above, compared to the CRC bridge beams observed in the field. It is unclear whether moving loads influence the overall girder performance given the differences in crack patterns.

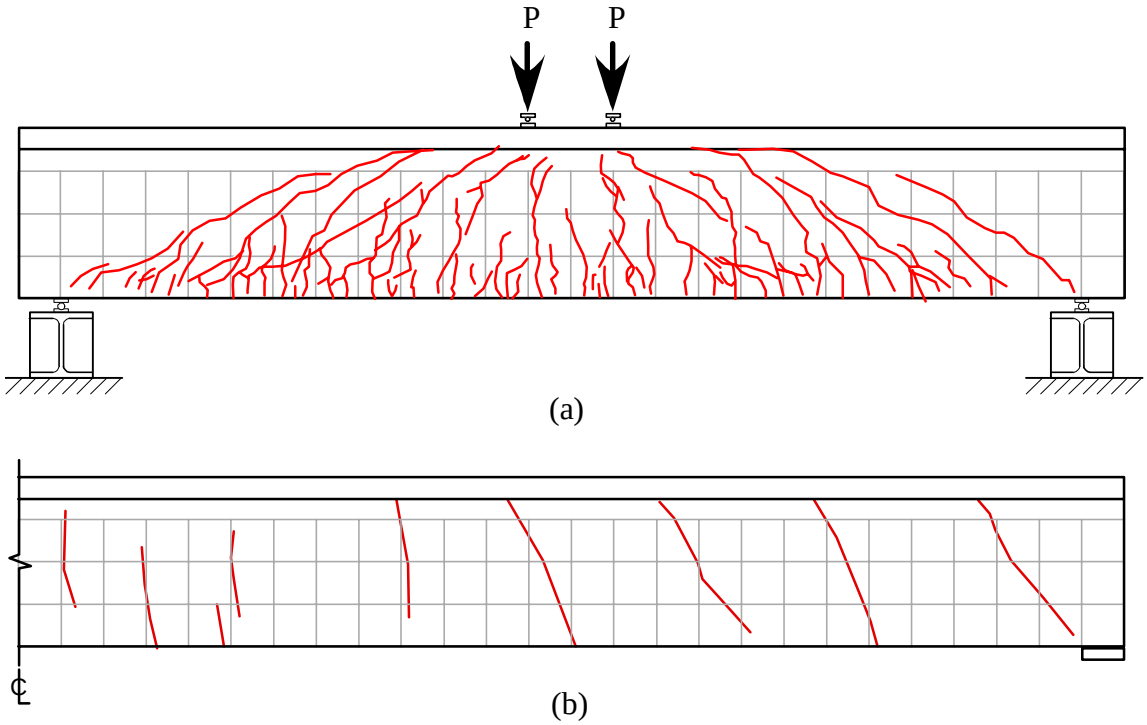

Figure 1.1: Typical crack patterns measured in (a) a laboratory specimen with stationary load and fixed shear-to-moment ratio and (b) an existing girder from ODOT Bridge No. 08175N, Spores Bridge, subjected to moving loads and constantly varying shear-to-moment ratios. The cracks in the existing bridge girder tend to be more vertically oriented and more widely spaced along the girder length.

There is a need to evaluate the performance of large, full-scale girders subject to varying shear-to-moment ratios under moving loads, and to compare this performance with models developed using stationary loads and fixed shear-to-moment ratios. A series of full-scale experiments were performed to address this need. Test specimens consisted of a simulated girder subassembly based on an in-service, CRC deck-girder bridge of 1950's vintage construction exhibiting diagonal-tension cracking. A unique loading system was developed to apply combined stationary and moving loads to the specimens, allowing simulation of shear-moment interactions consistent with those possible in the field. Differences in the behavior of CRC beams subjected to variable shear-moment interactions were identified and overall specimen capacities were compared to existing models developed from stationary load, fixed shear-to-moment ratio beam tests.

2.0 BACKGROUND

2.1 SHEAR CAPACITY OF CRC BRIDGE GIRDERS

Three codified methodologies are currently used for the shear design of CRC bridge girders. The simplest and most easily applied is that specified in the AASHTO 17^{h} Edition of the *Standard Specification for Highway Bridges* (*2002*) based on Chapter 11 of the American Concrete Institute publication *Building Code Requirements for Structural Concrete (ACI 318-02*(*2002*). This method attributes the overall shear capacity to a summation of capacities provided independently by the concrete and the shear reinforcement. In this method shear capacity is evaluated independently of moment capacity.

The second method is specified in *AASHTO LRFD Bridge Design Specifications* (*1998*), which is based on modified compression field theory (MCFT). This method takes into account the interaction between shear and moment capacities. Although the AASHTO LRFD has been calibrated to provide conservative results, it is generally regarded as the more accurate of the first two methods.

The third method, called the strut-and-tie method, is also specified in *AASHTO LRFD Bridge Design Specifications* (*1998*). The strut-and-tie method works by transforming the reinforced concrete matrix into a truss consisting of a series of concrete compression struts and tension steel ties connected by nodes. The strut-and-tie method is more appropriate to deep beams and regions with span-to-depth ratios less than 2.

In addition to the specification based approaches, the combined shear and moment capacities of a girder can be evaluated using a specialty computer program called *Response 2000*^{TM} (*Bentz 2000*). The program uses a sectional analysis approach to assess the load-deformation response of cross-sections subject to bending moments, shear forces, and axial loads. Constitutive relationships between stresses and strains at a section are based on Modified Compression Field Theory (MCFT) and have been shown to provide good prediction of specimen shear-moment capacities.

2.2 STRUCTURAL MODEL

A structural model was selected from among the CRC deck-girder bridges designed during the Eisenhower era highway construction boom, of which large numbers remain in-service. A database was developed to quantify typical parameters such as, span length, indeterminacy, number of girders, girder dimensions, slab thickness, material properties, and reinforcing steel details for CRC deck-girder bridges exhibiting diagonal tension cracks. Of the existing CRC deck-girder bridges located in Oregon, an in-service structure was identified that corresponded closely to the most commonly identified bridge characteristics. The structure is the west

approach spans of ODOT Bridge No. 08051, commonly called the Springfield Bridge (Figure 2.1), which crosses the Willamette River between Springfield and Eugene, Oregon, on State Route 126.

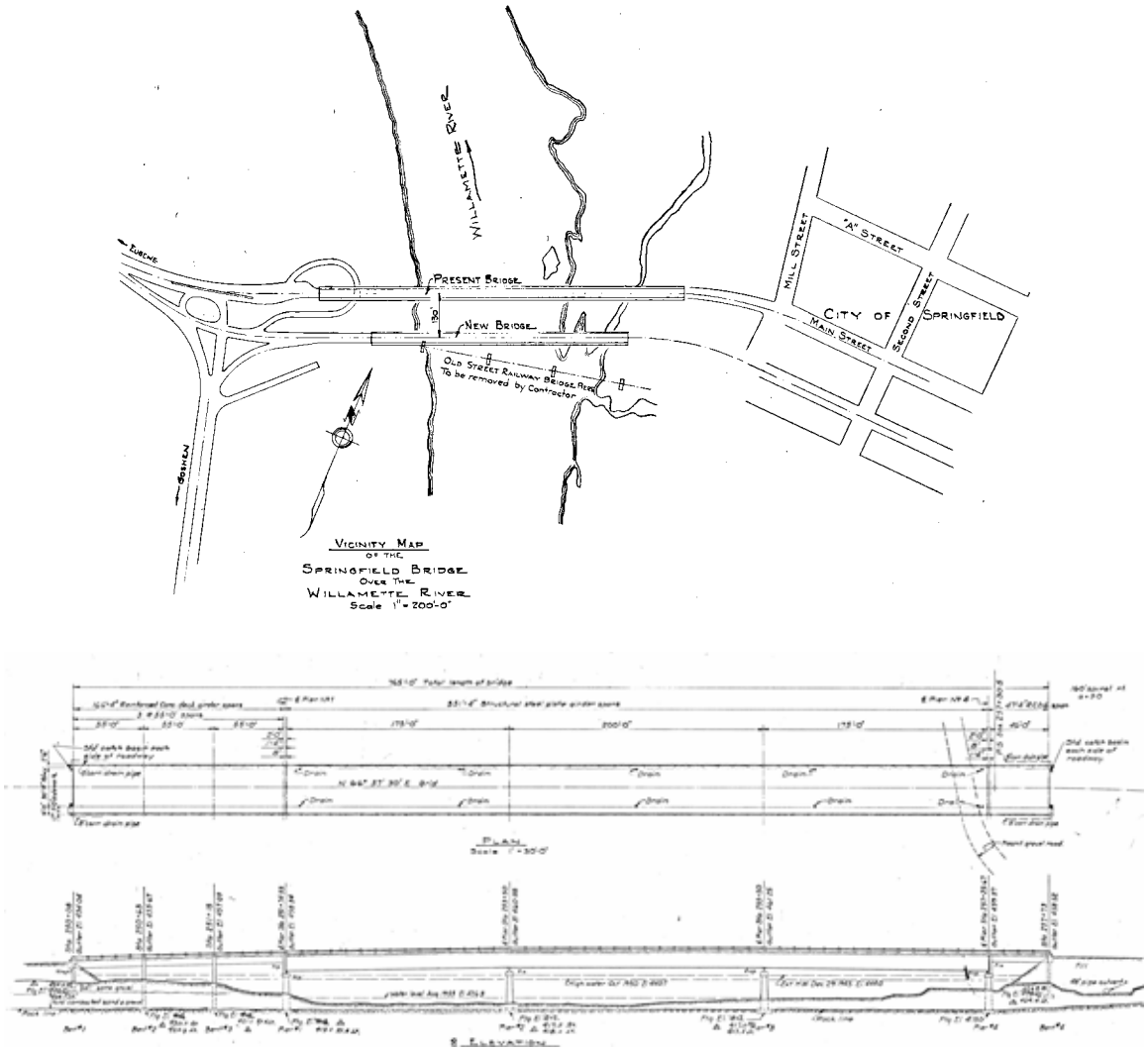

Figure 2.1: Springfield Bridge, ODOT Bridge No. 08051, (a) vicinity map and (b) plan and elevation views. Laboratory specimens were modeled after the three-span-continuous west approach spans.

The west approach spans are shown in Figure 2.2. The span lengths are each 16.8 m (55 ft) with supports at Bents 1, 2, and 3 and Pier 1, forming a 3-span continuous bridge. The spans have a roadway width of 9.1 m (30 ft), and a total width of 11.7 m (38.5 ft). A 1.5 m (5 ft) wide sidewalk is located on the south side of the bridge. Five (5) 330 mm x 1220 mm (13 in x 48 in) girders support the 150 mm (6 in) thick reinforced concrete deck, with 200 mm x 1170 mm (8 in

x 46 in) diaphragms located at the quarter points of each span. The sidewalk is principally supported by one of the exterior girders. Bent caps are 420 mm x 2210 mm (16.5 in x 87 in).

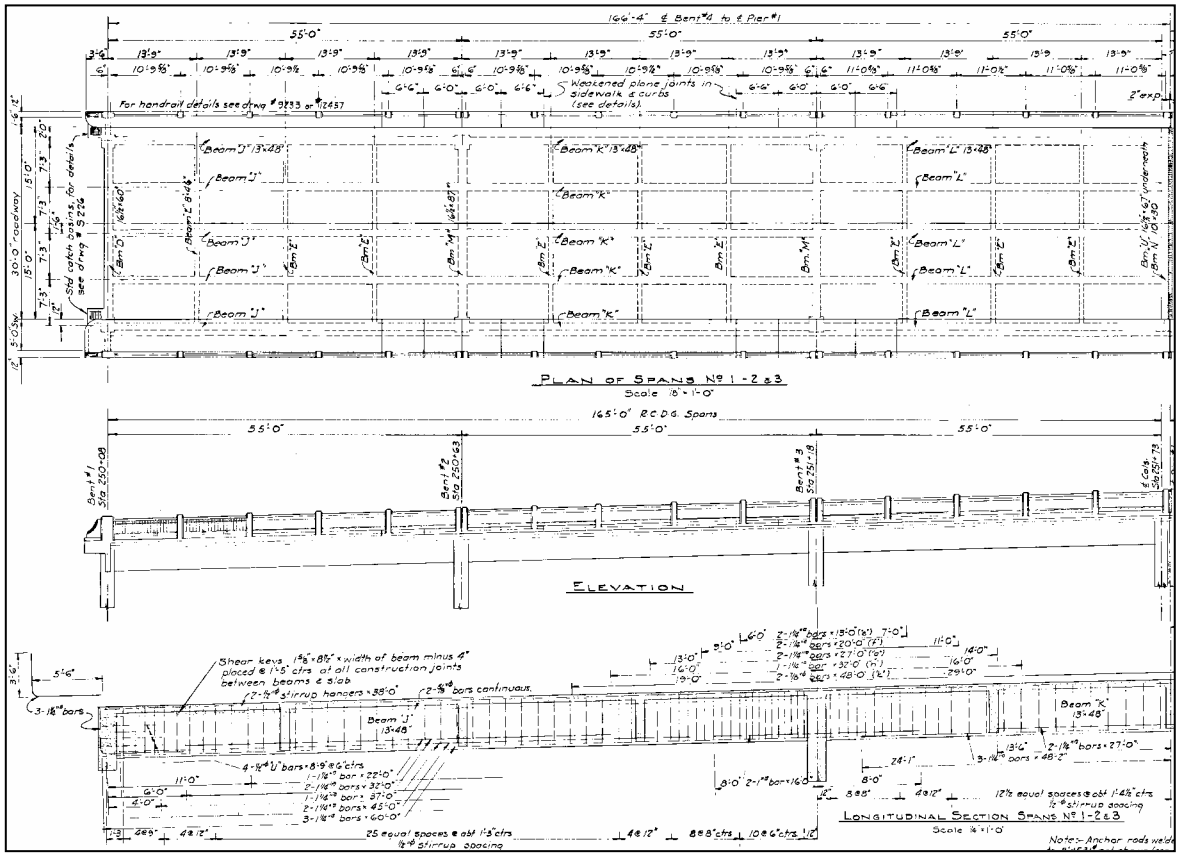

Figure 2.2: Plan view, elevation view and reinforcing details for the west approach spans of Springfield Bridge, ODOT Bridge No. 08051.

The specified concrete strength was 3300 psi (22.8 KPa) and the reinforcing steel consists of intermediate grade deformed bars corresponding to A305-50T (*ASTM 1950a*). Intermediate grade steel had a minimum yield stress of 275 MPa (40 ksi) and tensile strength ranging between 480-620 MPa (70-90 ksi) (*ASTM 1950b* and *1950c*). The flexural steel in the girders consists mainly of 32 mm (1.25 in) square bars and the stirrups are 13 mm (0.5 in.) diameter round bars. As was customary for the time, the flexural steel was terminated along the span where the designer determined it to no longer be necessary. Anchorage of the flexural steel is achieved through straight-bar development in the bent caps and girders. The stirrups have 90° hooks anchored around flexural reinforcing bars located in the deck. A shear key is located at the cold-joint between the girder stems and the deck.

2.3 MOVING LOAD HISTORY

Moving vehicle loads on a bridge produce variable moments and shears at points along the girders. The magnitude of these load effects depends on static equilibrium, axle loads, axle locations on the span, structural indeterminacy and the load distribution of the system. Based on field measurements of typical CRC deck-girder bridges located in Oregon, stirrup stresses at diagonal crack locations were found to correspond well with those calculated using elastic structural analysis (*as presented in previous sections of this report*). The magnitude of stress varies depending on the location of interest relative to the supports, the angle of the crack, and tire load positions. By positioning trucks of known weight, so as to produce the largest magnitude shears at a point of interest (as measured in the field) and attributing all vertical shear to the girders by neglecting the deck contribution, the worst possible shear load distribution for a single girder was found to be approximately 80% of a single truck load effect. This corresponds to a truck positioned along the curb, with the load effects being highest in the exterior girder. More typical values are 60% for the supported lane and 15% of the adjacent lane. This worst case, field-measured, distribution value (80%) was less than the value from the AASHTO LRFD and Standard Specification (approximately 90%) and was used in this study.

Live load shear-moment interactions were computed for the Springfield Bridge at girder locations near simple and continuous supports. The AASHTO HL-93 truck configuration (with all permissible axle spacings), the design tandem, and actual truck data taken from previous field work were used in calculating the shear-moment interactions. Using idealized support conditions and elastic structural analysis, the shear and corresponding moments were determined at locations along the span. At the girder ends, near simple supports, the shear and moment interactions are linearly related as seen in Figure 2.3. However, at continuous supports, the shear-moment interactions are more complex as shown in Figure 2.4. The unfactored shear-moment interactions were calculated for the continuous supports of the Springfield Bridge by multiplying the non-linear shear and moment interactions described above by the distribution factor (80%) and the AASHTO LRFD impact coefficient (1.33), and superimposing the permanent loads and wearing surface shear and moment. The resulting shear-moment interactions are shown in Figure 2.5.

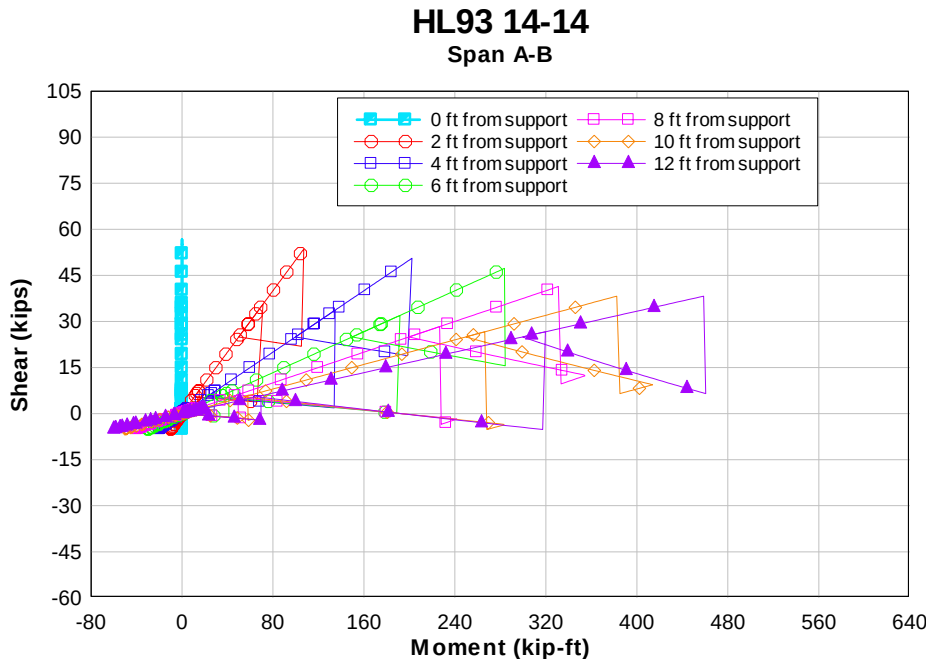

Figure 2.3: Shear-moment interactions for HL-93 truck model with 14 ft (4.27 m) axle spacing at locations near simply supported girder ends, Springfield Bridge.

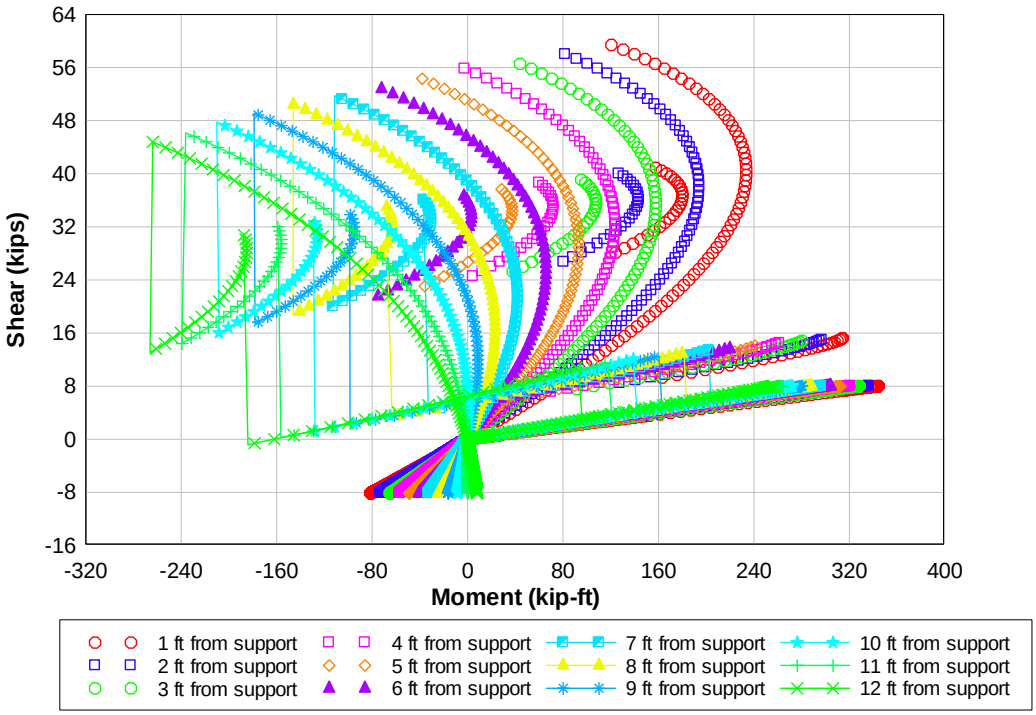

Figure 2.4: Shear-moment interactions for HL-93 truck model with 14 ft (4.27 m) axle spacing at locations near interior continuous supports, Springfield Bridge.

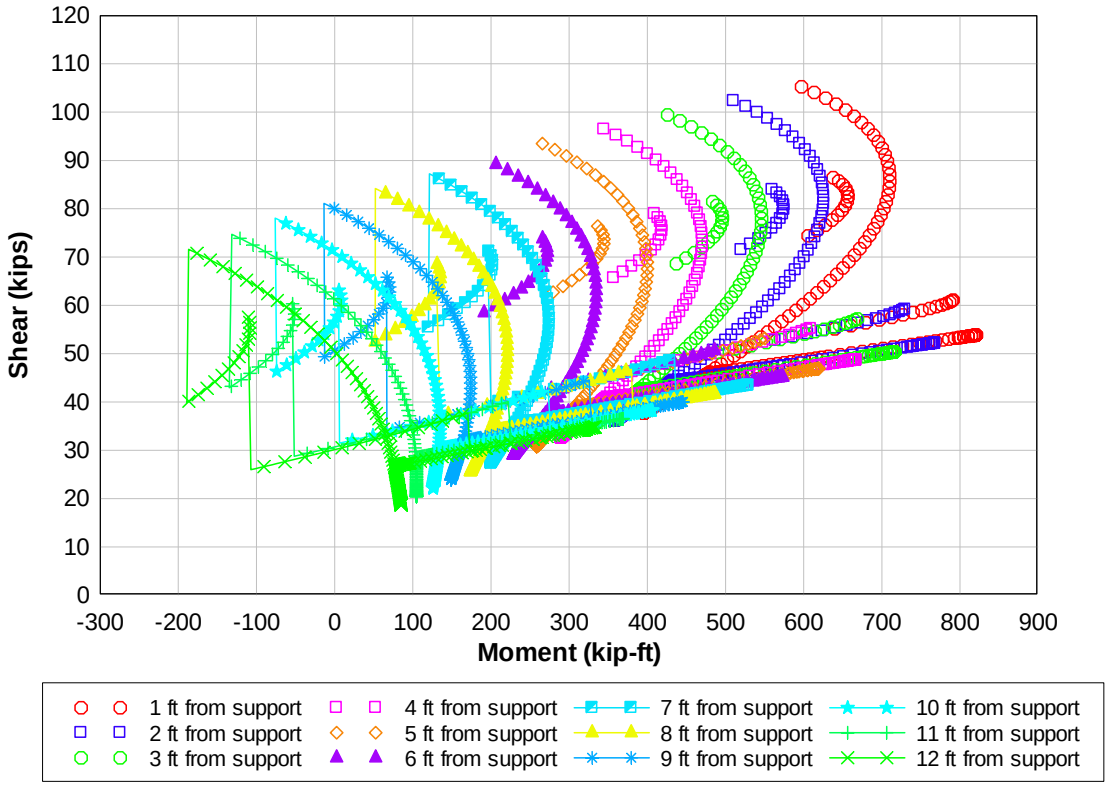

Figure 2.5: Shear-moment interactions for HL-93 truck model with 14 ft (4.27 m) axle spacing at locations near interior continuous supports including permanent load and wearing surface (dead load) effects.

As a result of this non-linear relationship near the continuous supports, the peak induced moment does not correspond with the peak induced shear. Determining the critical combination depends on the shear-moment interaction capacity at the point of interest. The shear-moment interaction capacity can be estimated using MCFT or Response 2000™. Alternatively, the shear capacity can be independently estimated using the ACI 318-02 method.

3.0 SPECIMEN DESIGN

Five (5) specimens were constructed and tested. Specimens were identified with a number and letter designator identifying the cast number, cross-sectional geometry, largest stirrup spacing, form number and loading protocol. Specimens were designed and constructed to approximate the girder geometry, cross-section properties, material properties, stirrup spacing, reinforcing detailing and girder shear capacities of the Springfield Bridge west approach spans. All specimens were 1220 mm (48 in) deep T-beams (or Inverted-T) with a 355 mm (14 in) wide stem and 150 mm (6 in) thick deck. The specified concrete compressive strength was 22.8 kPa (3300 psi) at 28 days. Stirrups were of A615 Grade 40 reinforcing steel with a yield stress of 359 MPa (52 ksi). Flexural reinforcing was of modern A706 Grade 60 steel with a yield stress of 478 MPa (69.4 ksi). Flexural reinforcing was sized to approximate the moment capacity curves of the Springfield Bridge. Given the higher grade of modern steel, this required that the specimens have less area of flexural reinforcing than the existing bridge. As a result, the dowel contribution to shear capacity for the specimens is less than that of the Springfield Bridge.

A more detailed description of each specimen design is provided below. A summary of cross-sectional properties is provided in Table 3.1. Detailed views of each specimen are provided in Figures 3.1 thru 3.4.

Table 3.1: Beam cross-sectional and material properties

Specimen	h	b	b_w	d	f_c' (psi)		f_y	f_{yv}	s	A_v
	(in)	(in)	(in)	(in)	Stem	Deck	(ksi)	(ksi)	(in)	(in^2)
C11T16.5-B2-ML	48	36	14	45.3	4970	4170	69.3	52.0	8, 12, 16.5	0.4
C11T22-B3-ML					4470	3510			10.5, 16, 18	
C11T22-B4-ML					4750	4010			10.5, 16, 18	
C10T12-B2-ML					4655	4405			12, 16, 20	
C11IT16-B1-ML					4635	4430			10.5, 16	

3.1 C11T16.5-B2-ML

The test span of this specimen was constructed to reflect the girder stirrup spacing found in the negative moment region of the Springfield Bridge near continuous supports. One (1) stirrup was placed 100 mm (4 in) from the face of support followed by seven (7) stirrups at 200 mm (8 in) on-center (OC), four (4) stirrups at 305 mm (12 in) OC, and two (2) stirrups at 420 mm (16.5 in) OC, equivalent to the negative moment stirrup spacing in the Springfield Bridge. Regions of the specimen not included in the test span were overly reinforced to ensure failure of the test span. Dimensions and reinforcing details for this specimen are shown in Figure 3.1

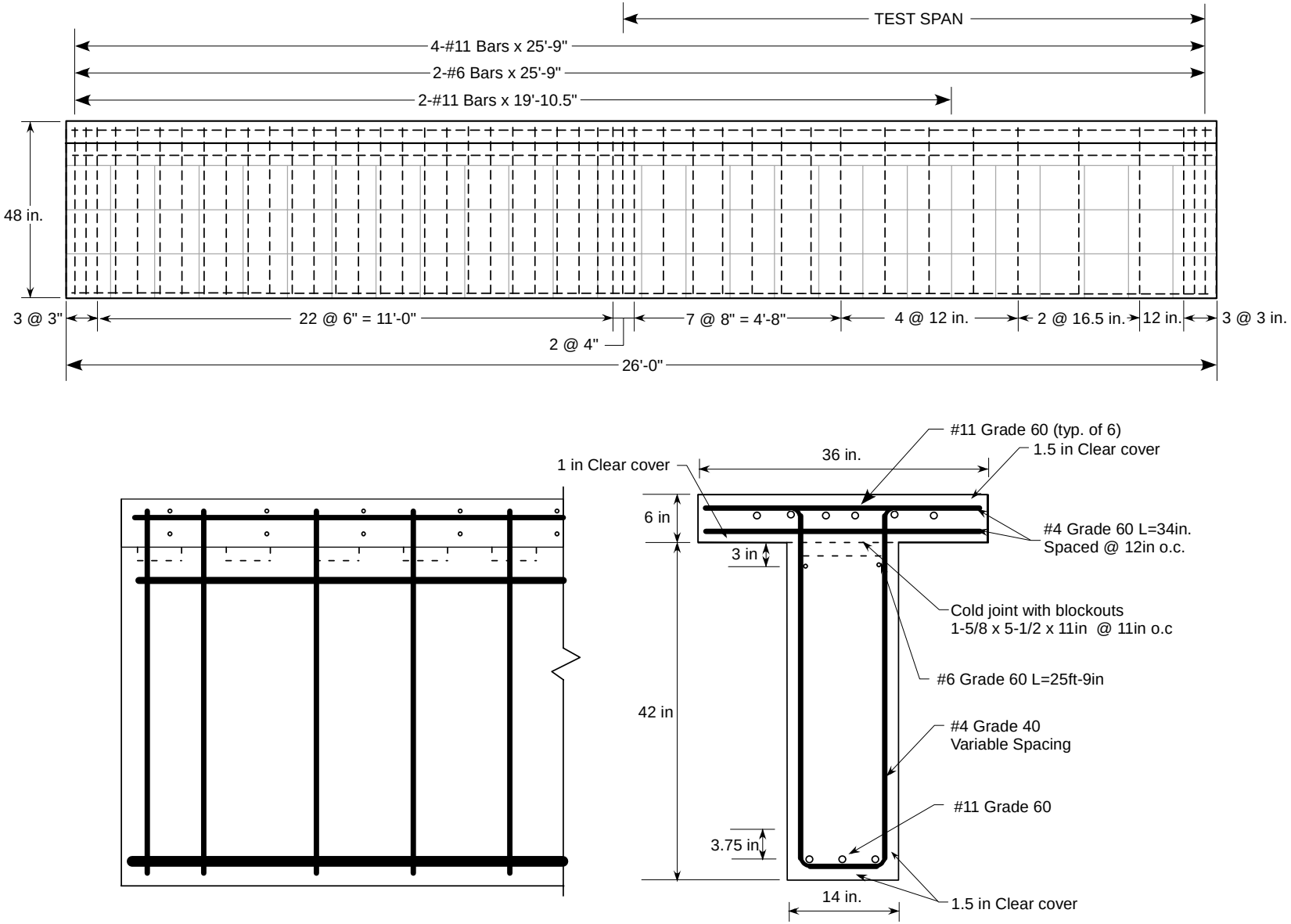

Figure 3.1: Dimensions and reinforcing details for Specimen C11T16.5-B2-ML

3.2 C11T22-B3-ML

The test span of this specimen was constructed to reflect the girder shear capacity in the negative moment region of the Springfield Bridge near continuous supports. Given the difference between the specified bridge stirrup yield stress of 40 ksi (276 MPa) and the specimen stirrup yield stress of 52 ksi (359 MPa), the stirrup capacity of the Springfield Bridge was maintained by increasing the specimen stirrup spacing by a factor of 52/40 = 1.3. Therefore, one (1) stirrup was placed at 100 mm (4 in) from the face of support followed by five (5) stirrups at 270 mm (10.5 in) OC, four (4) stirrups at 405 mm (16 in) OC, and one (1) stirrup at 460 mm (18 in) OC. Regions of the specimen not included in the test span were overly reinforced to ensure failure of the test span.

3.3 C11T22-B4-ML

This specimen design is identical to specimen C11T22-B3-ML, permitting the application of different loading histories. Dimensions and reinforcing details for specimens C11T22-B3-ML and C11T22-B4-ML are shown in Figure 3.2.

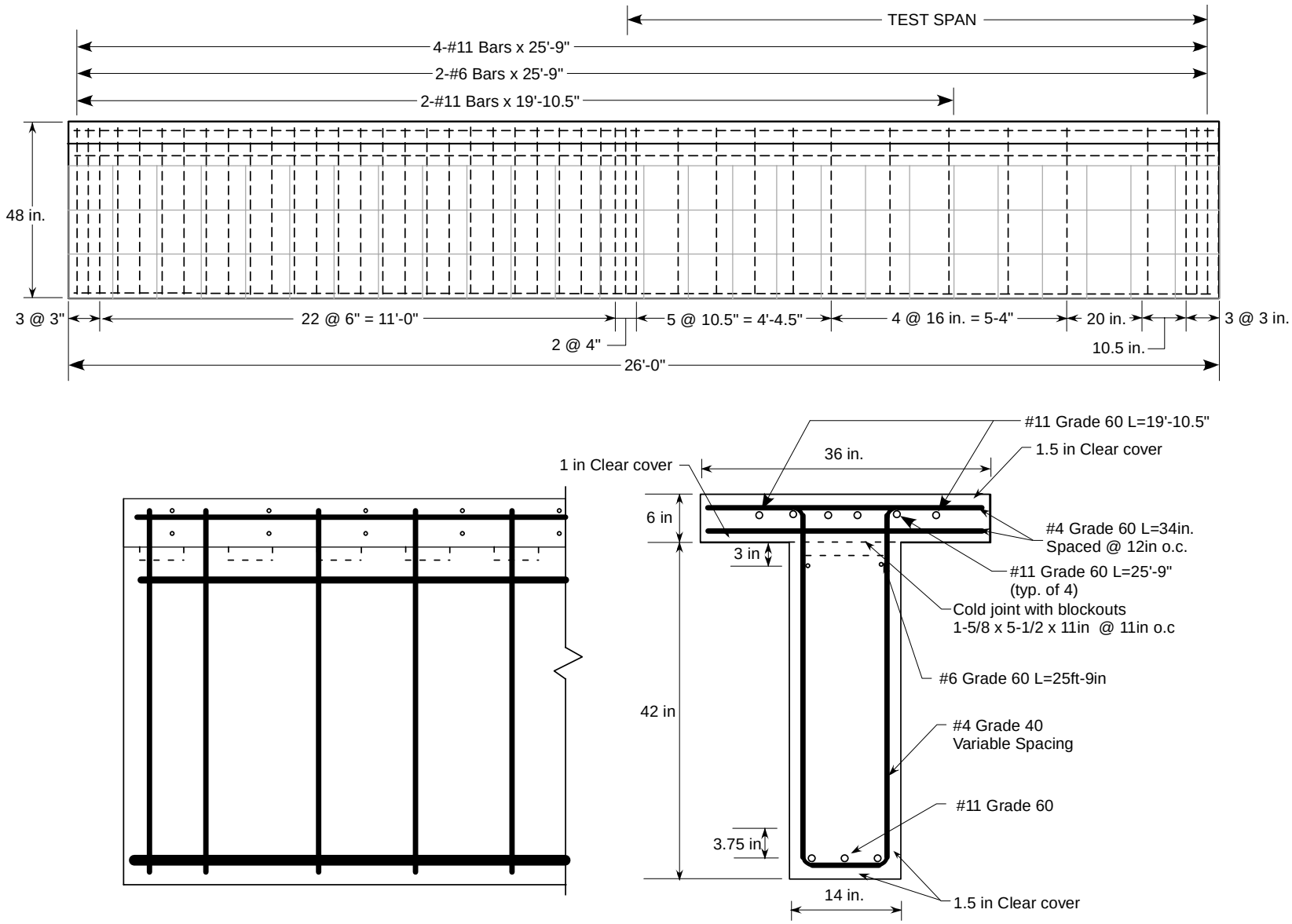

Figure 3.2: Dimensions and reinforcing details for Specimens C11T22-B3-ML and C11T22-B4-ML

3.4 C10T12-B2-ML

The test span of this specimen was constructed to reflect the girder shear capacity in the positive moment region of the Springfield Bridge near simple supports. As with specimens C11T22-B3-ML and C11T22 B4 ML, the stirrup capacity of the Springfield Bridge was maintained by increasing the specimen stirrup spacing by a factor of 1.3. Therefore, from the face of support three (3) stirrups were placed at 305 mm (12 in) OC followed by three (3) stirrups at 405 mm (16 in) OC and three (3) stirrups at 510 mm (20 in) OC. The simply supported beam ends of the Springfield Bridge also include three (3) 90º hooked anchorage bars extending 1.7 m (5.5 ft) into the span, typical of many vintage Oregon bridges. Besides providing additional partially-developed flexural reinforcing at the beam end, the anchorage bar detail reinforces the end of the girder to minimize bearing failure at the bottom corner. This detail was recreated in the specimen using #11 deformed bar. Dimensions and reinforcing details for this specimen are shown in Figure 3.3.

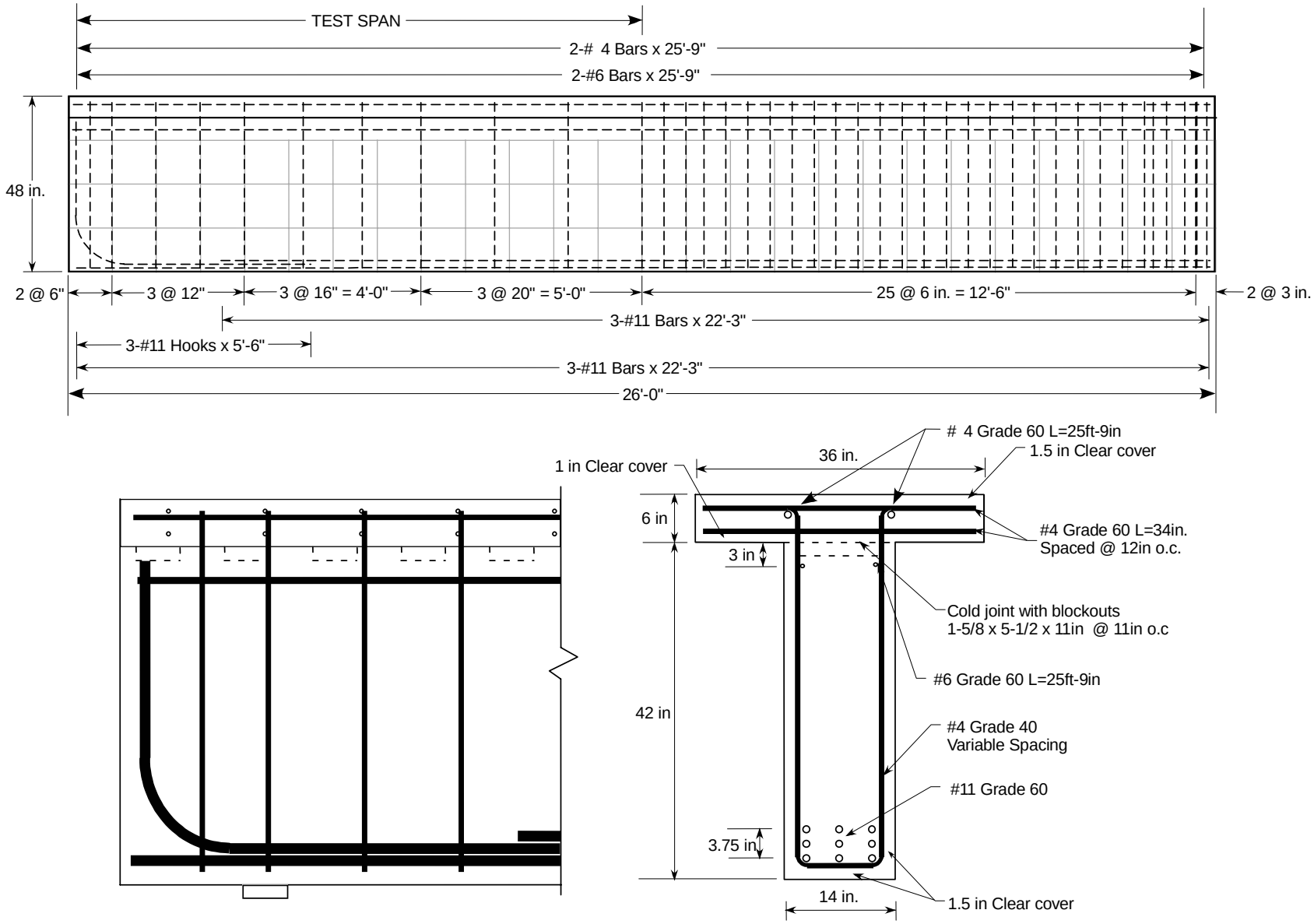

Figure 3.3: Dimensions and reinforcing details for Specimen C10T12-B2-ML

3.5 C11IT16-B1-ML

This specimen was constructed to reflect the girder shear capacity in the negative moment region of the Springfield Bridge near continuous supports. The stirrup configuration is identical to specimens C11T22-B3-ML and C11T22-B4-ML, except that this specimen was designed to be tested under monotonic loading to compare moving load and monotonic load capacities of similar specimens. This specimen has two test spans as shown in Figure 3.4.

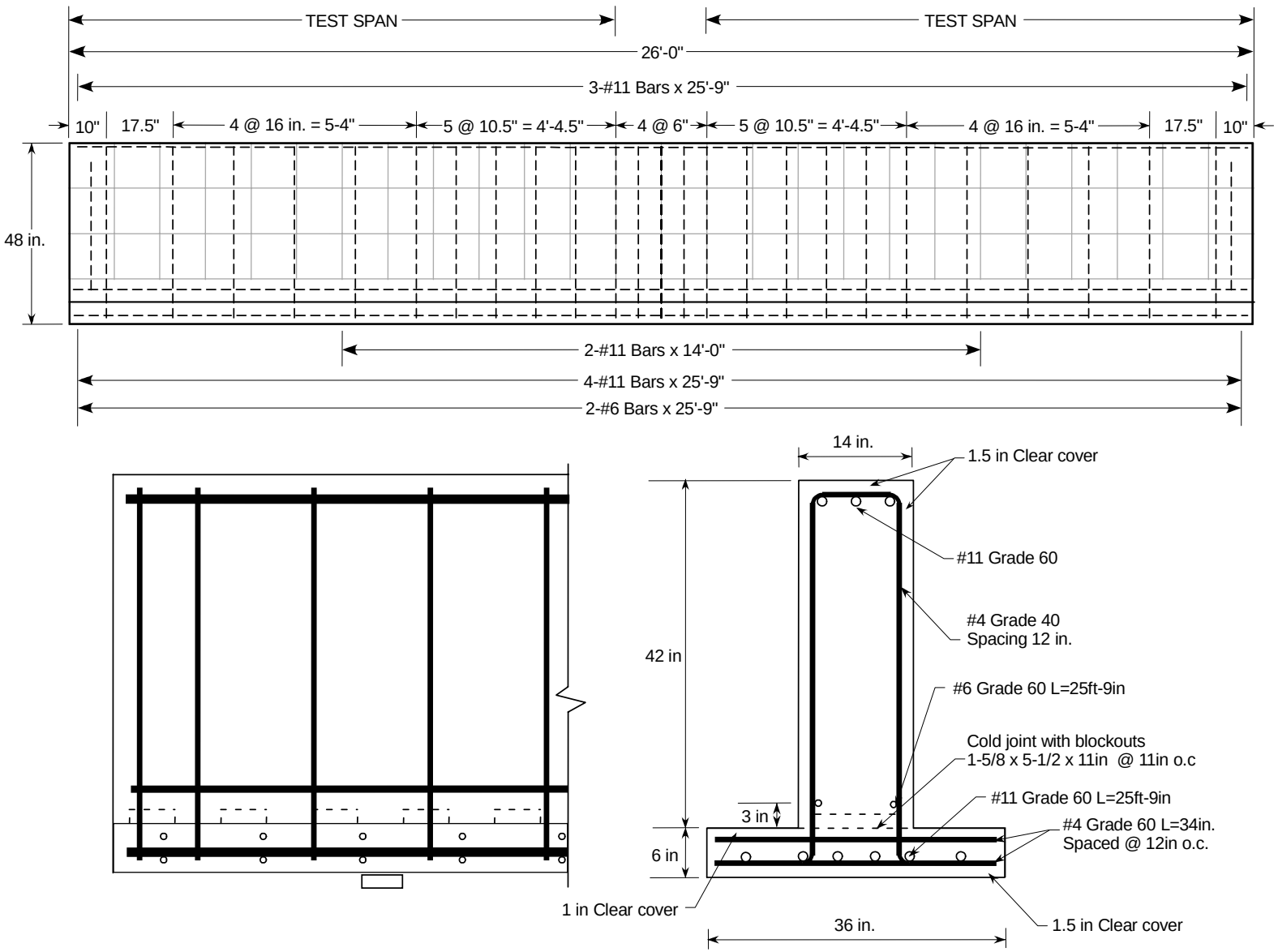

Figure 3.4: Dimensions and reinforcing details for Specimen C11IT16-B1-ML

Shear capacities of the existing bridge and the test specimens, based on ACI 318-02, are shown in Figures 3.5 and 3.6. The moment strength curves for the existing bridge and the test specimens are shown in Figures 3.7 and 3.8. The flexural steel dowel areas of the existing bridge and the test specimens are also shown in Figures 3.7 and 3.8.

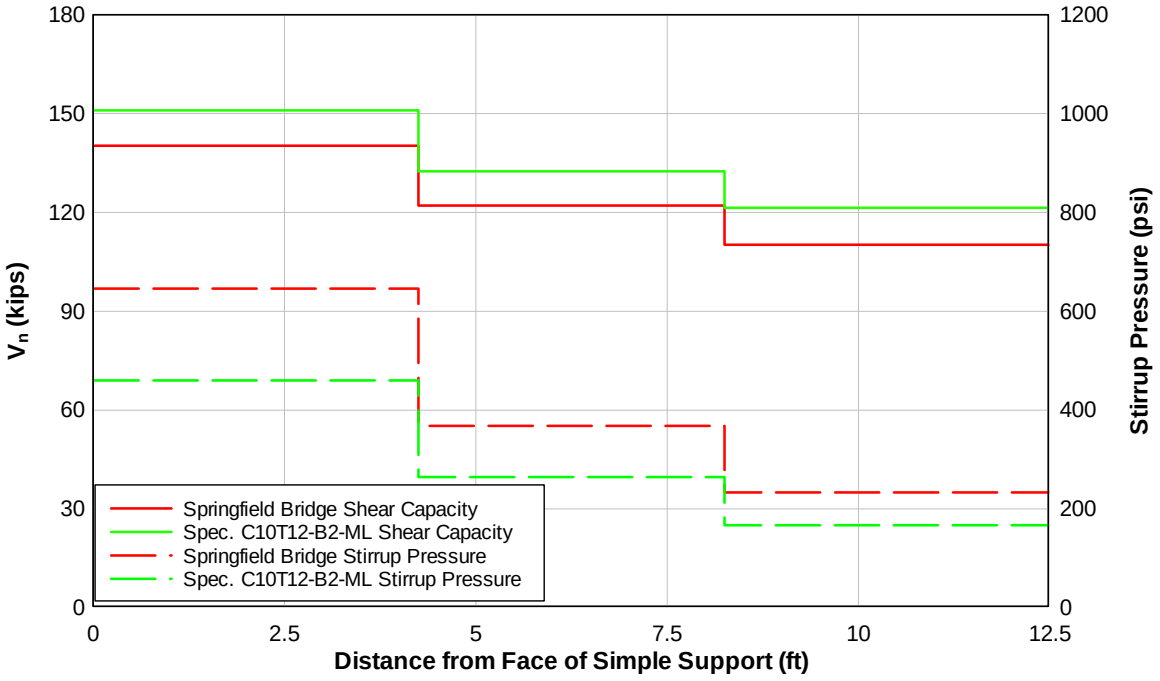

Figure 3.5: ACI 318-02 shear capacity and stirrup pressures at the simply supported ends of the Springfield Bridge (red) and Specimen C10T12-B2-ML (green). The shear capacity of the Springfield Bridge was based on the specified concrete compressive strength f'c =3300 psi. The stirrup spacing of the specimen was increased by a factor of 1.3 to approximate the shear capacity and stirrup pressures of the Springfield Bridge. In this figure, stirrup pressure is defined as (Av Fyv / s bw).

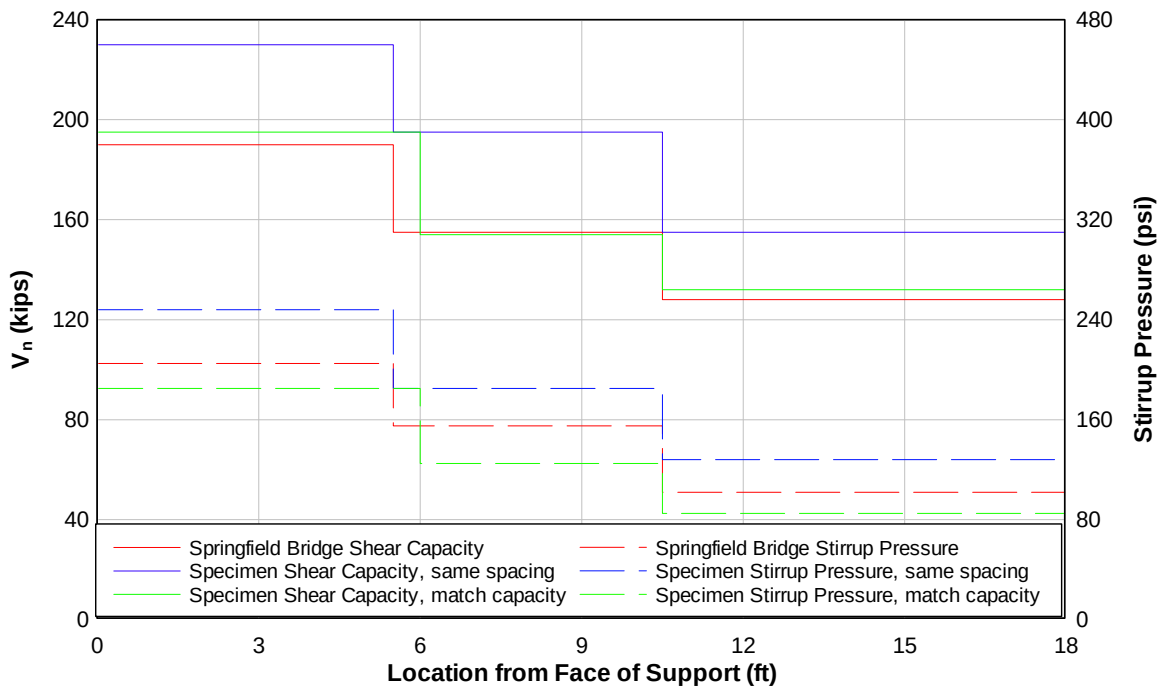

Figure 3.6: ACI 318-02 shear capacity and stirrup pressures over continuous supports of the Springfield Bridge (red), Specimen C11T16.5-B2-ML (blue), and Specimens C11T22-B3-ML, C11T22 B4 ML and C11IT16-B1-ML (green). The shear capacity of the Springfield Bridge was based on the specified concrete compressive strength f'c = 3300 psi. The stirrup spacing of Specimens C11T22-B3-ML, C11T22-B4-ML and C11IT16-B1-ML were increased by a factor of 1.3 to approximate the shear capacity and stirrup pressures of the Springfield Bridge. In this figure, stirrup pressure is defined as (Av Fyv / s bw).

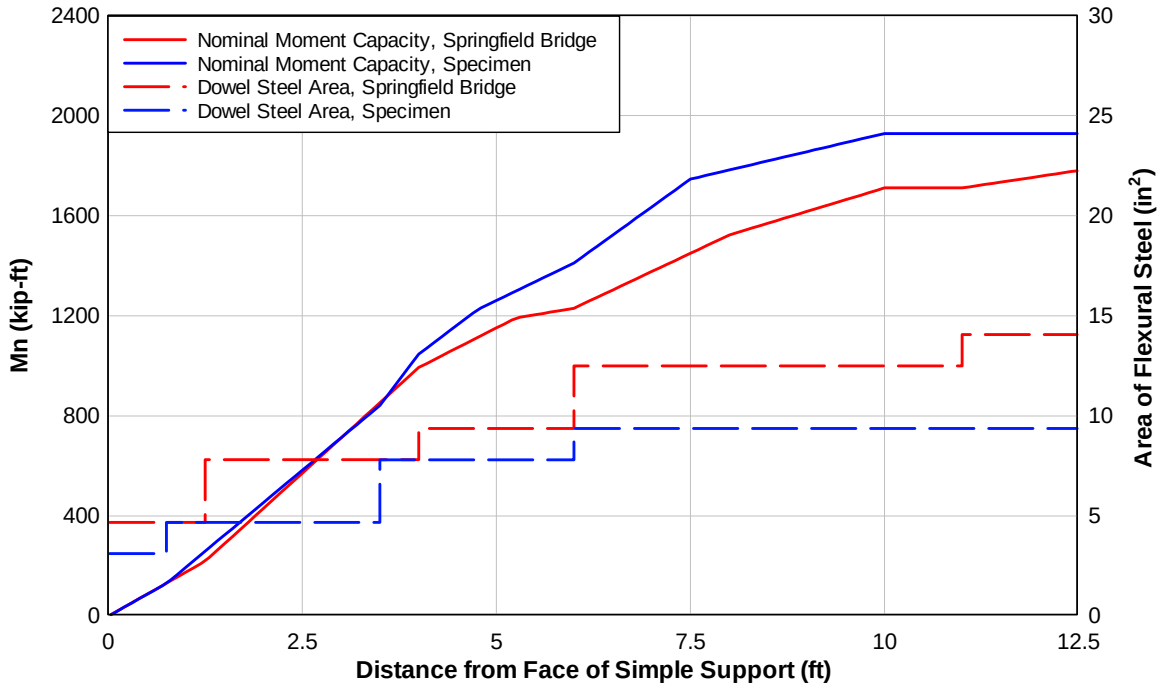

Figure 3.7: ACI 318-02 moment capacities and dowel steel cross-sectional area at simply supported ends of the Springfield Bridge and Specimen C10T12-B2-ML.

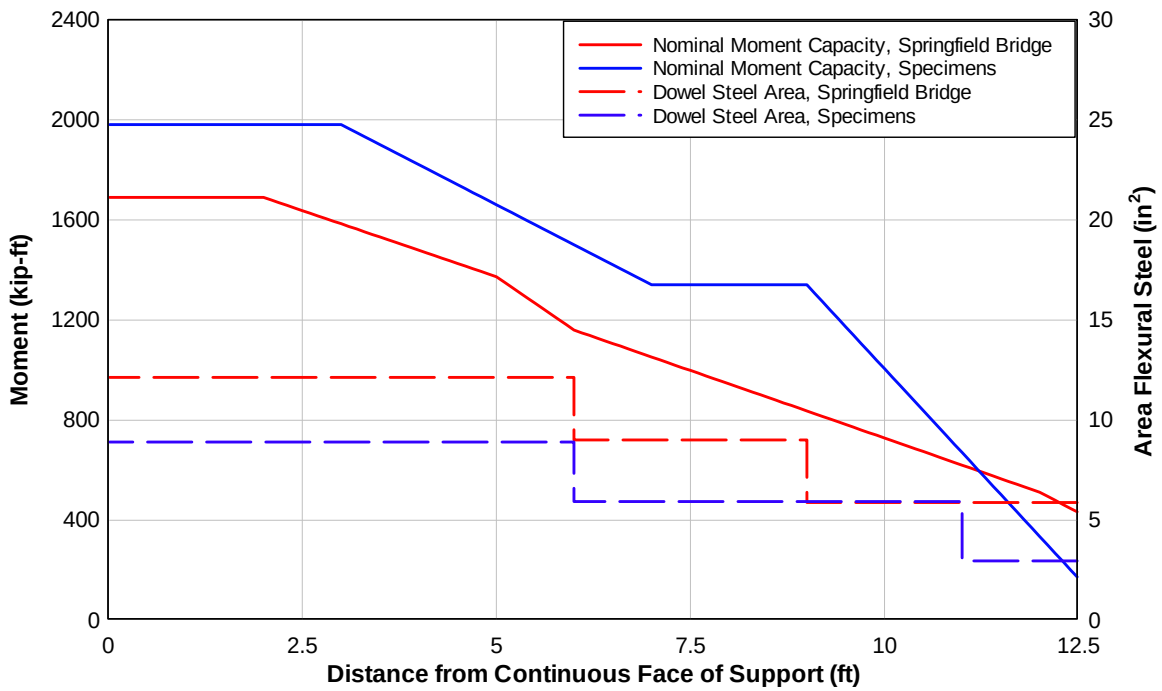

Figure 3.8: ACI 318-02 moment capacities and dowel steel cross-sectional area at continuous supports of the Springfield Bridge and Specimens C11T16.5-B2-ML, C11T22-B3-ML, C11T22-B4-ML and C11IT16-B1-ML.

4.0 TESTING APPARATUS DESIGN

The application of moving loads capable of inducing failure in full-scale girder specimens required design and construction of a new moving load apparatus that had not previously been attempted. A schematic of the moving load apparatus is shown in Figure 4.1. The moving load apparatus consisted of a horizontal rail, support frames, a moving load dolly, reaction supports, dead load cylinder, hydraulic power, servo-hydraulic controls and a data acquisition system. Two support configurations were used; Specimens C11T16.5-B2-ML, C11T22-B3-ML and C11T22-B4-ML were supported as cantilevers as shown in Figure 4.1(a) while Specimens C10T12-B2-ML and C11IT16-B1-ML were supported as shown in Figure 4.1(b). The cantilevered specimens model the shear-moment behavior of the continuous girders in the Springfield Bridge, from dead load inflection point to dead load inflection point (Figure 4.2). The simple supports of Specimen C10T12-B2-ML model the shear-moment behavior of the simply supported girder ends. The simple supports of Specimen C11IT16-B1-ML model the monotonic loading of the continuous girders loaded near the dead load points of inflection. Pictures of the completed system are provided in Figures 4.3 thru 4.5.

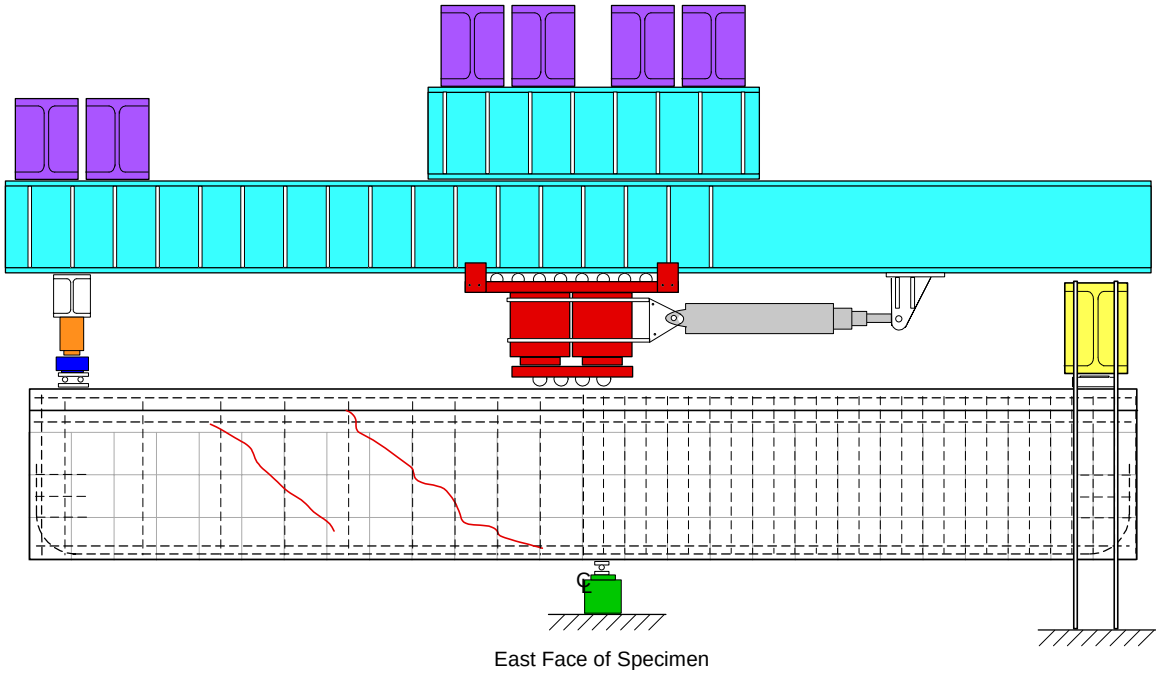

(a)

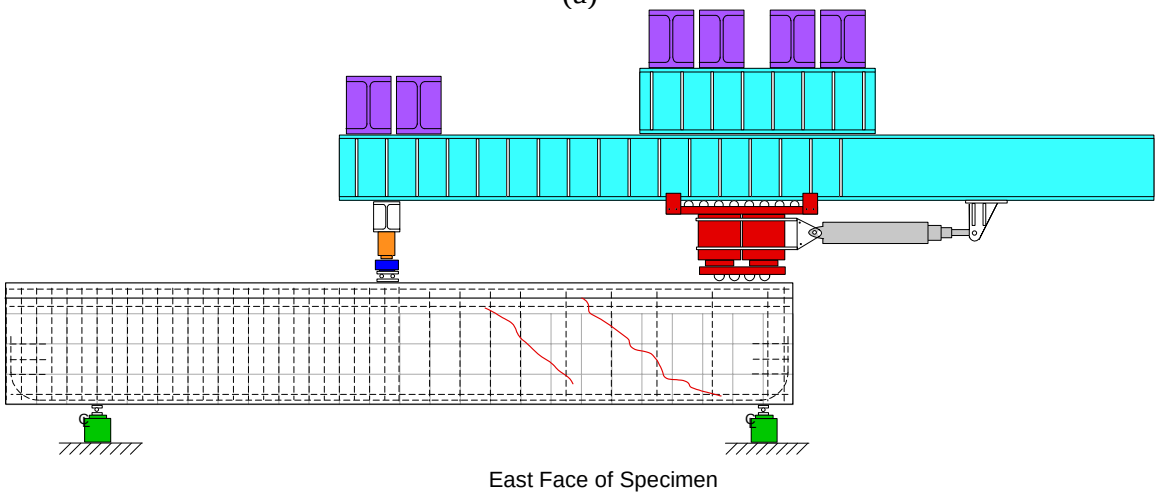

(b)

Figure 4.1: Schematic of the moving load apparatus, including horizontal rail (light blue), moving load dolly (red), support frames (purple), dead-load cylinder (orange), telescoping push-pull cylinder (grey), dead end reaction beam (yellow), reaction load cells (green) and dead-load load cell (dark blue). (a) Specimens C11T16.5-B2-ML, C11T22-B3-ML and C11T22-B4-ML were tested as cantilevered specimens. (b) Specimens C10T12-B2-ML and C11IT16-B1-ML were tested using simple supports.

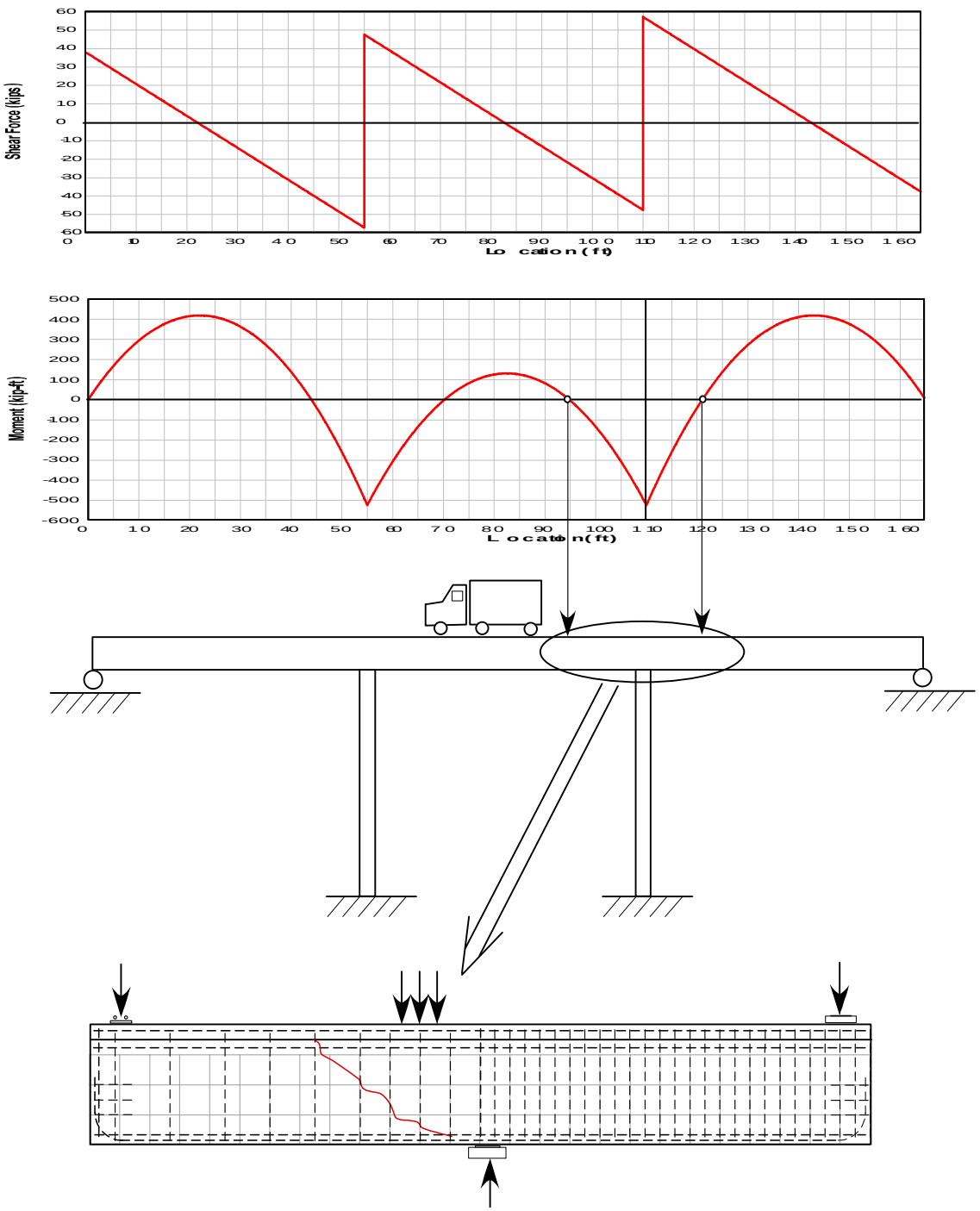

Figure 4.2: Cantilevered Specimens C11T16.5-B2-ML, C11T22-B3-ML and C11T22-B4-ML were configured to model the shear-moment behavior of continuous girders in the Springfield Bridge. The vertical support near the center of the specimen models the dead load shear in the existing bridge at the dead load point of inflection. Note that the applied moment is zero at the cantilever tip, which approximates the combined live and dead load moments at the dead load point of inflection. The moving load dolly models a moving tire patch load.

Figure 4.3: Moving load apparatus with cantilever supports

Figure 4.4: Moving load apparatus with cantilever supports

Figure 4.5: Moving load apparatus with simple supports

The horizontal rail was constructed of two (2) W14x122 column sections welded along the flange tips to form a rigid box. Web stiffeners, both internal and external, were installed to stiffen the web and to prevent web buckling due to heavy point loading from the dolly. The rail was supported by two steel frames placed 3.7 m (12 ft) apart. The load dolly traveled along the bottom flange of the horizontal rail and was used to apply moving loads to the specimen, as shown in Figure 4.6. The dolly consisted of two (2) 4450 kN (500 ton) double-acting hydraulic cylinders mounted between two (2) 75 mm (3 in) steel plates.

The force applied to the specimen was controlled by measuring the differential pressure acting on both sides of the cylinder areas using *Sensotec TJE,* 3000 psi (20 MPa) rated pressure transducers (Figure 4.7). Low-level signals from the pressure transducers were amplified in proportion to the area of the cylinders, and a difference amplifier circuit with unity gain was developed to supply a voltage feedback signal to an *MTS Flex Test SE* controller for closed-loop servo-hydraulic force control. Hardened steel roller bearings mounted on the upper and lower faces of the steel plates allowed the dolly to roll between the horizontal rail and a specimen positioned below. The roller bearings on the lower plate were configured to apply a 355 mm x 250 mm (14 in x 10 in) patch load to the specimen. This is slightly smaller than the AASHTO LRFD (1998) tire patch size of 510 mm x 255 mm (20 in x 10 in). Spherical bearings positioned between the cylinder heads and the lower plate allowed the plate to swivel up to 15 degrees in any direction to follow the deflected shapes of specimens and to ensure that all rollers achieved equal bearing. External reaction forces were measured using 2225 kN (500 kip) capacity load cells at the reaction points, which provided independent confirmation of the live load applied by the load dolly (Figure 4.8).

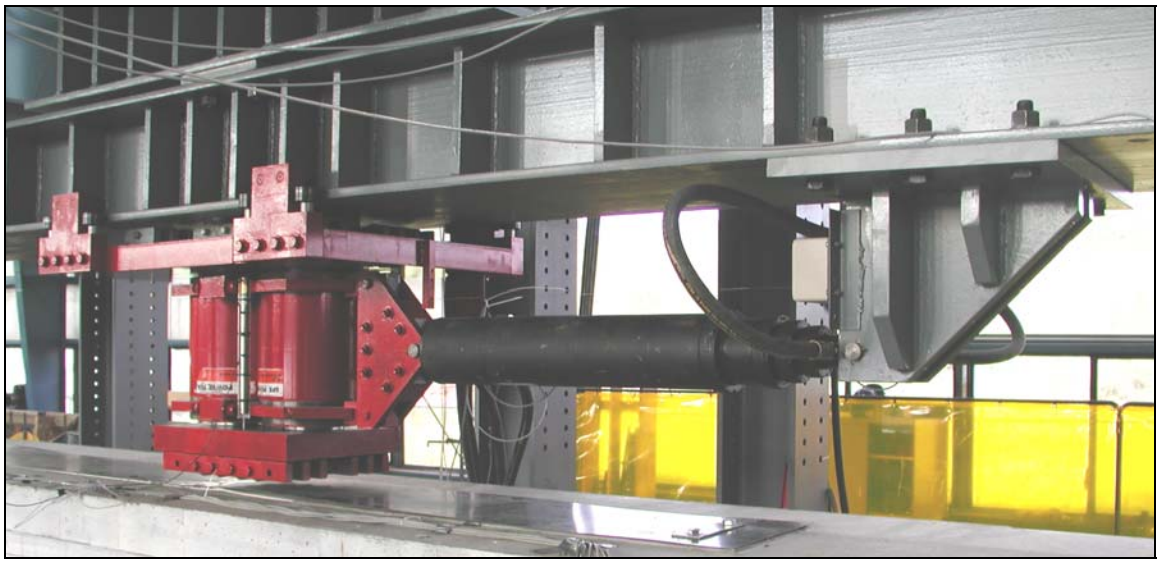

Figure 4.6: Moving load dolly (red) and telescoping push-pull cylinder

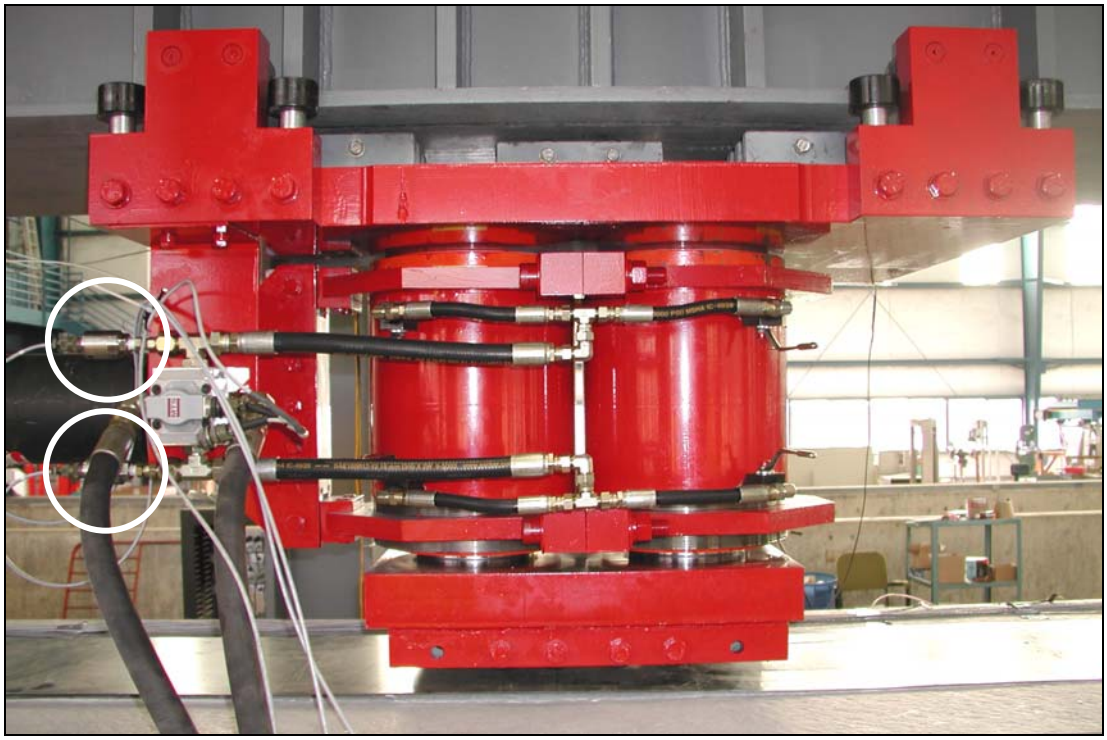

Figure 4.7: Moving load dolly and hydraulic connections, including the *Sensotec TGE* 3000 psi rated pressure transducers (circled) that enabled closed-loop servo-hydraulic force control.

Figure 4.8: 500 kip load cell simulating the bent cap reaction in the Springfield Bridge. The pinned bearing allowed the specimen to rotate under load.

The position of the load dolly was controlled using a push-pull telescoping hydraulic cylinder connected to the moving load dolly. A position transducer supplied a control signal to a second *MTS Flex-Test SE* controller, which provided position control of the dolly. The telescoping cylinder was designed to move the load dolly through a total travel of 3.7 m (12 ft) while the dolly applied full-scale moving loads to the specimen.

Simulated superimposed dead loads were applied by mounting an 890 kN (100 ton) hydraulic cylinder to the underside of the horizontal rail (Figure 4.9). The dead load cylinder was positioned to prevent contact with the moving load dolly and was connected to a hydraulic piston accumulator to maintain dead load pressure as the specimen deflected under load. The superimposed dead load was measured using a 245 kN (55 kip) load cell placed between the dead load cylinder and the specimen.

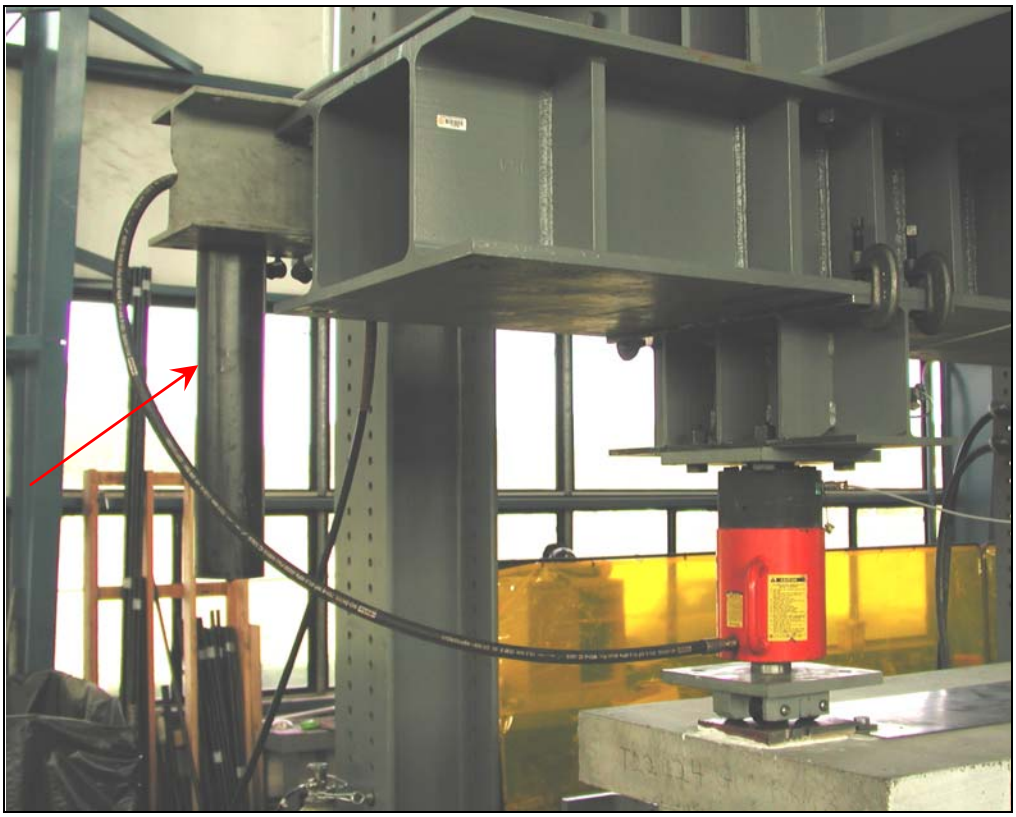

Figure 4.9: Dead load cylinder (orange) and hydraulic accumulator (arrow) used to maintain preset dead load as the beam deflected under live load. Roller bearing plate affixed to bottom of dead load cylinder to allowed flange to deflect without restriction of movement.

The moving load apparatus was designed to operate under hydraulic pressure of 20 MPa (3000 psi). At this pressure rating, the moving load apparatus has a maximum live load design capacity of 2135 kN (480 kips). During this testing program the apparatus was proof loaded to a live load of 1670 kN (375 kips). Due to the configuration of the hydraulic controls, the apparatus is capable of applying moving loads of variable speed in both directions (pushing and pulling) and can apply varying loads as a function of position.

5.0 TESTING PROCEDURES

5.1 LOADING PROTOCOL

A combination of live (moving) and superimposed dead (stationary) loads were applied to each specimen. The superimposed dead load was determined from the structural drawings of the Springfield Bridge. The dead load included a 50 mm (2 in) asphalt wearing surface with an additional 50 mm (2 in) asphalt overlay. The reinforced concrete unit weight was assumed to be 2400 kg/m^3 (150 pcf) and the asphalt unit weight was assumed to be 2080 kg/m^3 (130 pcf). The dead load was computed as 24.8 kN/m (1.7 kips/ft) and was applied uniformly to each of the four girders. The resulting unfactored dead load shear and moment diagrams for an individual Springfield Bridge girder are shown in Figure 5.1 and Figure 5.2. A unique live load history was applied to each specimen, but in general, predetermined magnitudes of constant and/or variable live loads were applied across a predetermined length of the test span. The magnitude of the live load was increased until failure of the specimen was achieved. Typical live load and member response histories for cantilever and simply supported specimens are shown in Figure 5.3. More detailed descriptions of the loading protocols used for each of the specimens are provided below.

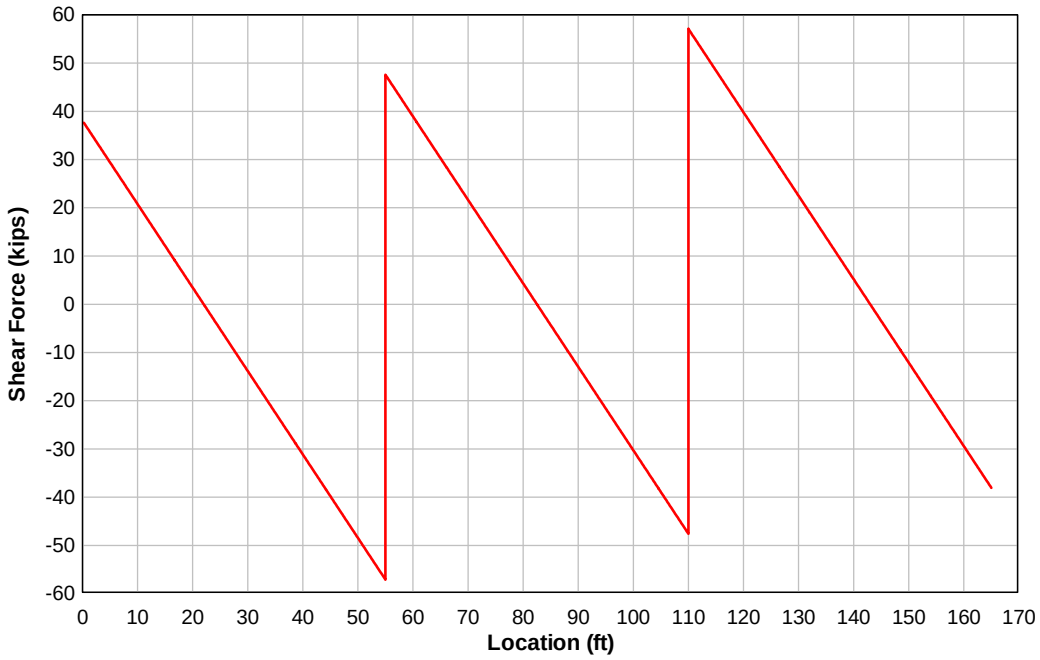

Figure 5.1: Dead load shear for an individual girder of the Springfield Bridge

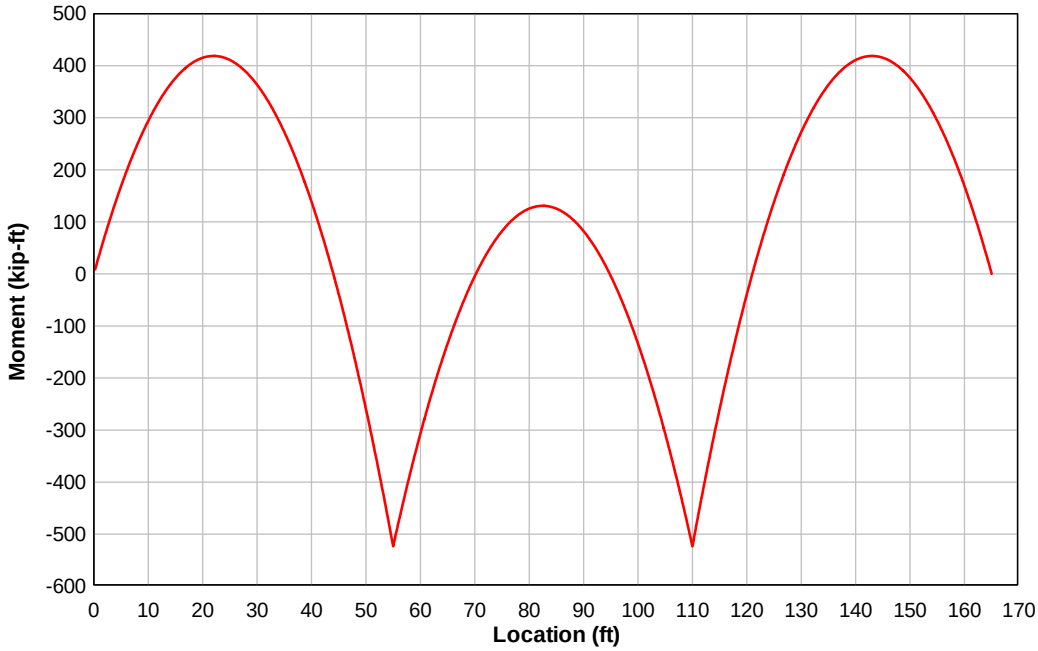

Figure 5.2: Dead load moments for an individual girder of the Springfield Bridge.

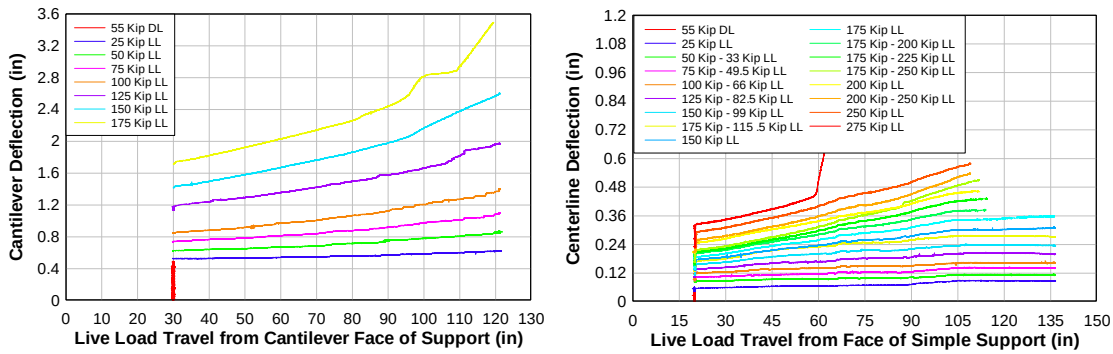

(a) **(b)**

Figure 5.3: Typical imposed dead and live load protocols and specimen response for (a) cantilever supports and (b) simple supports.

5.2 C11T22-B3-ML

A constant live load protocol was used to induce failure of the cantilevered specimen. A stationary superimposed dead load of 245 kN (55 kips) was applied at a point 2.76 m (9.04 ft) from the cantilever face of support, modeling the existing dead load shear at the Springfield Bridge dead load points of inflection. Constant-value live loads were then applied beginning at a

point 0.76 m (2.5 ft) from the face of support and ending at a point 3.07 m (10.08 ft) from the face of support. The total live load travel was 2.31 m (7.58 ft). The initial live load was approximately 111 kN (25 kips). The live load was increased by 111 kN (25 kip) with each successive live load pass. A detailed view of the support and loading conditions is provided in Figure 5.4. The live load history is shown in Figure 5.5 as a function of live load position at each load step. The superimposed dead load history is shown in Figure 5.6. The centerline and dead load end support reactions are shown in Figures 5.7 and 5.8, respectively, as a function of live load position for each load step. The specimen deflection is shown in Figure 5.9.

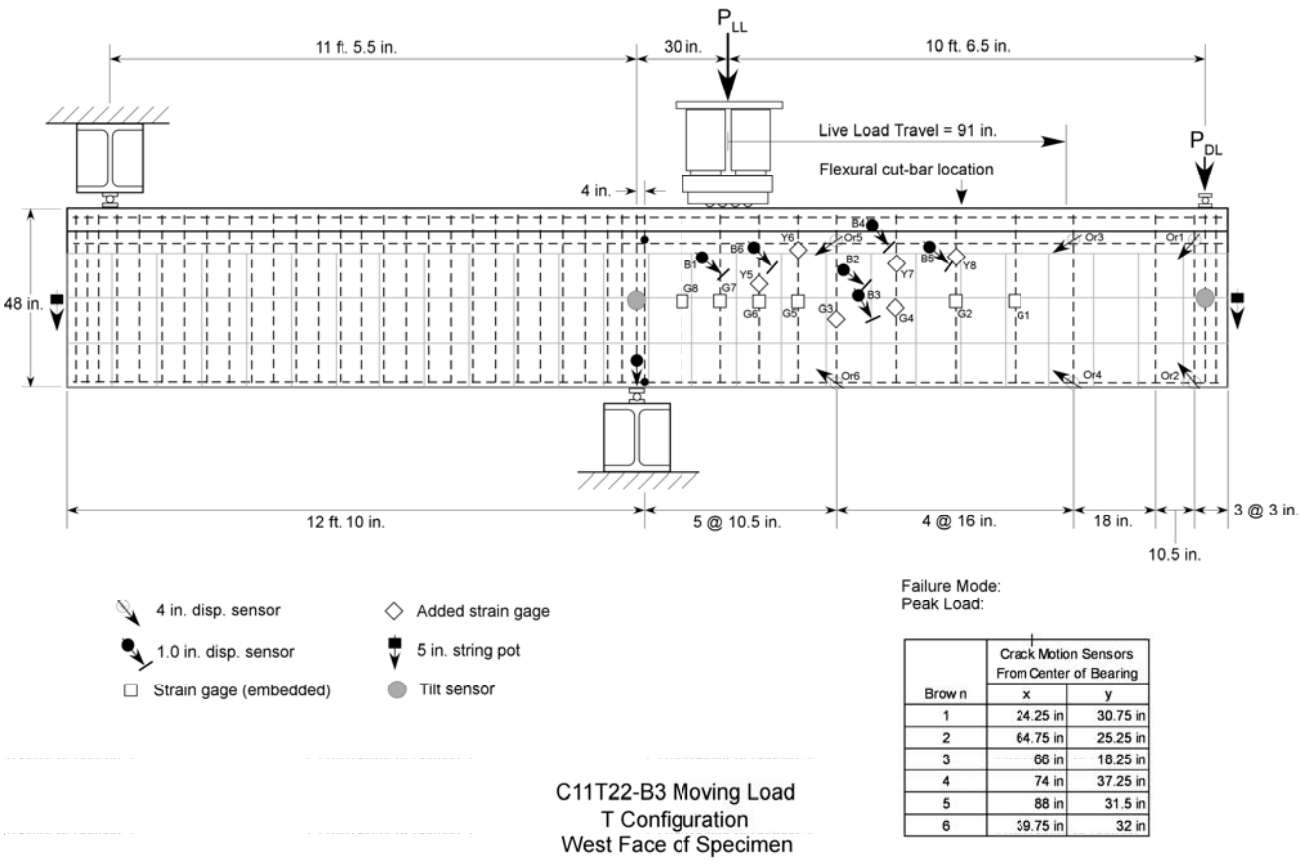

Failure Mode:
Peak Load:

Brown	Crack Motion Sensors From Center of Bearing x	y
1	24.25 in	30.75 in
2	64.75 in	25.25 in
3	66 in	18.25 in
4	74 in	37.25 in
5	88 in	31.5 in
6	39.75 in	32 in

Figure 5.4: Support, loading conditions and instrumentation for Specimen C11T22-B3-ML.

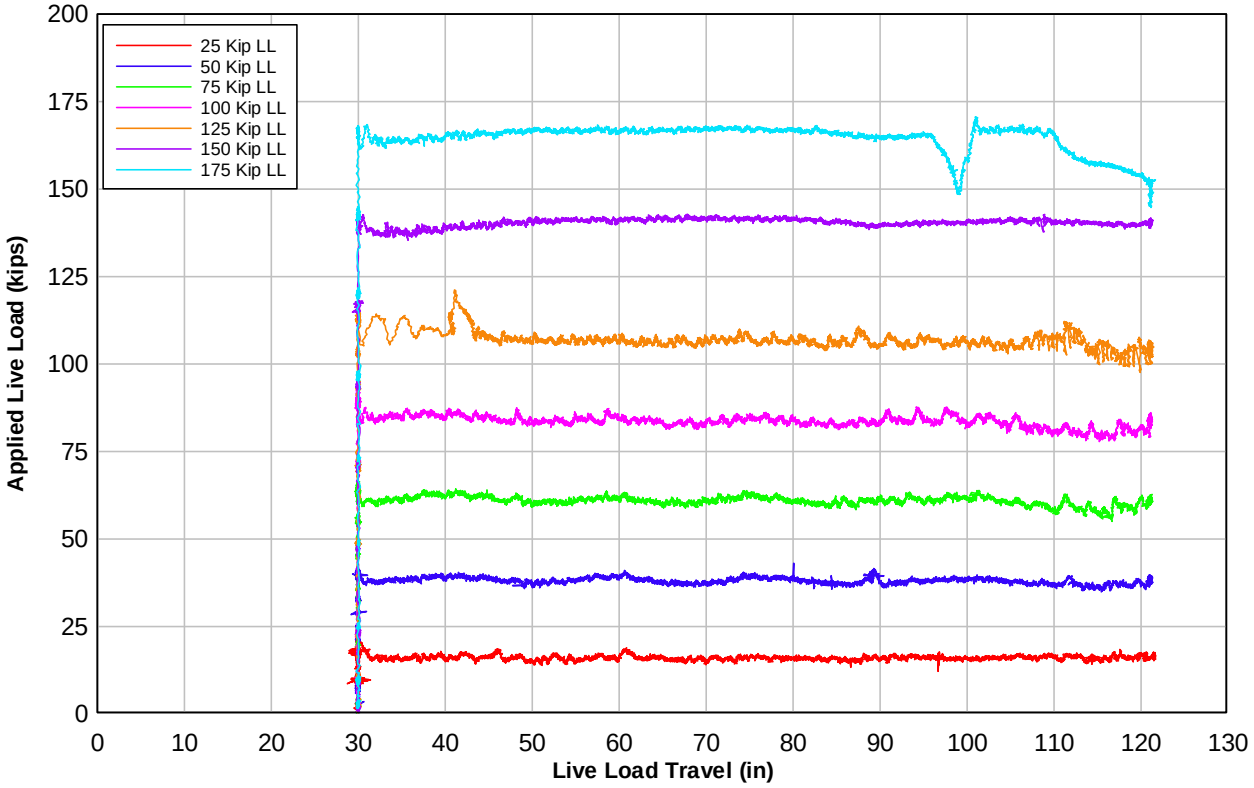

Figure 5.5: Live load history for Specimen C11T22-B3-ML as a function of live load position and load step.

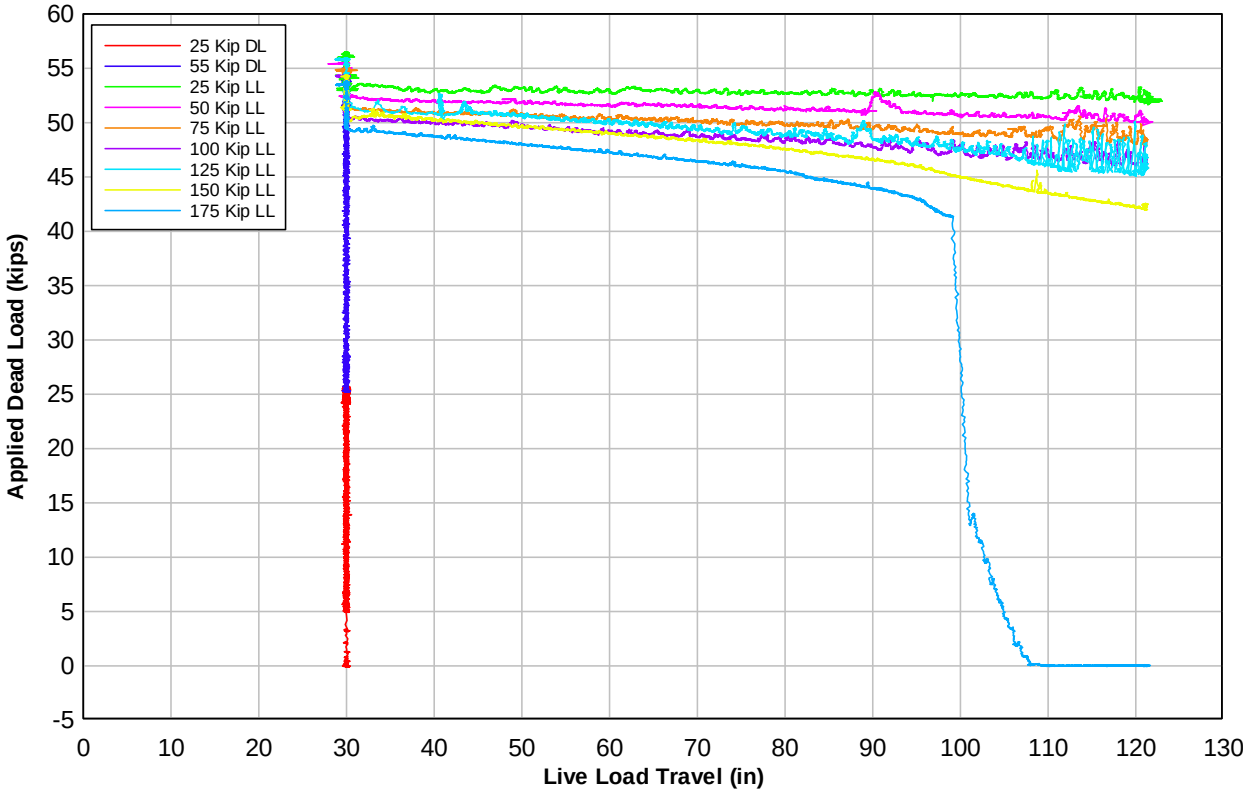

Figure 5.6: Dead load history for Specimen C11T22-B3-ML as a function of live load position and load step.

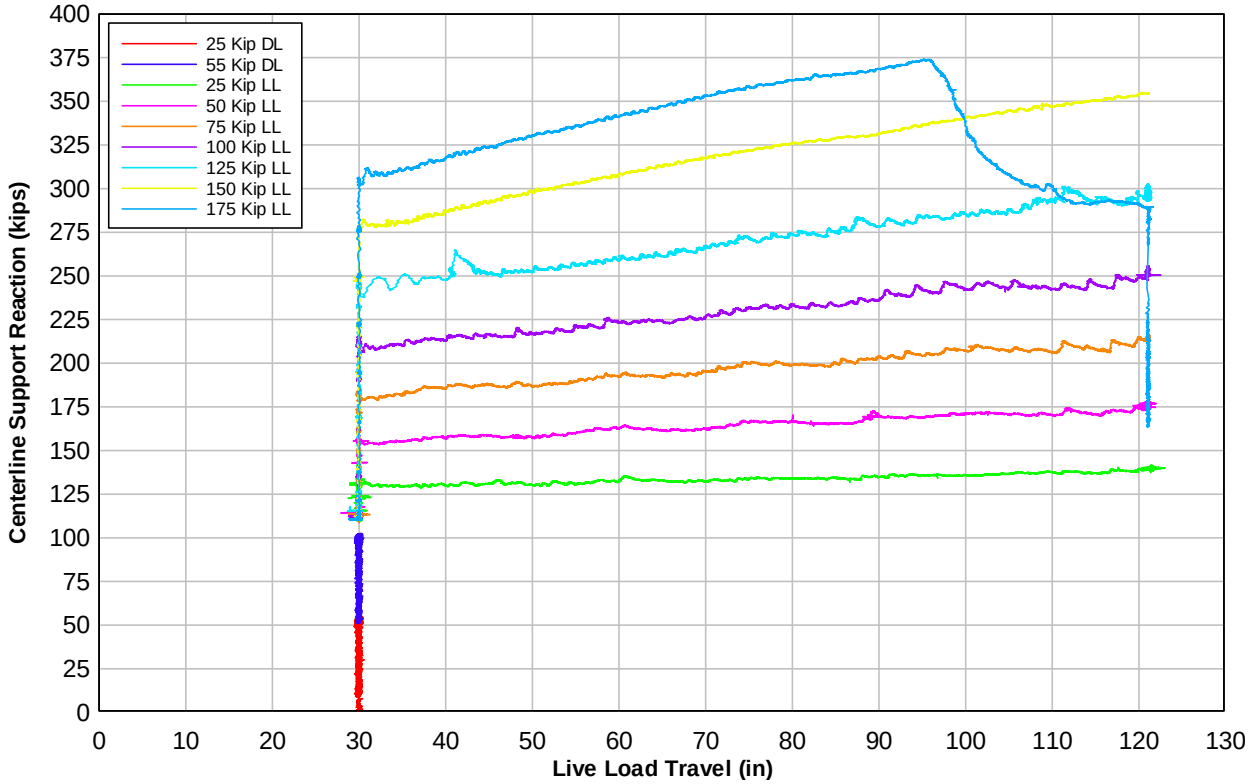

Figure 5.7: Centerline support reaction for Specimen C11T22-B3-ML as a function of live load position and load step.

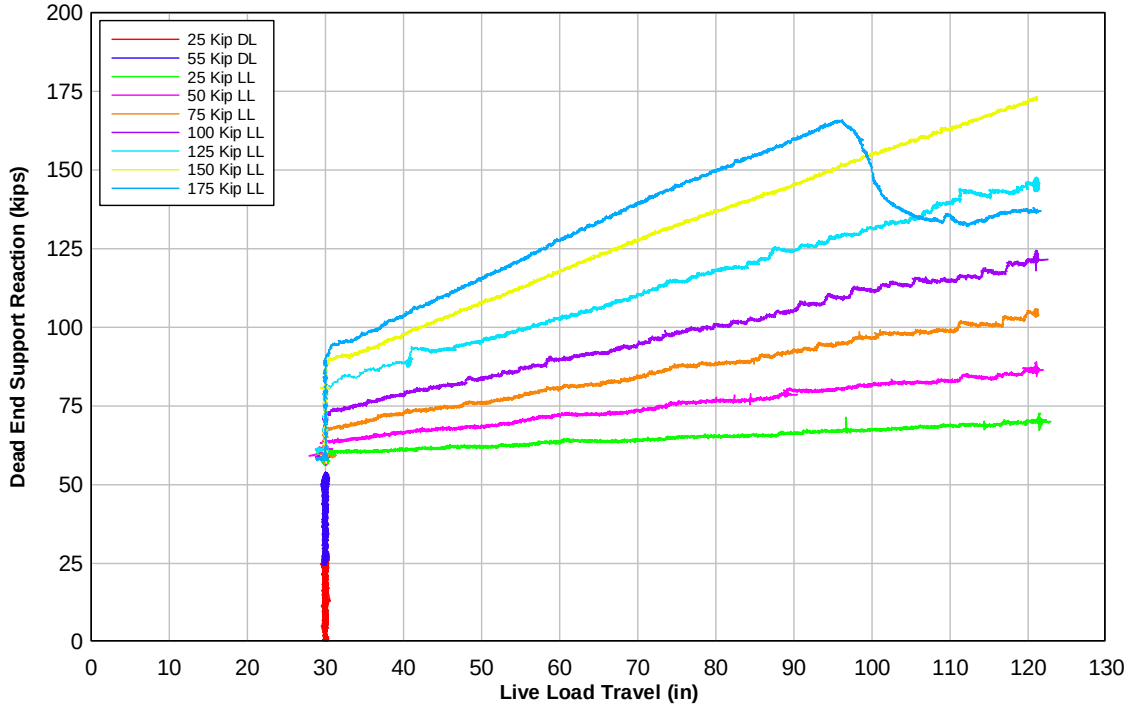

Figure 5.8: Dead end support reaction for Specimen C11T22-B3-ML as a function of live load position and load step.

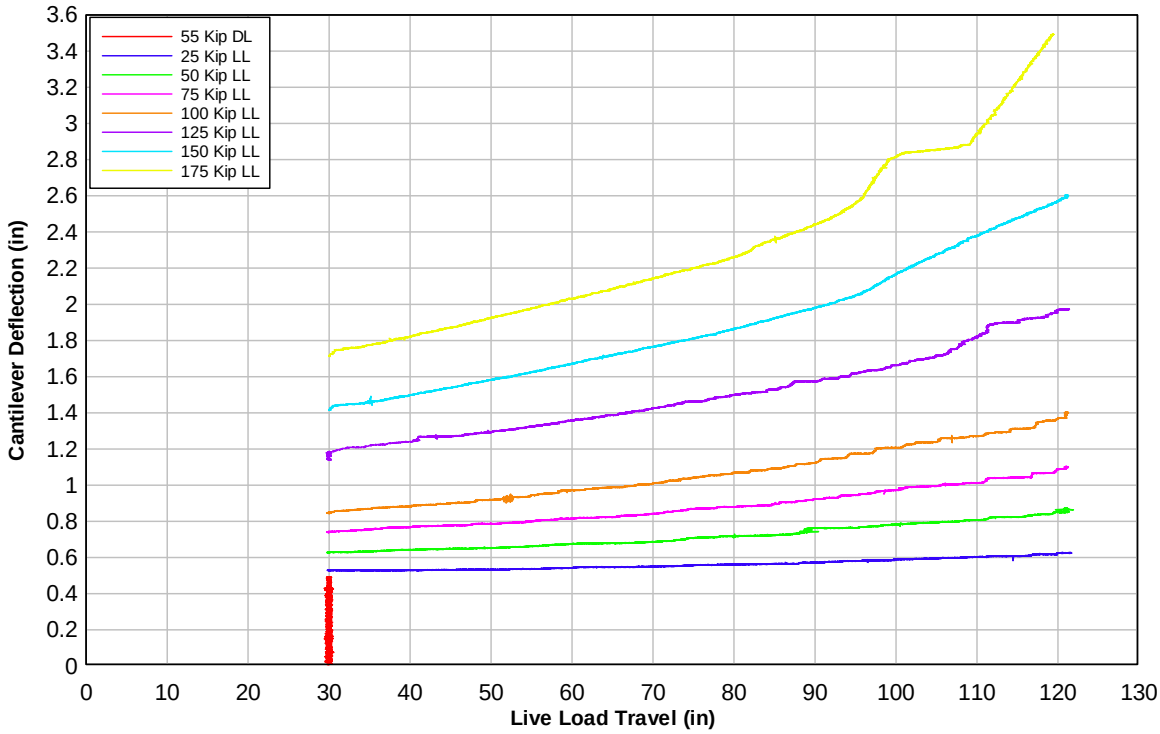

Figure 5.9: Corrected cantilever deflection for Specimen C11T22-B3-ML as a function of live load position and load step.

5.3 C11T22-B4-ML

The cantilevered specimen was subjected to moving loads with the live load magnitude changing as a function of live load position. Linearly varying live loads were used to induce shear-moment interactions in the specimen that approximated the shape of shear-moment interactions induced by truck loads near the continuous supports of the Springfield Bridge (Figure 2.5 and 6.15 through 6.24). The linearly varying loads also served to increase the shear-to-moment ratio near the support compared to Specimen C11T22 B3 ML. The shear-moment ratio was also modified by decreasing the dead load magnitude to 156 kN (35 kips).

Live loads were applied beginning at a point 305 mm (12 in) from the face of support to a point 3.07 m (10.08 ft) from the face of support. The total live load travel was 2.77 m (9.08 ft). The load near the support was increased in 111 kN (25 kip) increments and tapered linearly to a constant value of 111 kN (25 kips) near the cantilever end. When the initial live load reached 1000 kN (225 kips), the ending load near the cantilever tip was increased and the load process repeated. A detailed view of the specimen support and loading conditions is shown in Figure 5.10. The live load history is shown in Figure 5.11 as a function of live load position and load step, which also serves to illustrate the variable shear-moment interactions that were induced. The superimposed dead load history is shown in Figure 5.12. The centerline support and dead load end support reactions are shown in Figures 5.13 and 5.14. Specimen deflection is shown in Figure 5.15.

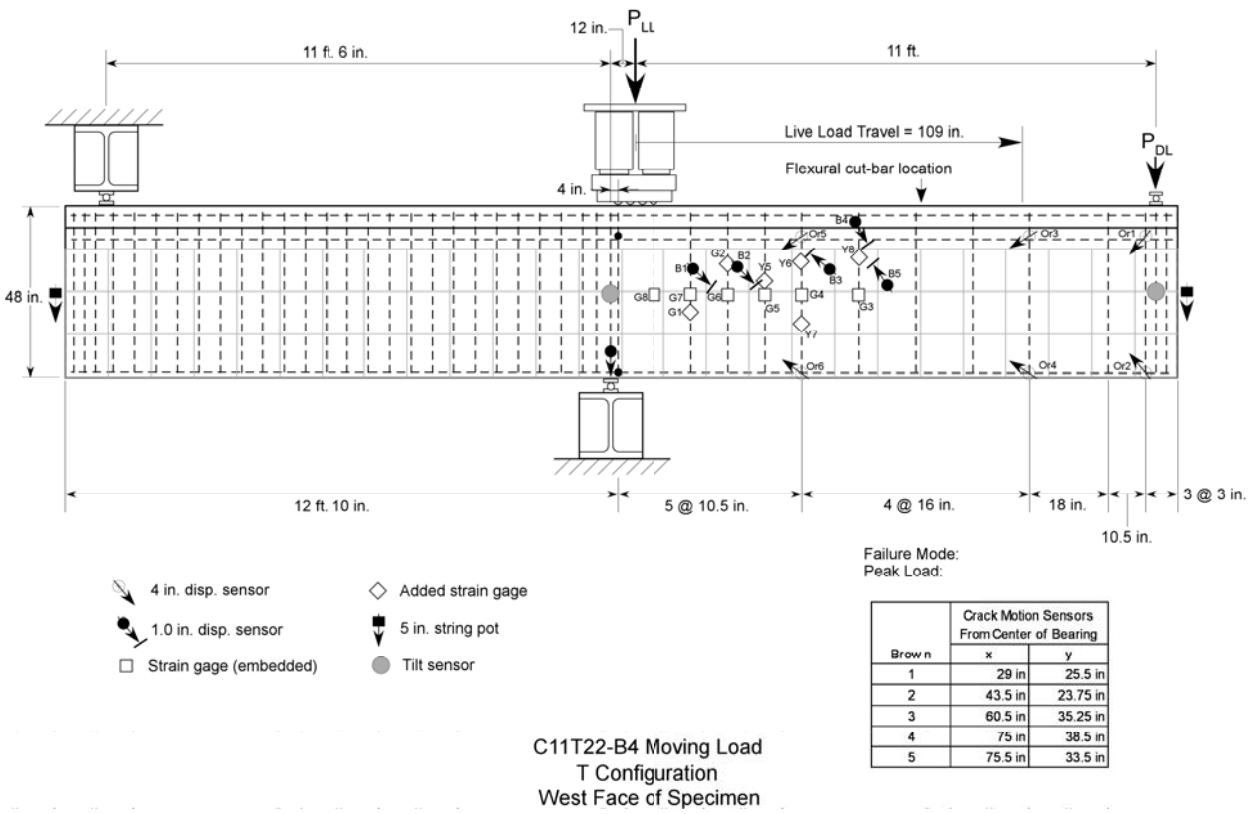

Brown	Crack Motion Sensors From Center of Bearing x	y
1	29 in	25.5 in
2	43.5 in	23.75 in
3	60.5 in	35.25 in
4	75 in	38.5 in
5	75.5 in	33.5 in

Figure 5.10: Support, loading conditions and instrumentation for Specimen C11T22-B4-ML

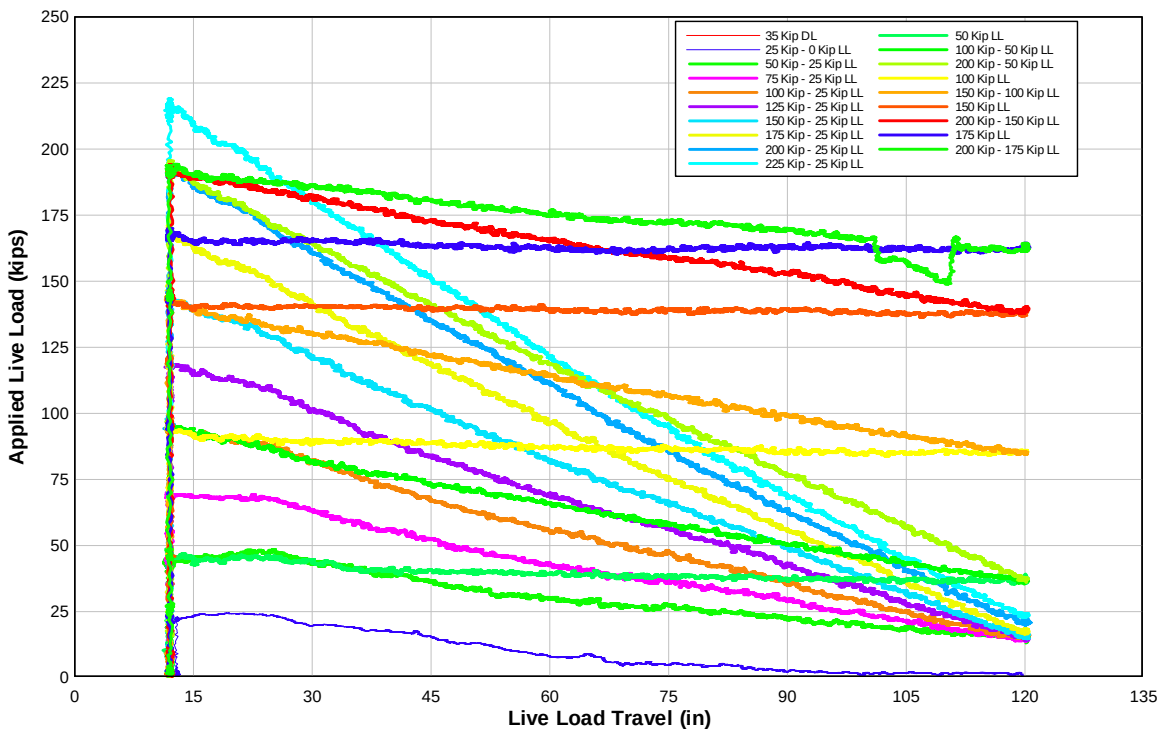

Figure 5.11: Live load history for Specimen C11T22-B4-ML as a function of live load position and load step.

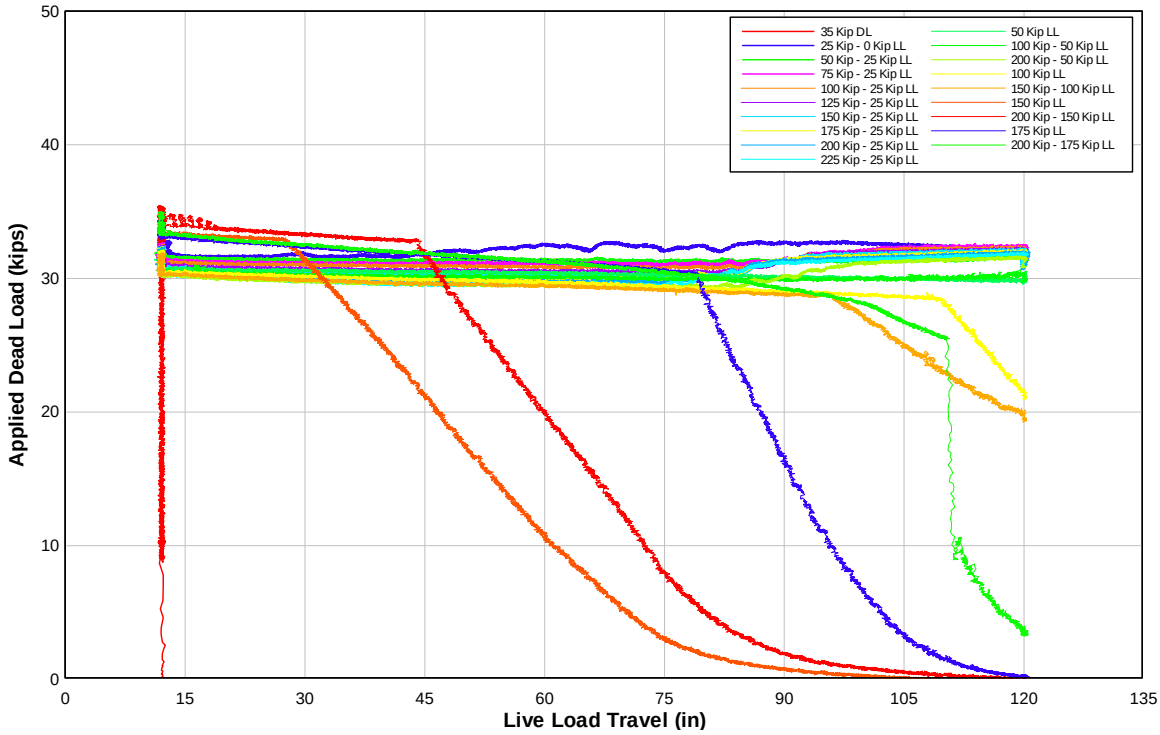

Figure 5.12: Dead load history for Specimen C11T22-B4-ML as a function of live load position and load step.

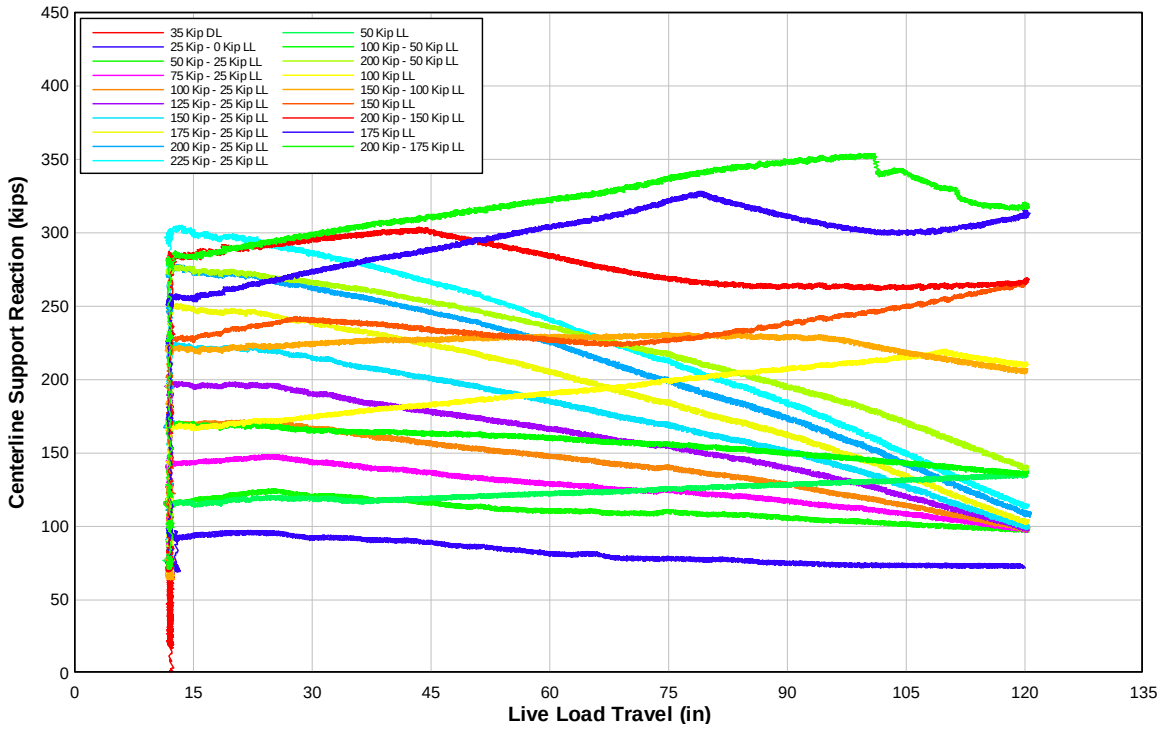

Figure 5.13: Centerline support reaction for Specimen C11T22-B4-ML as a function of live load position and load step.

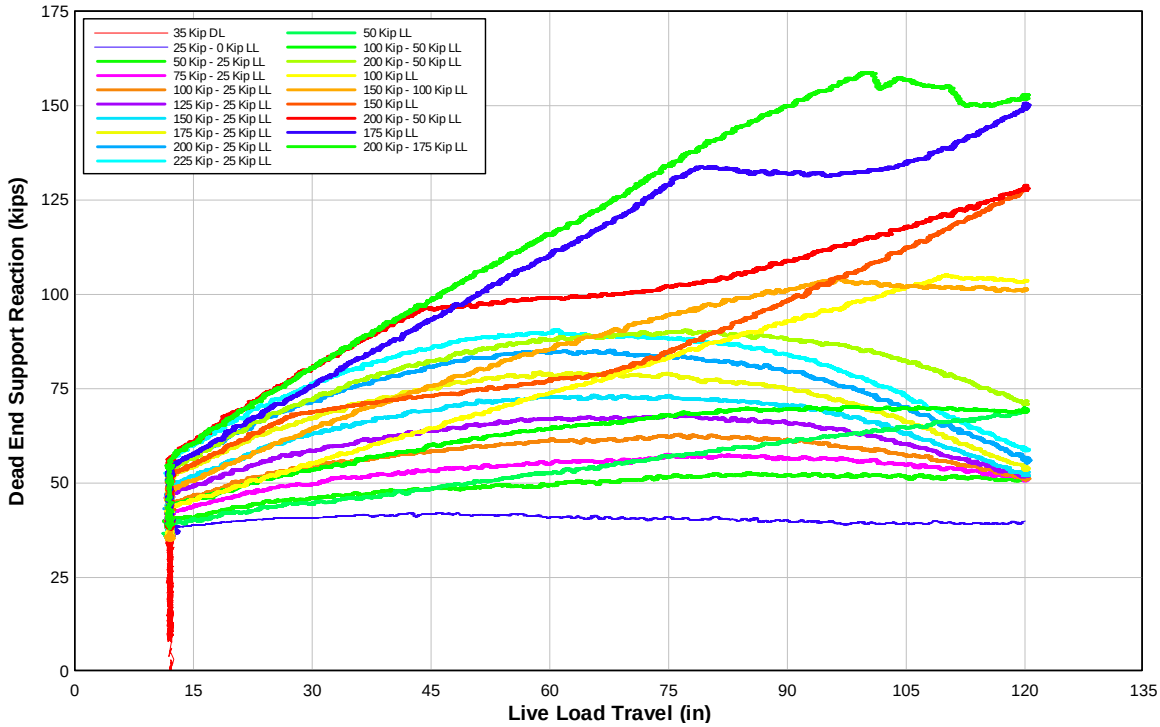

Figure 5.14: Dead end support reaction for Specimen C11T22-B4-ML as a function of live load position and load step.

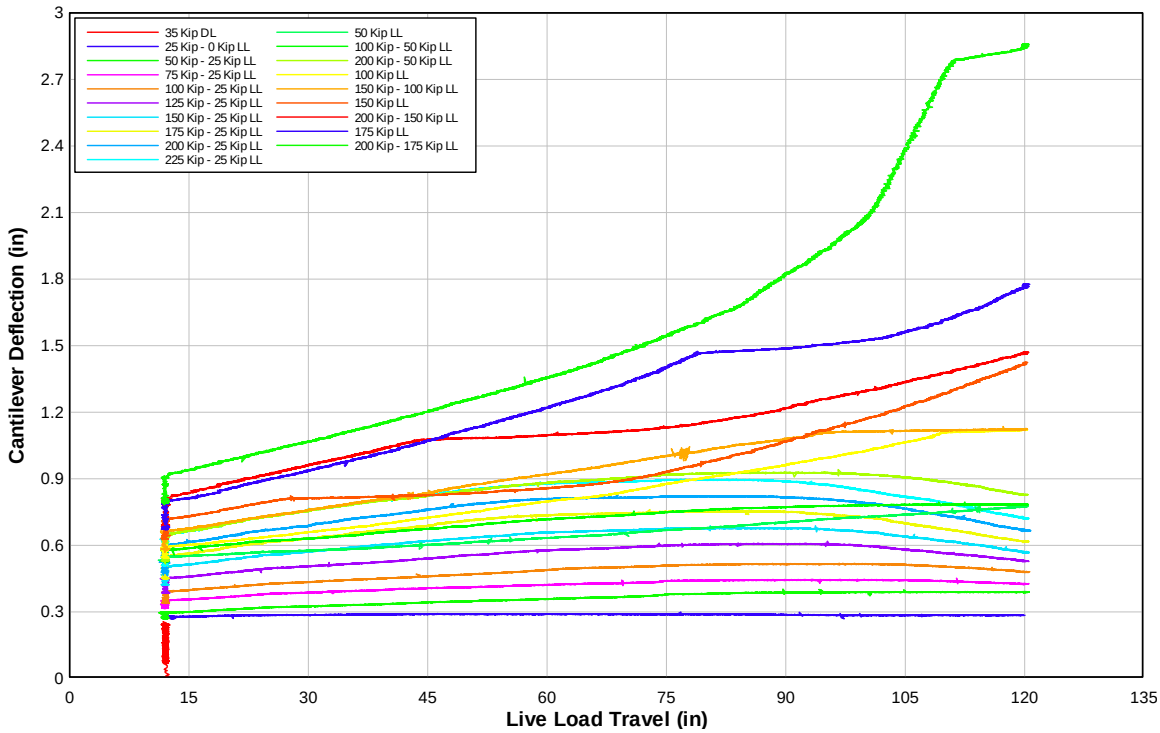

Figure 5.15: Corrected cantilever deflection for Specimen C11T22-B4-ML as a function of live load and load step.

5.4 C11T16.5-B2-ML

The cantilevered specimen was subjected to a combination of constant and tapered live loads. The constant loading was used to induce shear-moment interactions consistent with the first live load test. This provided a comparison between the shear and moment capacities for a specimen with equivalent ACI 318-02 shear capacity (C11T22-B3-ML) and equivalent stirrup spacing (C11T16.5-B2-ML) as the Springfield Bridge. A detailed view of the specimen supports and loading conditions is shown in Figure 5.16. The live load was applied in 111 kN (25 kip) increments as shown in Figure 5.17. Once the live load magnitude reached 780 kN (175 kips) it was tapered downward as the load moved toward the cantilever tip. This was done to eliminate the risk of a moment induced failure at the centerline support. The centerline and dead load end support reactions are shown in Figures 5.18 and 5.19, respectively, as a function of live load position for each load step. The specimen deflection is shown in Figure 5.20. No superimposed dead load was applied to this specimen.

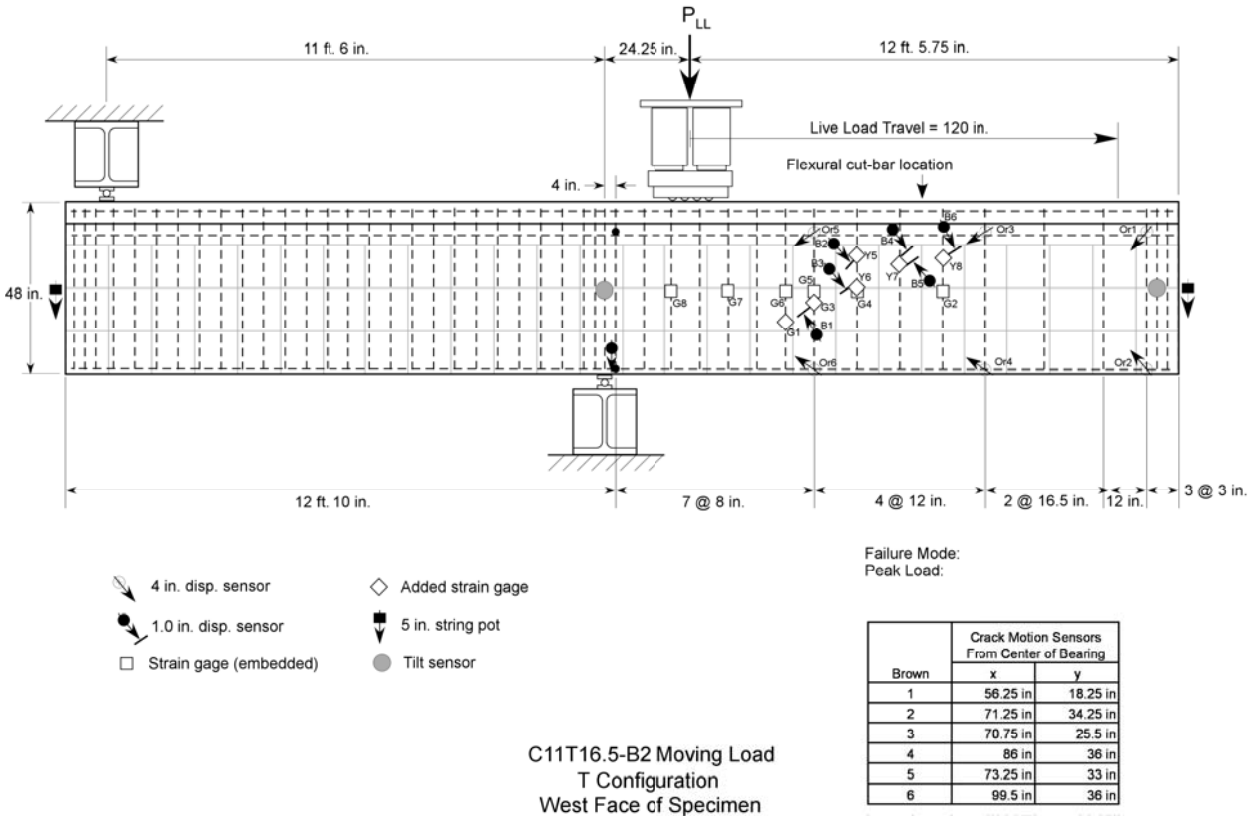

Brown	Crack Motion Sensors From Center of Bearing	
	x	y
1	56.25 in	18.25 in
2	71.25 in	34.25 in
3	70.75 in	25.5 in
4	86 in	36 in
5	73.25 in	33 in
6	99.5 in	36 in

Figure 5.16: Supports, loading conditions and instrumentation for Specimen C11T16.5-B2-ML.

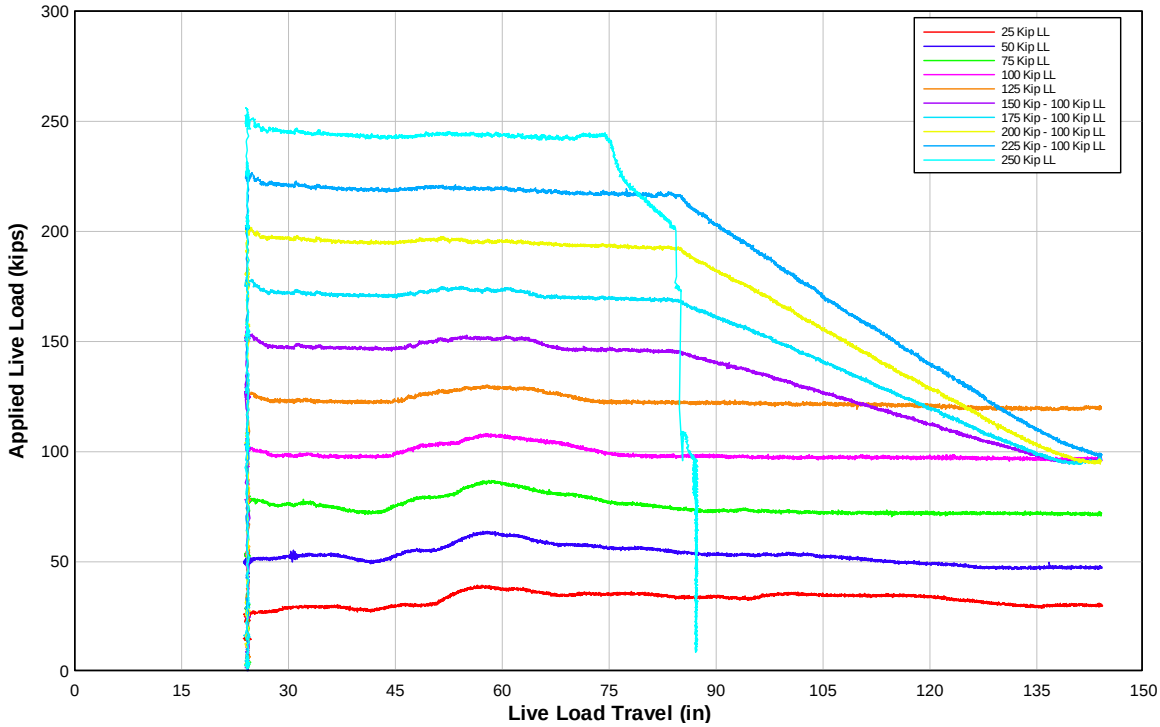

Figure 5.17: Live load history for Specimen C11T16.5-B2-ML as a function of live load position and load step.

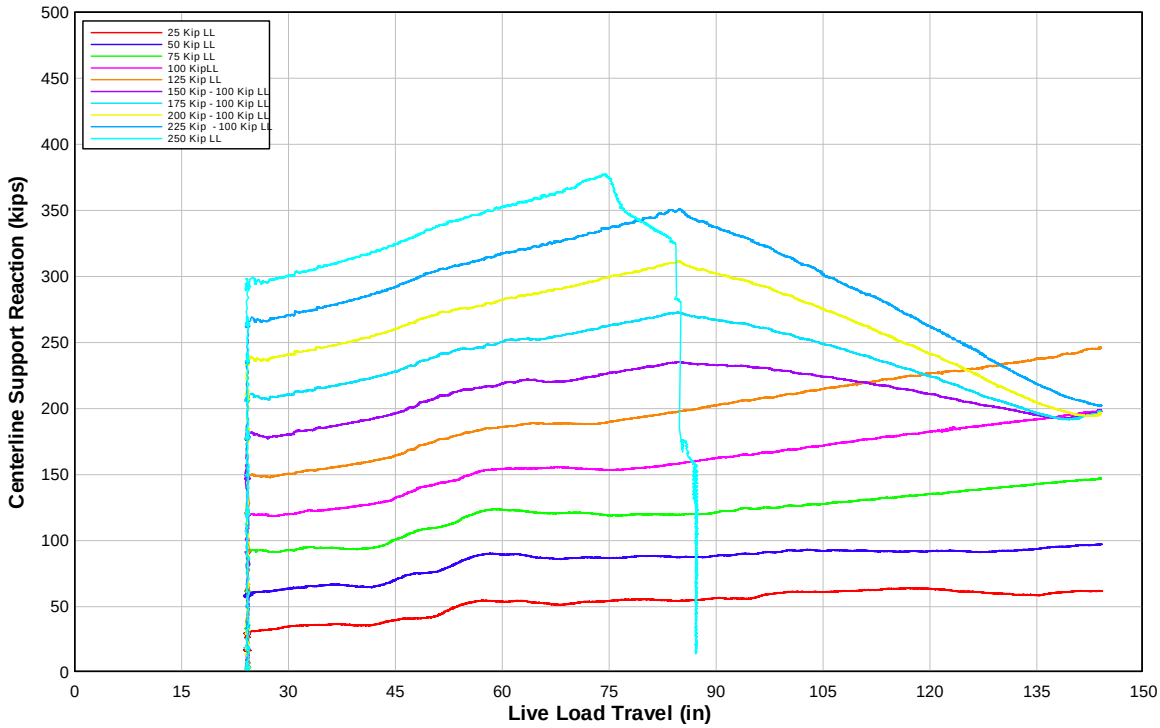

Figure 5.18: Centerline support reaction for Specimen C11T16.5-B2-ML as a function of live load position and load step.

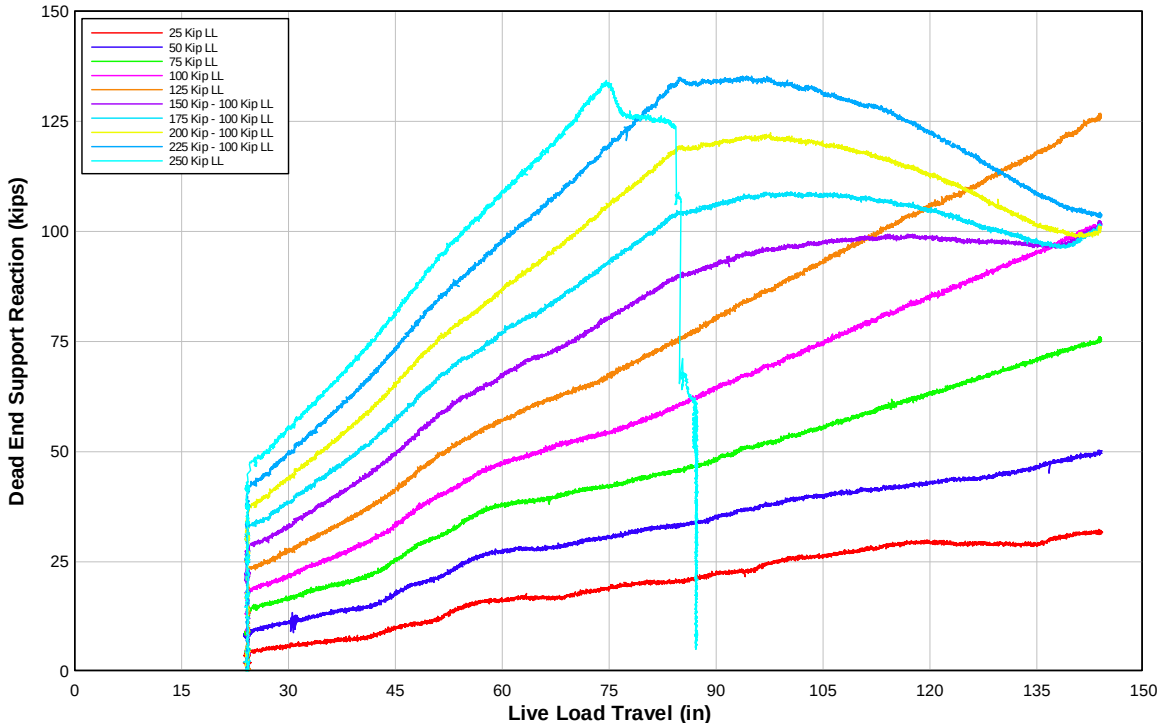

Figure 5.19: Dead end support reaction for Specimen C11T16.5-B2-ML as a function of live load position and load step.

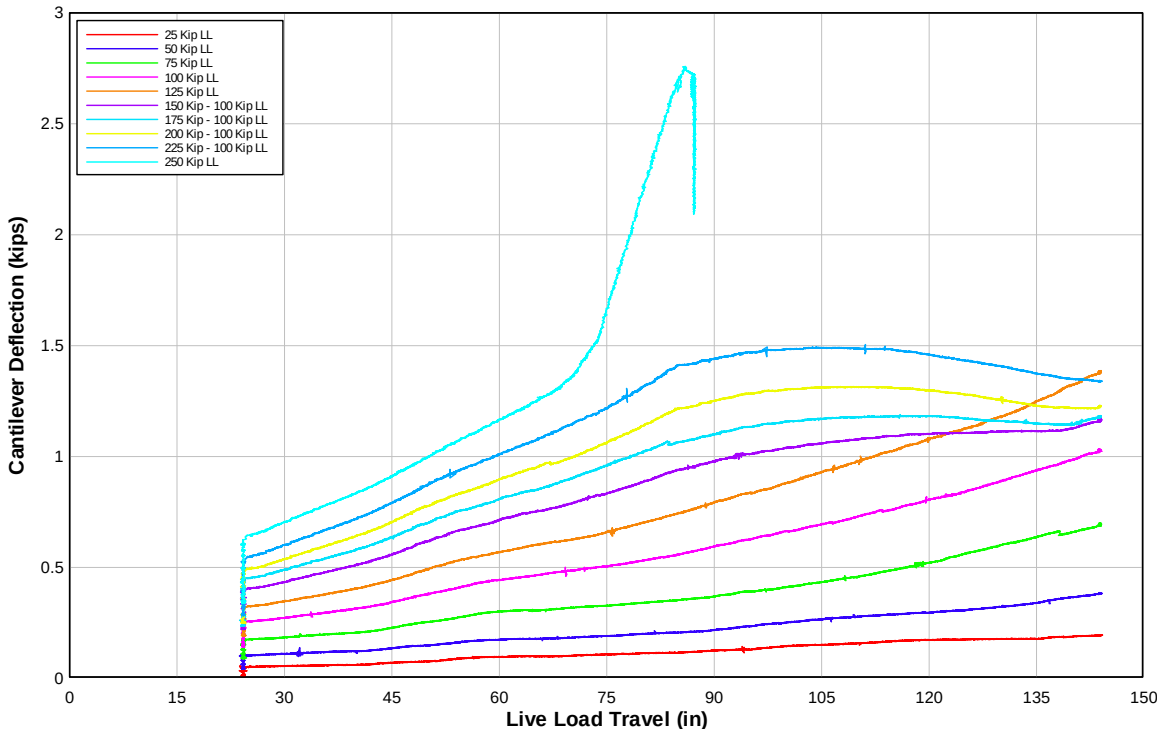

Figure 5.20: Corrected cantilever deflection for Specimen C11T16.5-B2-ML as a function of live load position and load step.

5.5 C10T16-B2-ML

The specimen was subjected to a combination of constant and tapered live loads. Initially, the live load was tapered to approximate the shear and moment interaction induced by truck loads near the simply supported ends of the Springfield Bridge (Figure 2.3). Early in the loading protocol, a diagonal crack developed near the face of support extending upward at approximately 45º. Once the live load reached about 780 kN (175 kips) the crack became quite large and no additional diagonal cracks developed. Therefore, the live load taper was reversed in order to encourage diagonal cracking away from the support. A detailed view of support and loading conditions is shown in Figure 5.21. Live and dead load histories are shown in Figure 5.22 and 5.23, respectively. The north support reaction and centerline deflections are shown in Figures 5.24 and 5.25, respectively, as a function of live load position for each load step.

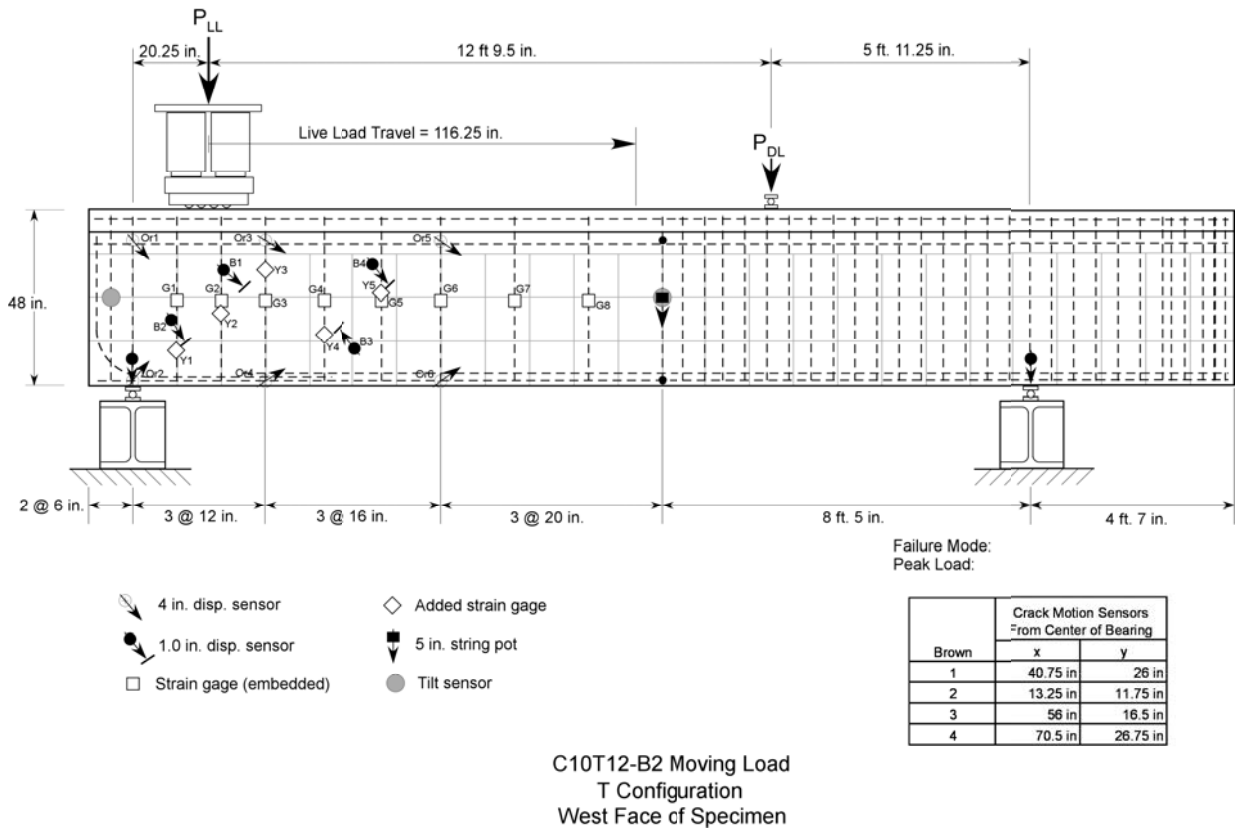

Brown	Crack Motion Sensors From Center of Bearing	
	x	y
1	40.75 in	26 in
2	13.25 in	11.75 in
3	56 in	16.5 in
4	70.5 in	26.75 in

Figure 5.21: Supports, loading conditions and instrumentation for Specimen C10T12-B2-ML.

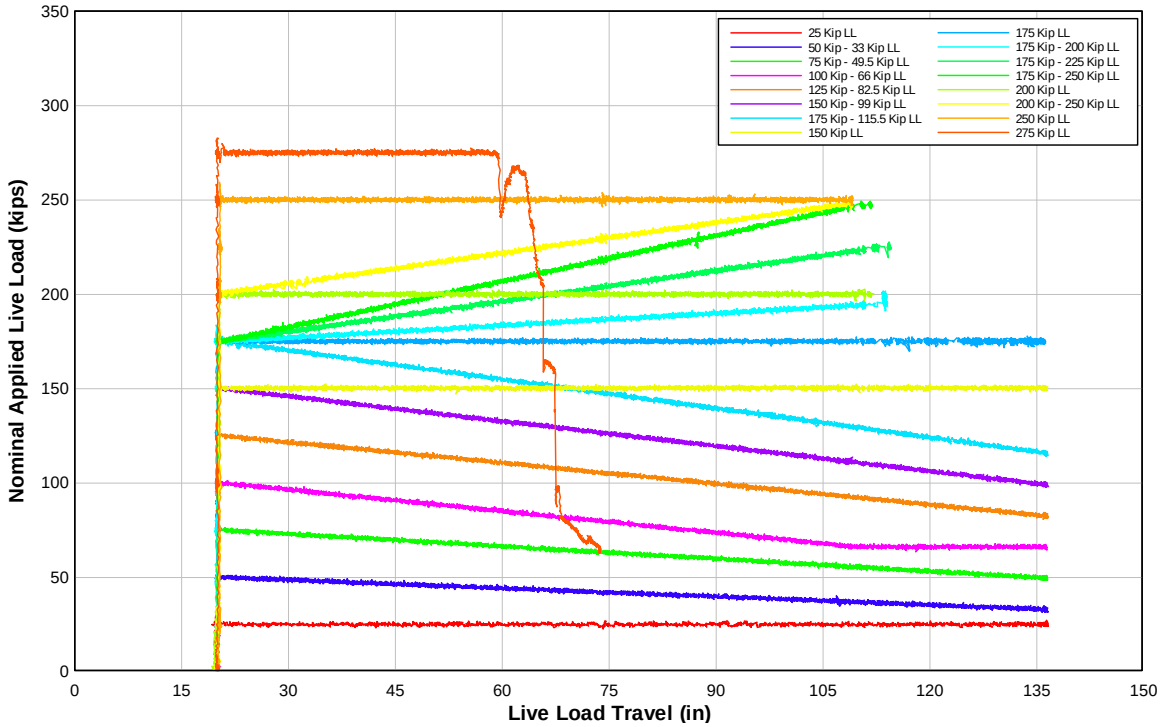

Figure 5.22: Live load history for Specimen C10T12-B2-ML as a function of live load position and load step.

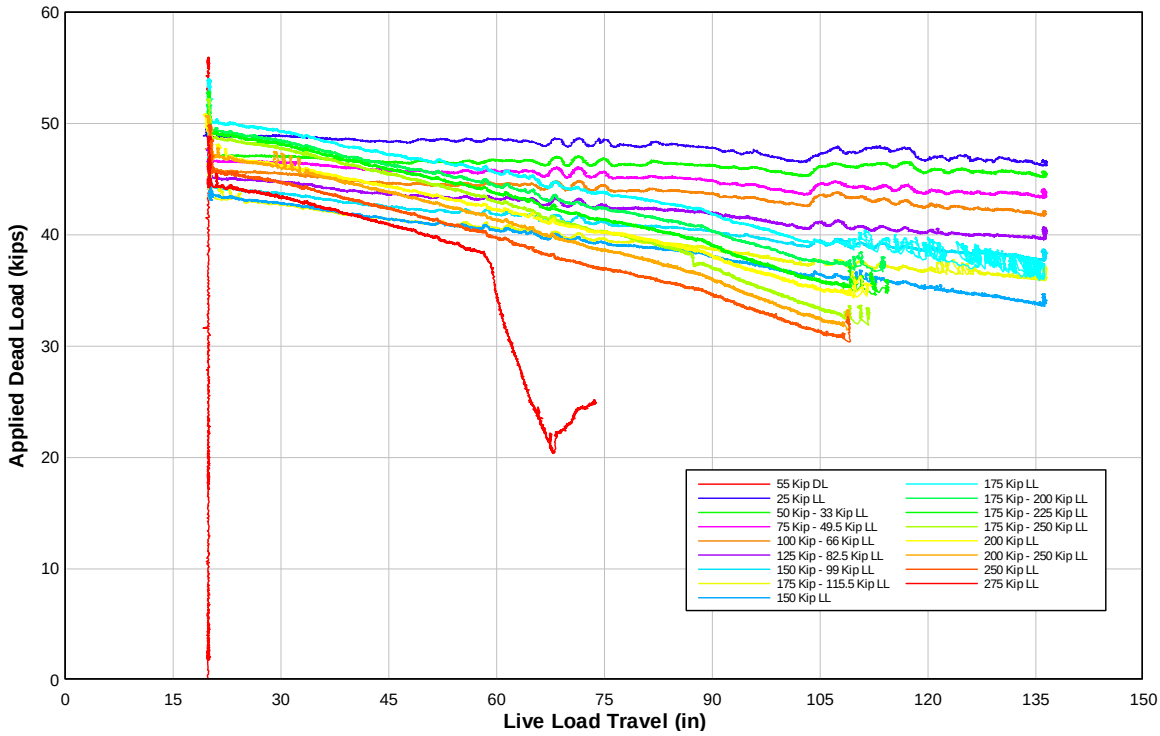

Figure 5.23: Dead load history for Specimen C10T12-B2-ML as a function of live load position and load step.

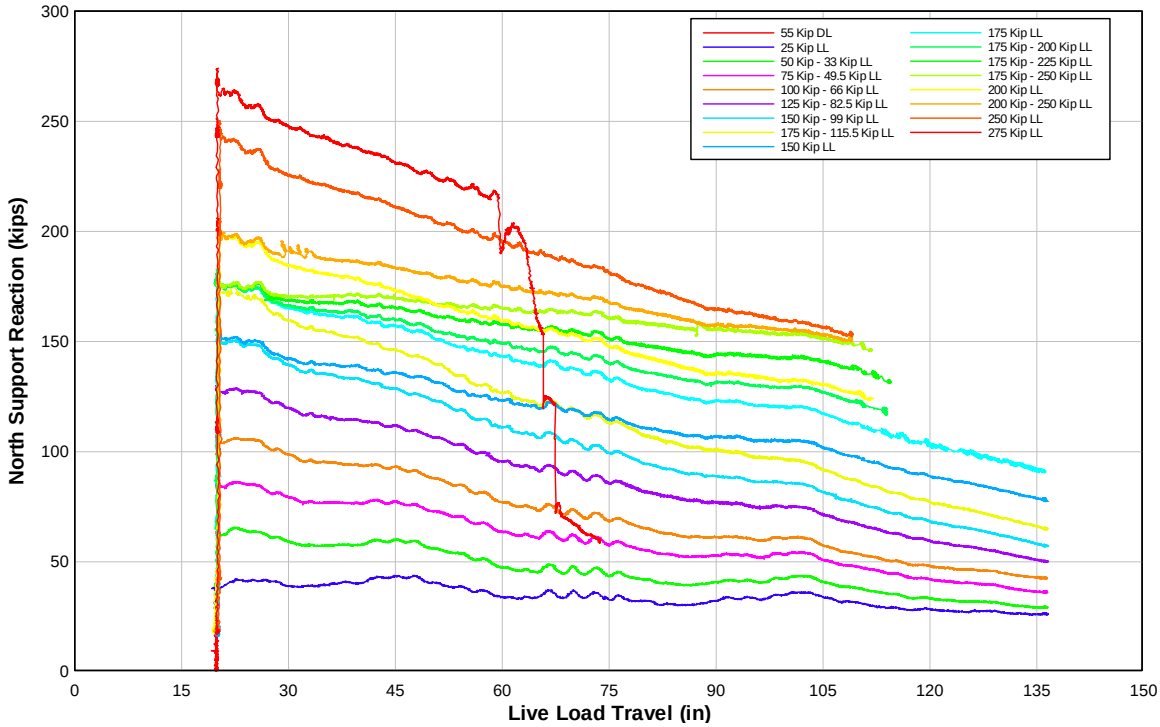

Figure 5.24: Left hand support reaction for Specimen C10T12-B2-ML as a function of live load position and load step.

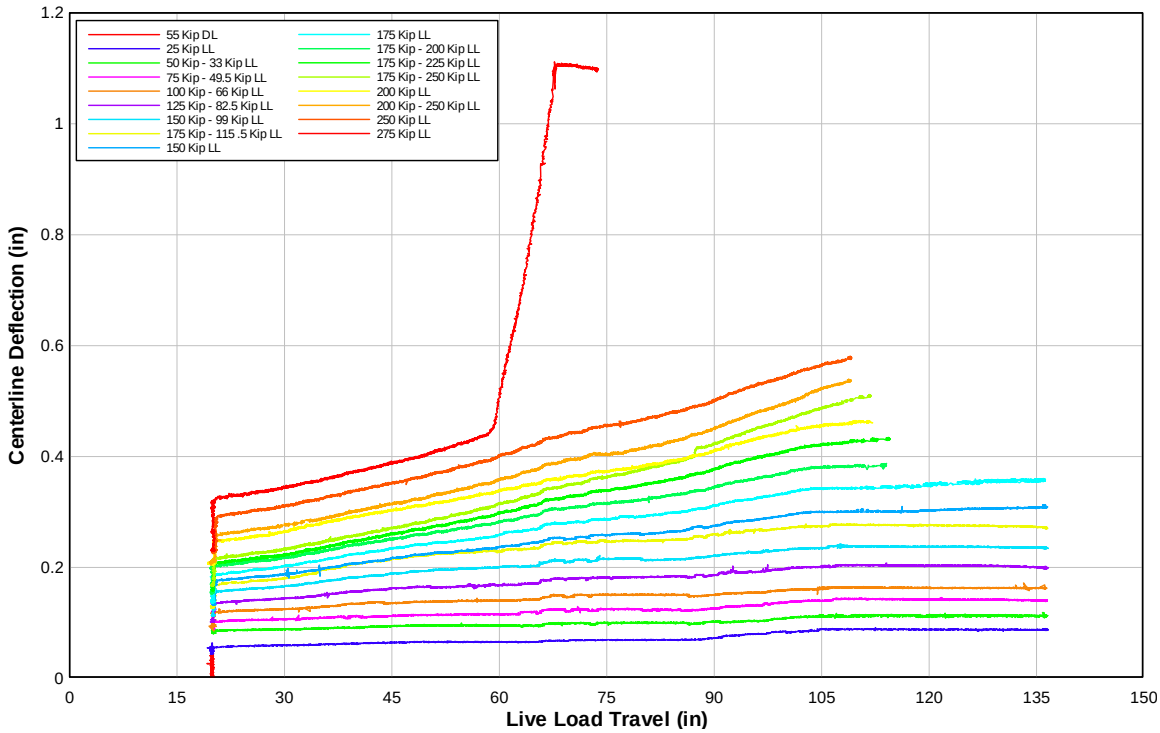

Figure 5.25: Corrected centerline deflection for Specimen C10T12-B2-ML as a function of live load position and load step.

5.6 C11IT16-B1-ML

The simply supported specimen was subjected to monotonic loading as shown in Figure 5.26. This provided a comparison between the moving load shear and moment capacities (Specimens C11T22-B3-ML and C11T22-B4-ML) and the monotonic shear and moment capacity (Specimen C11IT16-B1-ML) of equivalently designed specimens. The load was increased in 220 kN (50 kip) increments as shown in Figure 5.27 until failure of the specimen was achieved.

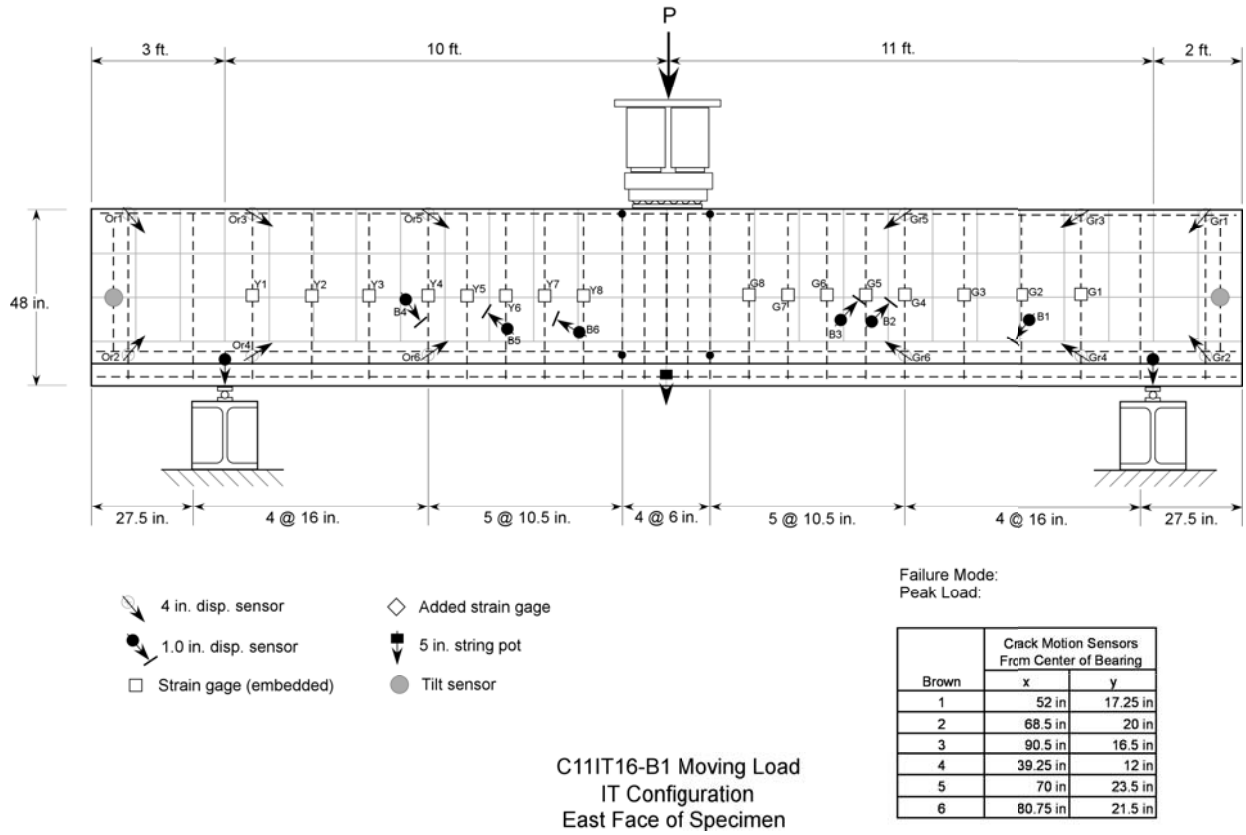

Brown	Crack Motion Sensors From Center of Bearing x	y
1	52 in	17.25 in
2	68.5 in	20 in
3	90.5 in	16.5 in
4	39.25 in	12 in
5	70 in	23.5 in
6	80.75 in	21.5 in

Figure 5.26: Support, loading conditions and instrumentation for Specimen C11IT16-B1-ML

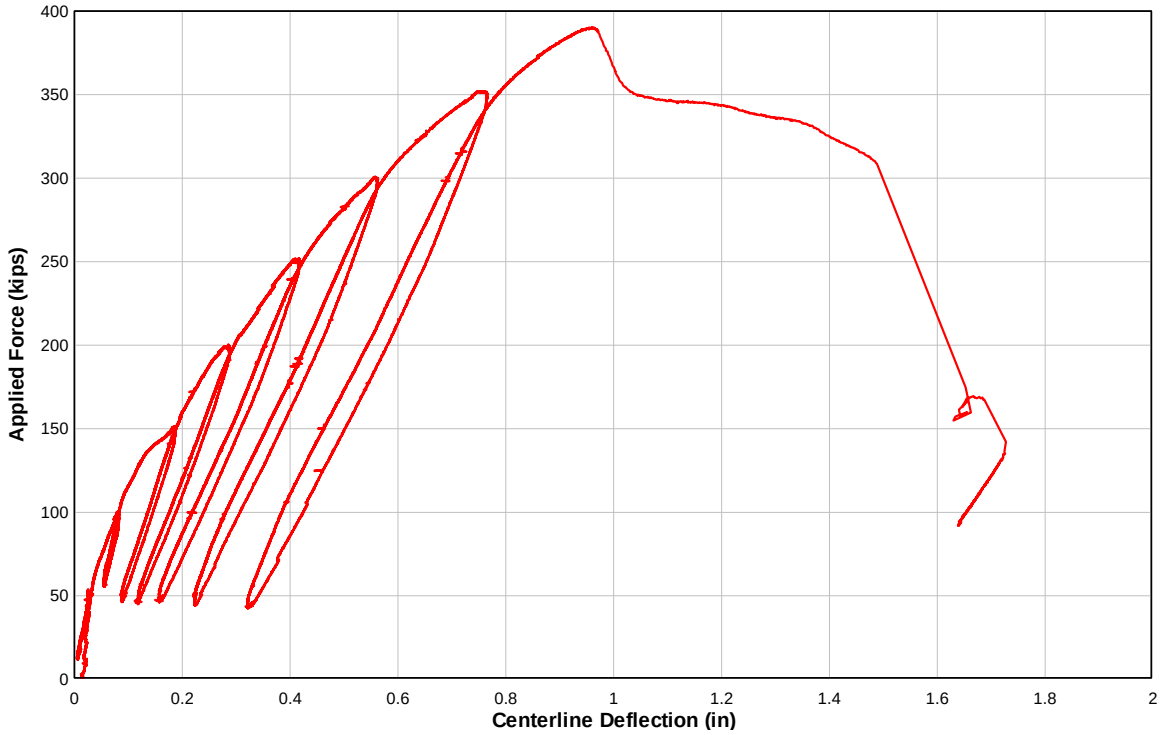

Figure 5.27: Loading and centerline deflection history for Specimen C11IT16-B1-ML.

5.7 INSTRUMENTATION

Specimens were instrumented to measure external deformations and internal stirrup strains. The instrument locations for each specimen are shown schematically in Figures 5.4, 5.10, 5.16, 5.21 and 5.26. Strain gages were installed at the mid-height of stirrups located in the test spans prior to the casting of each specimen. After initial diagonal cracks developed during testing, small excavations were made in the concrete to expose the outer face of stirrups that crossed cracks of significant width. A strain gage was installed at each of these locations to measure stirrup strain at the point where the stirrup crossed the crack (Figure 5.28). Transverse crack motion was measured with 25 mm (1 in) displacement sensors installed across the diagonal crack on the face of the concrete stem. Displacement transducers were installed diagonally across each set of equally spaced stirrups (Figure 5.29) to measure the diagonal deformations within the stirrup spacing. Support settlements were measured using 13 mm (0.5 in) displacement sensors.

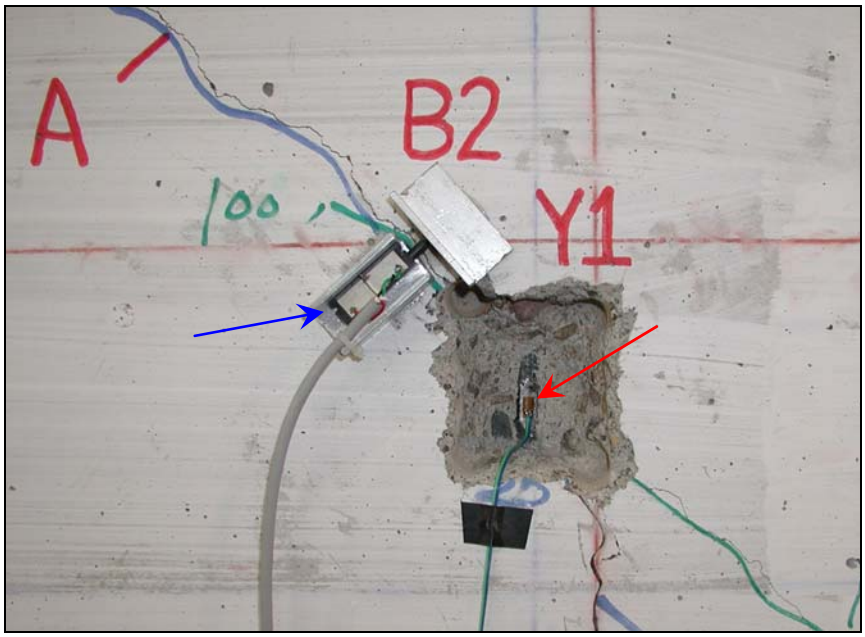

Figure 5.28: Exposed strain gage (red arrow) and 1 inch extensometer (blue arrow) located at a crack of interest.

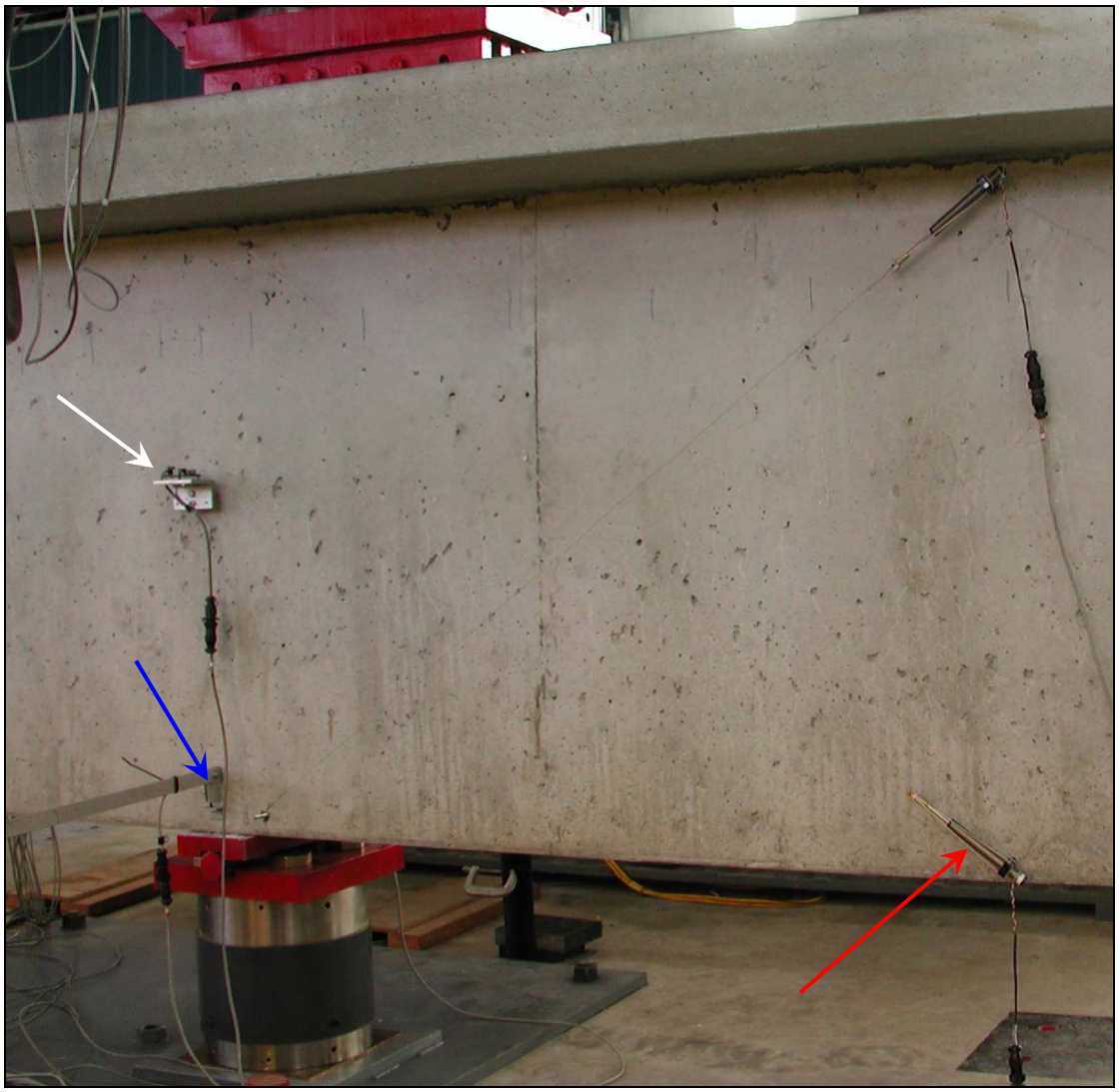

Figure 5.29: Instrumentation of a cantilevered specimen. Displacement transducers (red arrow) measure the diagonal deformations within groups of stirrups with equal spacing. Displacement sensors (blue arrow) were also used to measure support deflections. Specimen rotations were measured using tilt meters (white arrow)

The vertical deflection of cantilevered specimens was measured at the cantilever tip and at the dead end of the specimen. Rotation of the cantilevered specimens was measured at the centerline support and at the cantilever tip. Vertical deflection of the simply supported specimens was measured at the centerline of the specimen. Note that the span lengths of the simply supported beams were not equal. Therefore, the centerlines of the simply supported specimens do not coincide with the midpoint of the simple supports. Rotation of the simply supported specimens was measured at both ends.

6.0 TEST RESULTS AND DISCUSSION

6.1 CRACK PATTERNS

Significant differences in crack patterns were observed in the moving load specimens compared to the monotonically loaded control specimen. The crack pattern for Specimen C11IT16-B1-ML is shown in Figure 6.1, which was consistent with crack patterns observed in other monotonic tests. In the monotonic specimen, the diagonal cracks tended to radiate outward from the stationary point of loading, resulting in more clearly defined compression struts within the concrete matrix. In the moving load specimens, the shear-moment ratio and internal stress field were continually changing at a given section. Referring to Figures 6.2 and 6.3, diagonal cracks in the moving load specimens tended to be more vertically oriented, and cracks and compression struts tended to cross over one another more than in the control specimen. More spider web cracking was observed in the moving load specimens at high load steps compared to the control specimen. The similarity of cracking patterns in a cantilevered moving load specimen and a typical CRC continuous bridge girder are illustrated in Figure 6.4. The similarity in crack patterns between the moving load specimens and existing bridges indicates that the stress fields present in the Springfield Bridge may be better represented by the application of moving loads rather than stationary loads.

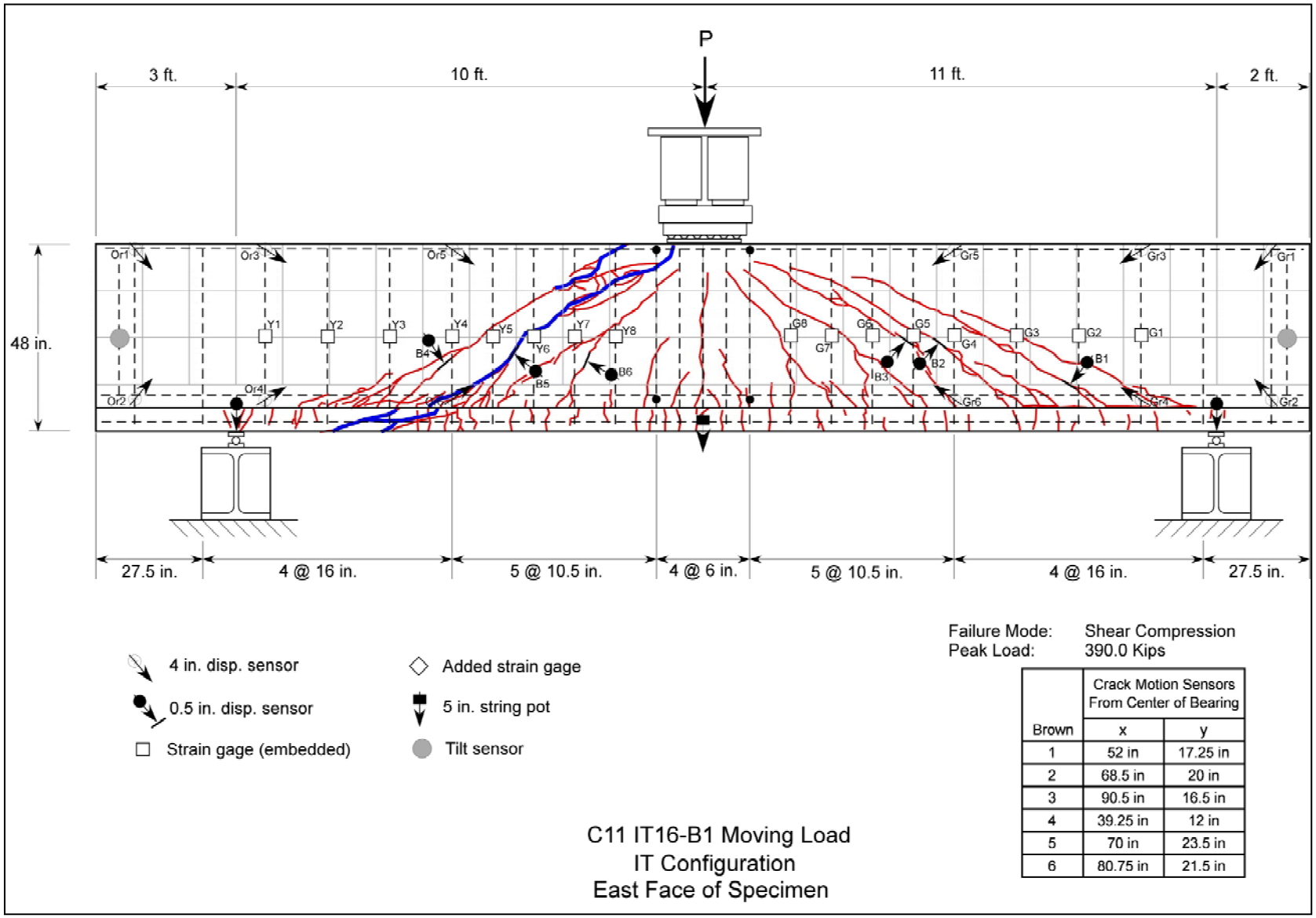

Brown	Crack Motion Sensors From Center of Bearing	
	x	y
1	52 in	17.25 in
2	68.5 in	20 in
3	90.5 in	16.5 in
4	39.25 in	12 in
5	70 in	23.5 in
6	80.75 in	21.5 in

Figure 6.1: Support and loading conditions, instrumentation and crack map for Specimen C11IT16-B1-ML. Bold blue line denotes failure crack

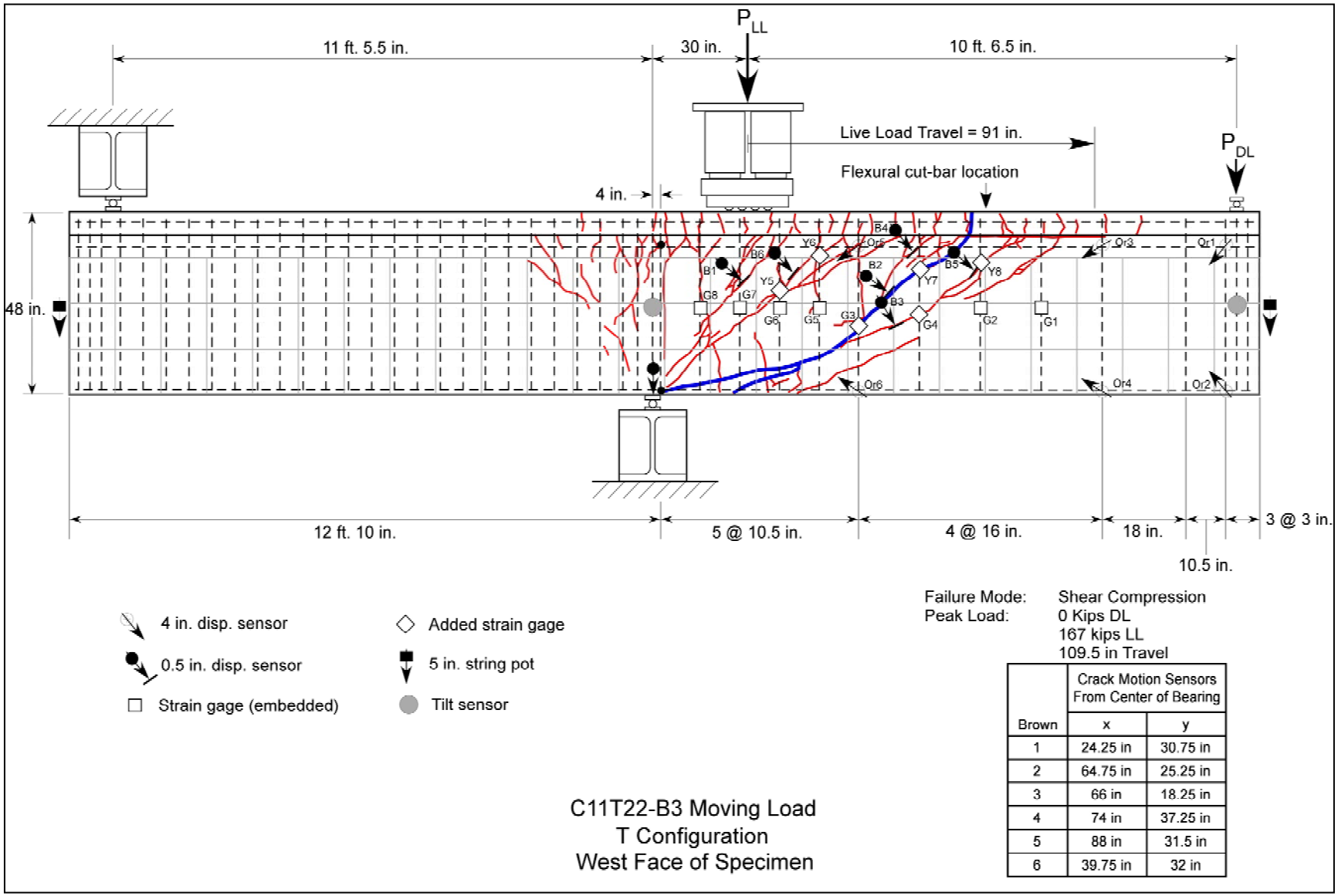

Brown	Crack Motion Sensors From Center of Bearing	
	x	y
1	24.25 in	30.75 in
2	64.75 in	25.25 in
3	66 in	18.25 in
4	74 in	37.25 in
5	88 in	31.5 in
6	39.75 in	32 in

Figure 6.2: Support and loading conditions, instrumentation and crack map for Specimen C11T22-B3-ML. Bold blue line denotes failure crack.

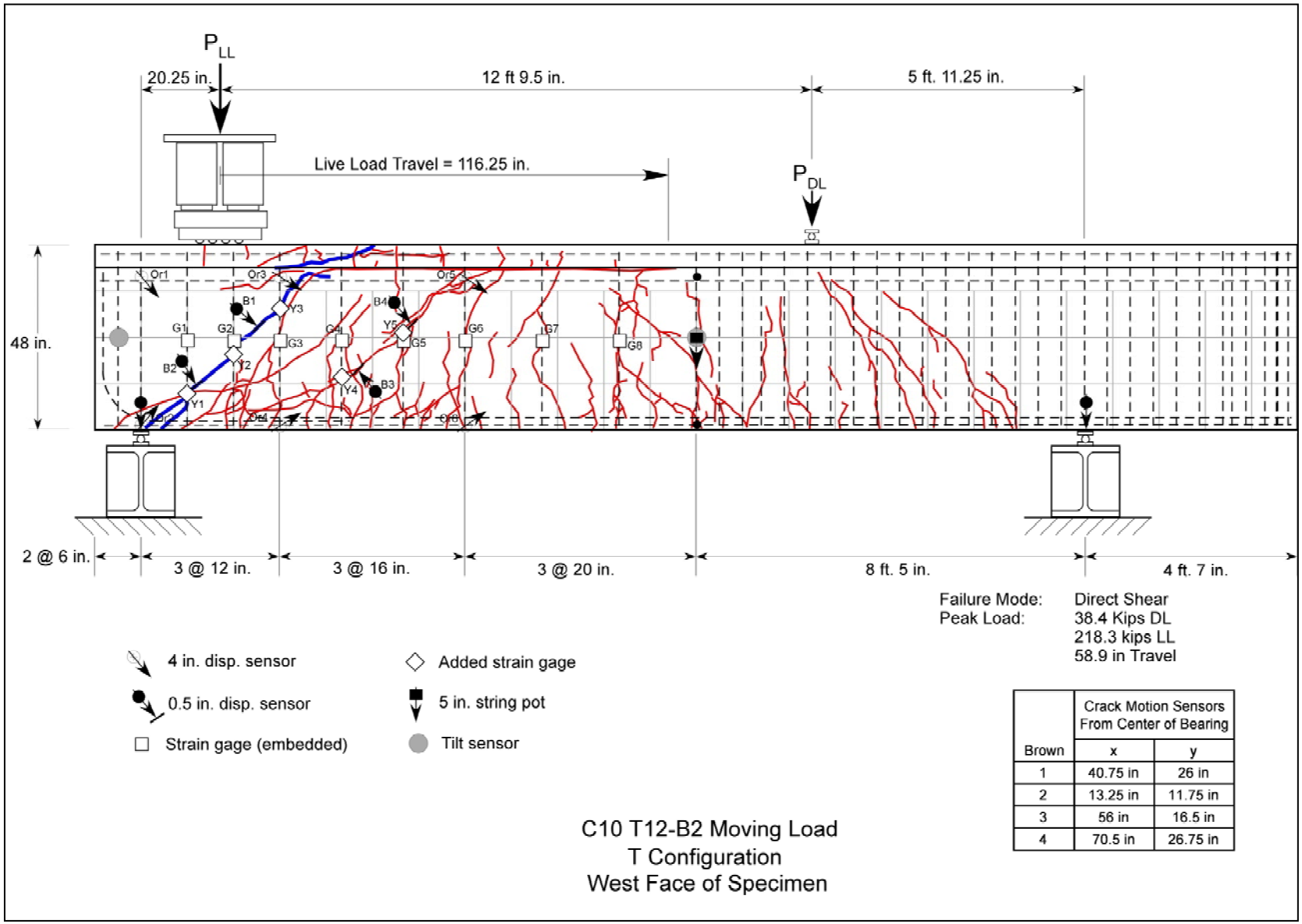

Brown	Crack Motion Sensors From Center of Bearing	
	x	y
1	40.75 in	26 in
2	13.25 in	11.75 in
3	56 in	16.5 in
4	70.5 in	26.75 in

Figure 6.3: Support and loading conditions, instrumentation and crack map for Specimen C10T12-B2-ML. Bold blue line denotes failure crack.

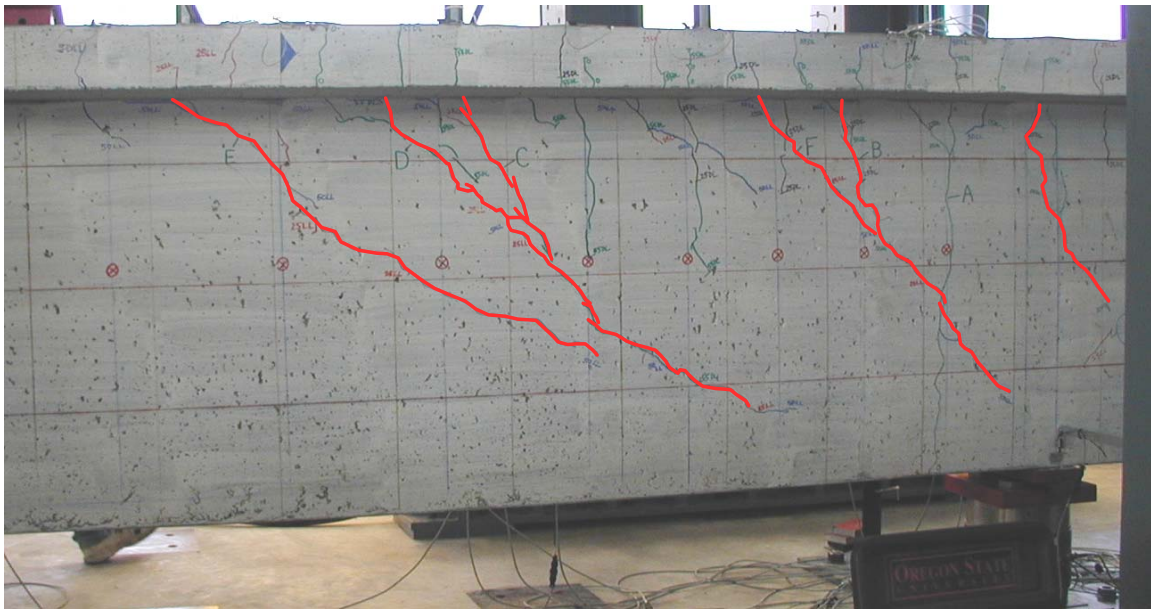

(a)

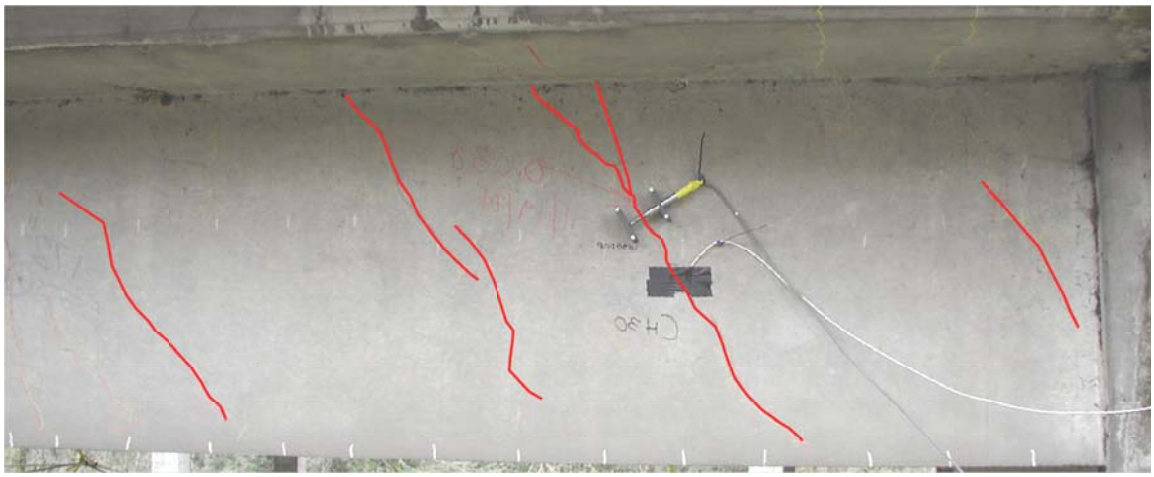

(b)

Figure 6.4: Similarity of cracking patterns in (a) Specimen C11T22-B3-ML and (b) a typical continuous bridge girder (Spores Bridge, Eugene, Oregon), with red lines denoting primary diagonal cracks.

6.2 PREDICTED MOVING LOAD SHEAR-MOMENT CAPACITY

A qualitative analysis of the moving load shear-moment capacities for each specimen was performed by comparing the imposed live and dead load shear-moment histories to the shear-moment capacity envelopes predicted by MCFT and Response 2000™. The effect of reduced flexural steel sections resulting from straight bar development within the specimens was incorporated into the MCFT and Response 2000™ calculations.

In general, the MCFT envelope was more conservative and fell within the Response 2000™ envelope. The shear capacity of each specimen was also estimated using ACI 318-02. In this study, each test span was divided into a series of vertical cut sections spaced 305 mm (12 in) apart beginning at the centerline of the support. The induced shear-moment interactions, shear-moment envelopes and ACI 318-02 shear capacities were plotted for each section. Since diagonal cracks cross more than one section, it can be reasonably assumed that failure prediction will involve an interaction of the shear-moment capacities of several sections. The results of the qualitative analysis are provided in the following sections.

6.2.1 C11T22-B3-ML

This specimen failed in shear-compression at an imposed live load of 743 kN (167 kips) located 2.78 m (9.13 ft) from the cantilever face of support. The concrete crack pattern and failure conditions are shown in Figure 6.2. The imposed shear-moment histories, shear-moment envelopes and ACI 318-02 predicted shear capacity at each section are shown in Figures 6.5 through 6.13. The diagonal crack at failure extended from the face of support to a point approximately 1.83 m (6 ft) from the face of support. Figures 6.5 through 6.13 show that the induced shear-moment interaction at failure exceeded the Response 2000™ envelope from the face of support thru 0.91 m (3 ft). The induced shear fell between the Response 2000™ and MCFT envelopes from 1.22 m thru 1.83 m (4 ft thru 6 ft). It is noted that Response 2000™ reasonably predicted the shear-moment capacity at each section, except in the stress-disturbed region (from the face of support to an effective depth (1.15 m (3.8 ft)), where the induced shear-moment significantly exceeded the Response 2000™ envelope. This is to be expected for sectional analysis methods applied to disturbed regions. MCFT conservatively estimated the shear-moment capacity at all sections. ACI 318-02 greatly underestimated the shear capacity at all sections.

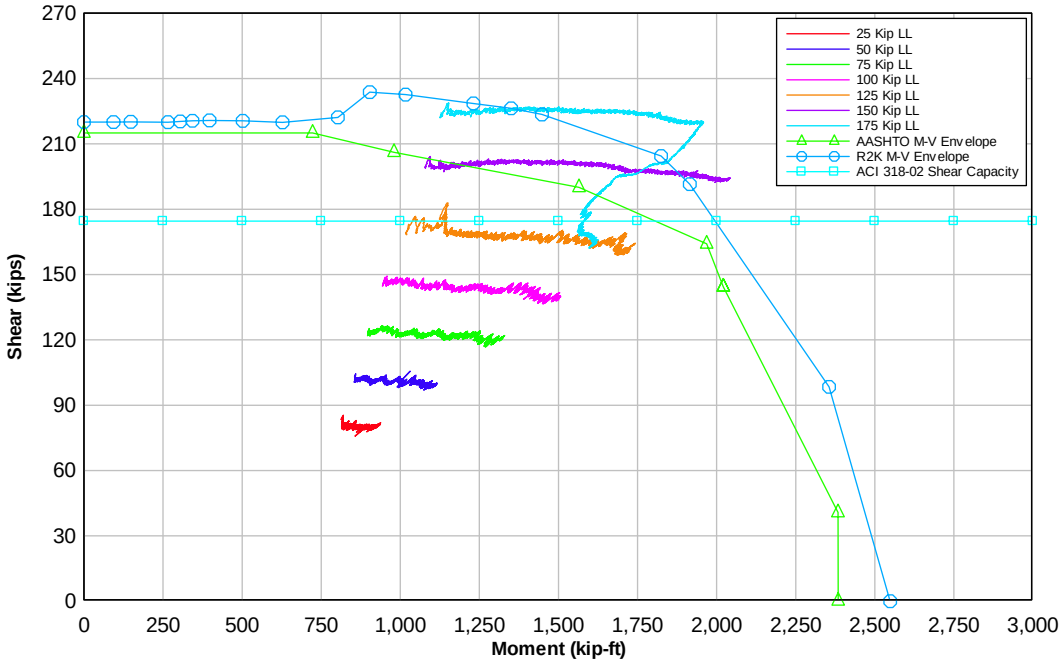

Figure 6.5: Shear-moment interaction diagram for Specimen C11T22-B3-ML for cut section located at face of support.

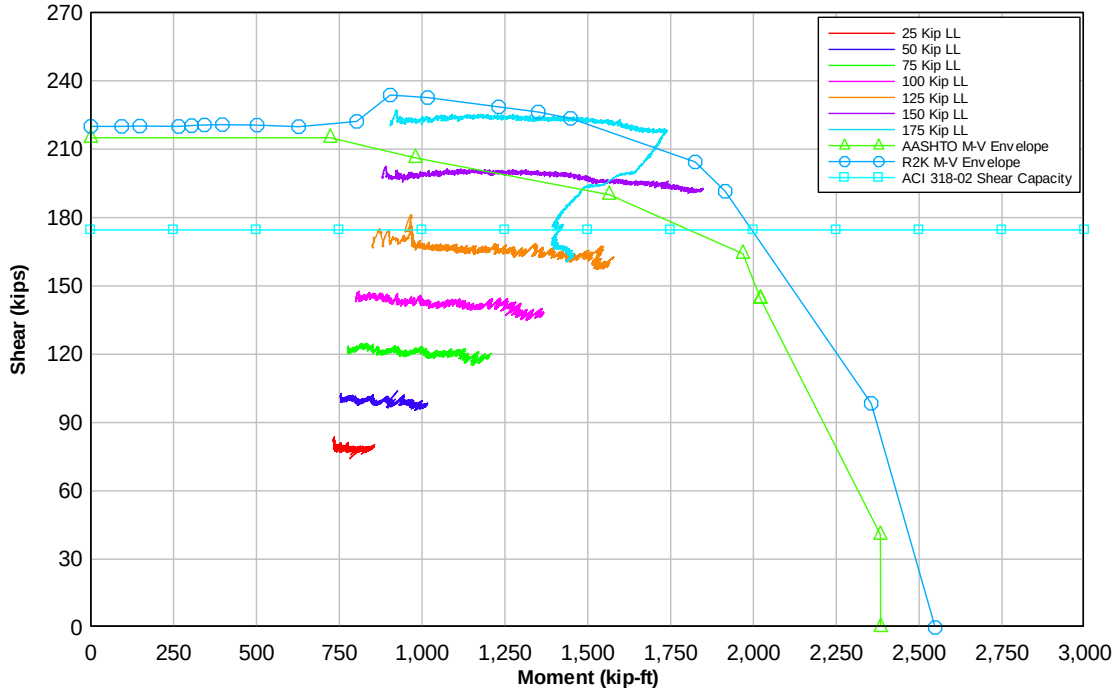

Figure 6.6: Shear-moment interaction diagram for Specimen C11T22-B3-ML for cut section located 1 foot from face of support.

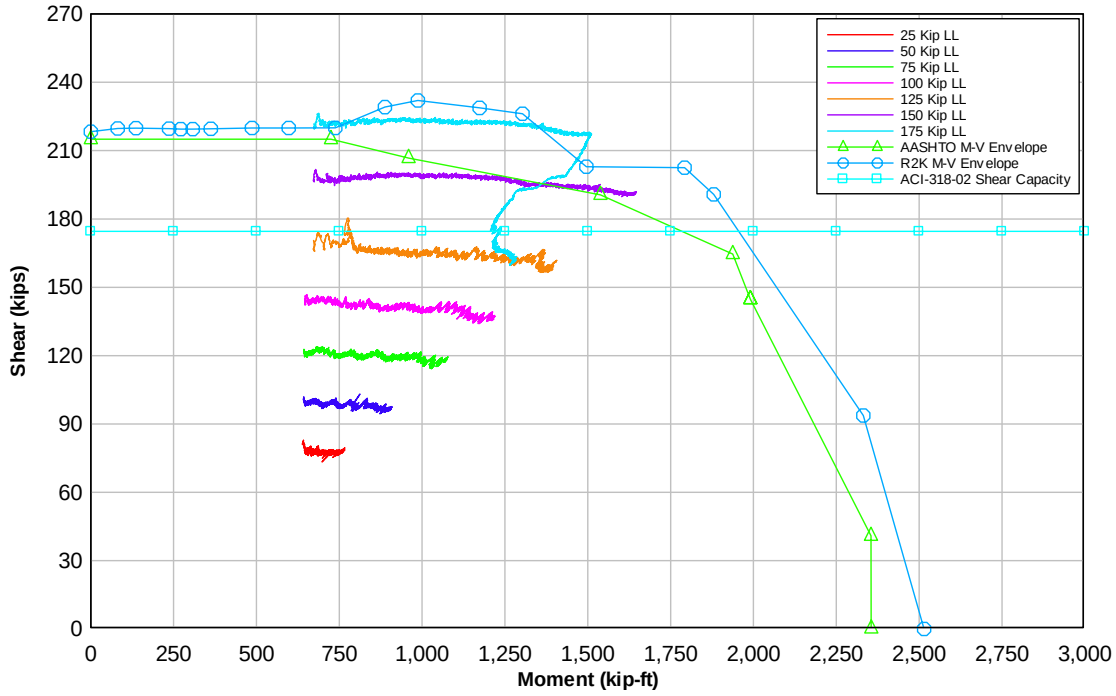

Figure 6.7: Shear-moment interaction diagram for Specimen C11T22-B3-ML for cut section located 2 feet from face of support.

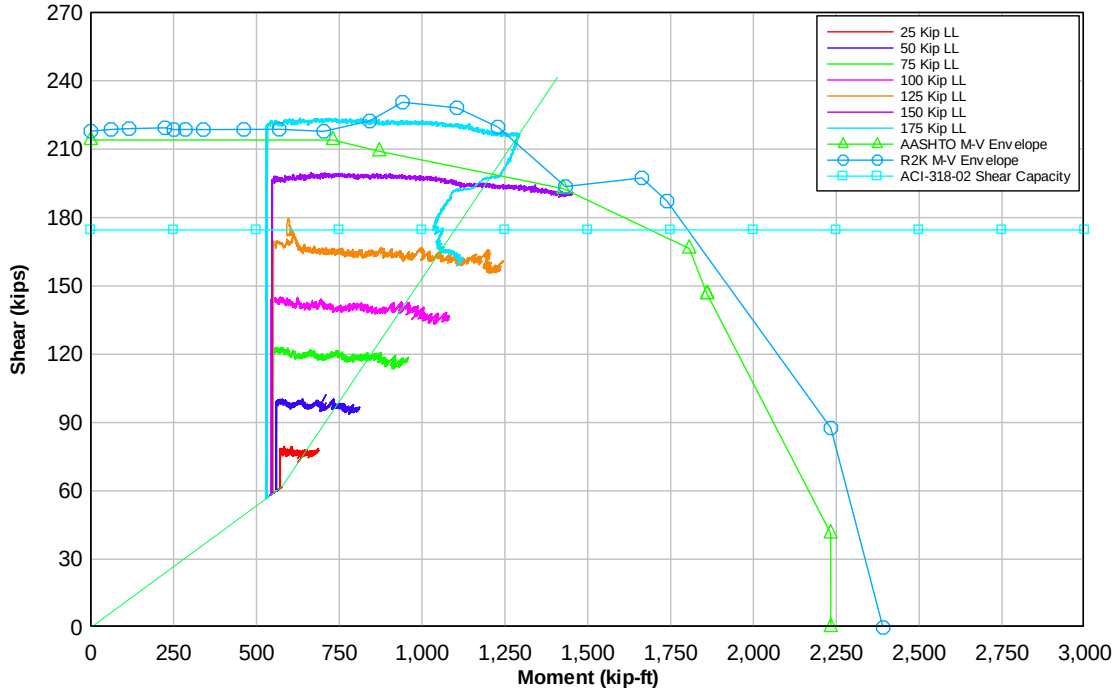

Figure 6.8: Shear-moment interaction diagram for Specimen C11T22-B3-ML for cut section located 3 feet from face of support.

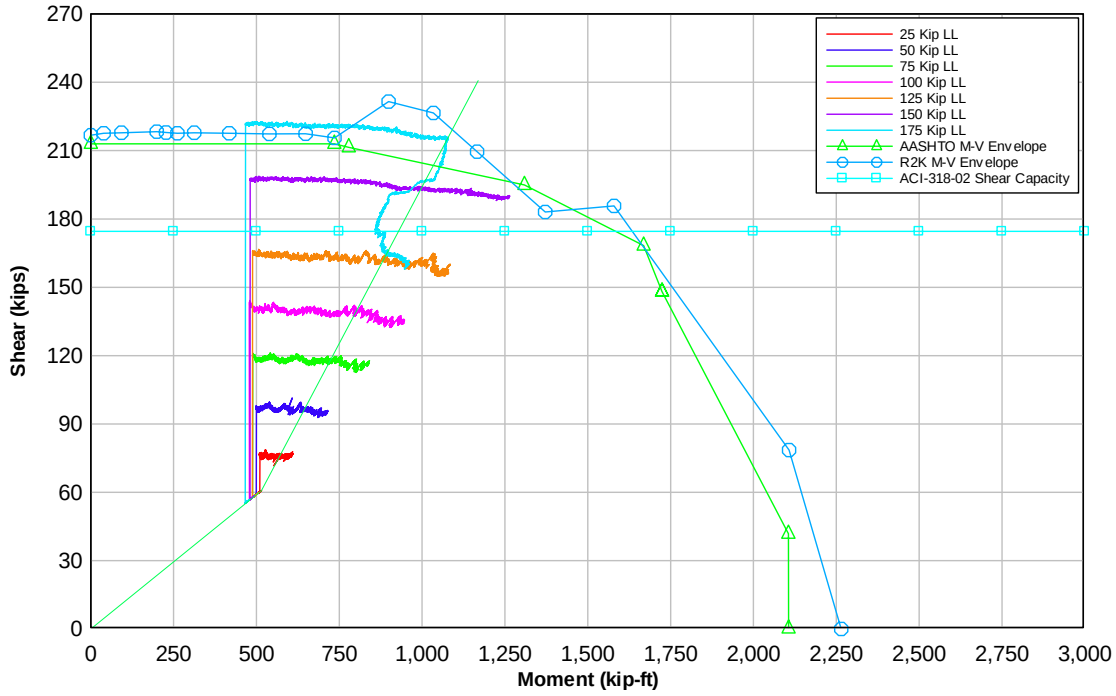

Figure 6.9: Shear-moment interaction diagram for Specimen C11T22-B3-ML for cut section located 4 feet from face of support.

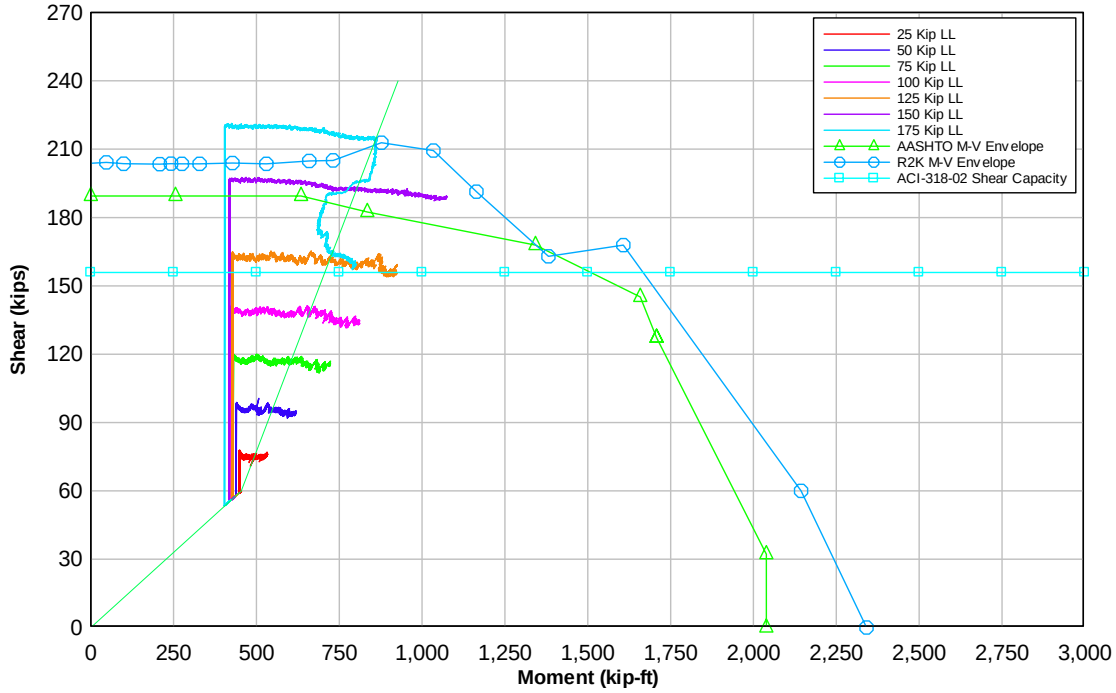

Figure 6.10: Shear-moment interaction diagram for Specimen C11T22-B3-ML for cut section located 5 feet from face of support.

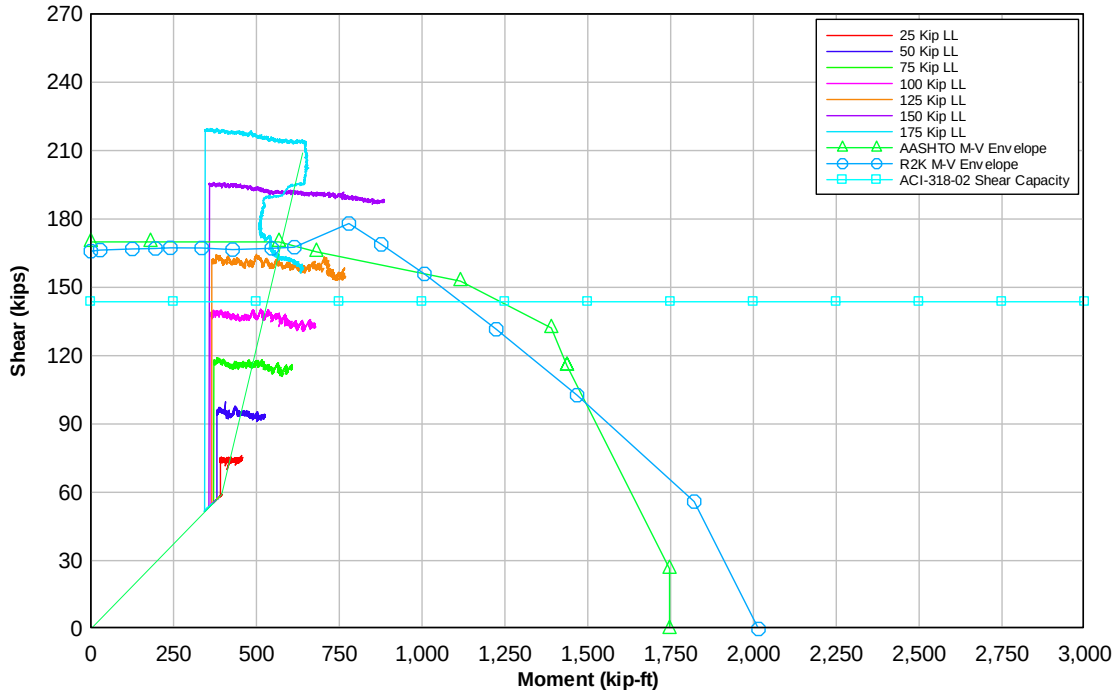

Figure 6.11: Shear-moment interaction diagram for Specimen C11T22-B3-ML for cut section located 6 feet from face of support.

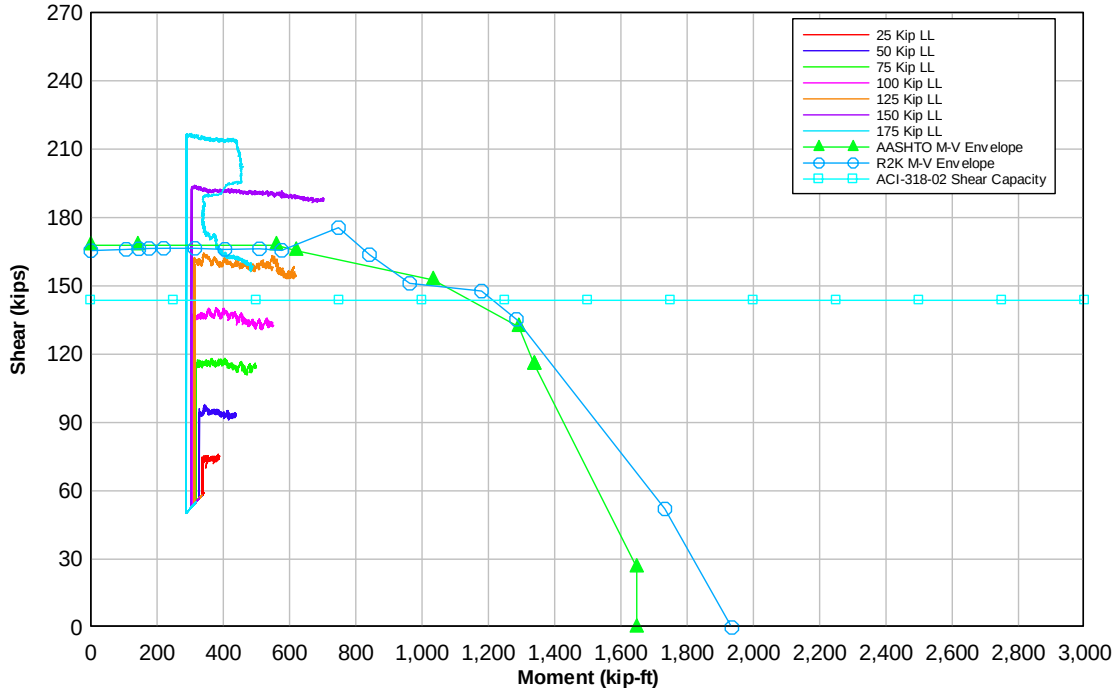

Figure 6.12: Shear-moment interaction diagram for Specimen C11T22-B3-ML for cut section located 7 feet from face of support.

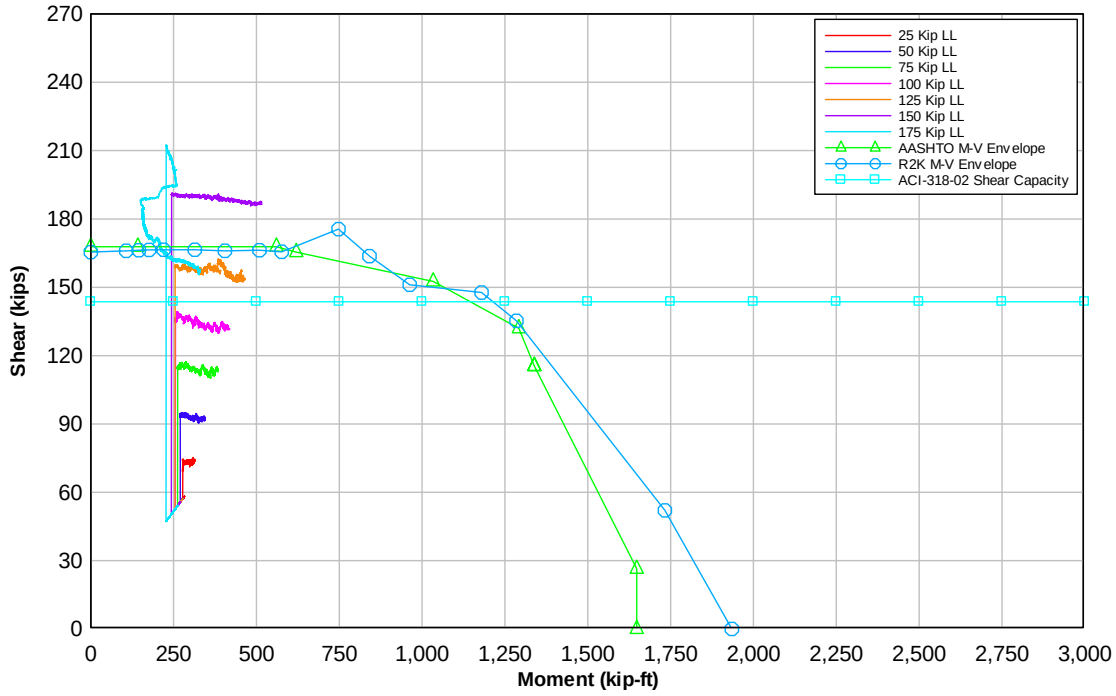

Figure 6.13: Shear-moment interaction diagram for Specimen C11T22-B3-ML for cut section located 8 feet from face of support.

It is significant to note the specimen performance in regions that did not fail. Traveling away from the face of support, the sectional shear-moment capacities decrease due to increased stirrup spacing and reduced flexural steel development. The imposed shear began to dominate the imposed moment at approximately 2.13 m (7 ft) from the face of support. In this high-shear, low-moment region of the beam, the imposed shear-moment at failure greatly exceeded both the Response 2000™ and MCFT envelopes.

6.2.2 C11T22-B4-ML

This specimen failed in shear at an imposed live load of 734 kN (165 kips) located 2.82 m (9.25 ft) from the cantilever face of support. The concrete crack pattern and failure conditions are shown in Figure 6.14. The imposed shear-moment histories, shear-moment envelopes and ACI 318-02 predicted shear capacity at each section are shown in Figures 6.15 through 6.24. The failure crack extended from the face of support to a point approximately 1.52 m (5 ft) away from the face of support.

Figures 6.15 through 6.24 show that the shear-moment interaction at failure coincided very closely with the Response 2000™ shear-moment envelope at the face of support. The ultimate shear-moment interaction values fell between the Response 2000™ and MCFT envelopes within the 0.30 m to 0.91 m (1 ft to 3 ft) range. At 1.22 m (4 ft), the ultimate shear-moment interaction fell below the MCFT envelope. At 1.52 m (5 ft), the ultimate shear-moment interaction values again fell between the Response 2000™ and MCFT envelopes. At all of these sections the area bounded by the Response 2000™ and MCFT envelopes provided a reasonable estimate of the specimen capacity. Again, the MCFT envelope provided a conservative estimate of the specimen shear-moment capacity and ACI 318-02 greatly underestimated the specimen shear capacity at all sections.

The imposed shear began to dominate the imposed moment at about 1.83 m (6 ft). As with Specimen C11T22-B3-ML, the shear-moment at failure greatly exceeded the Response 2000™ and MCFT envelopes near the end of the cantilever as expected in regions of high shear-moment ratio.

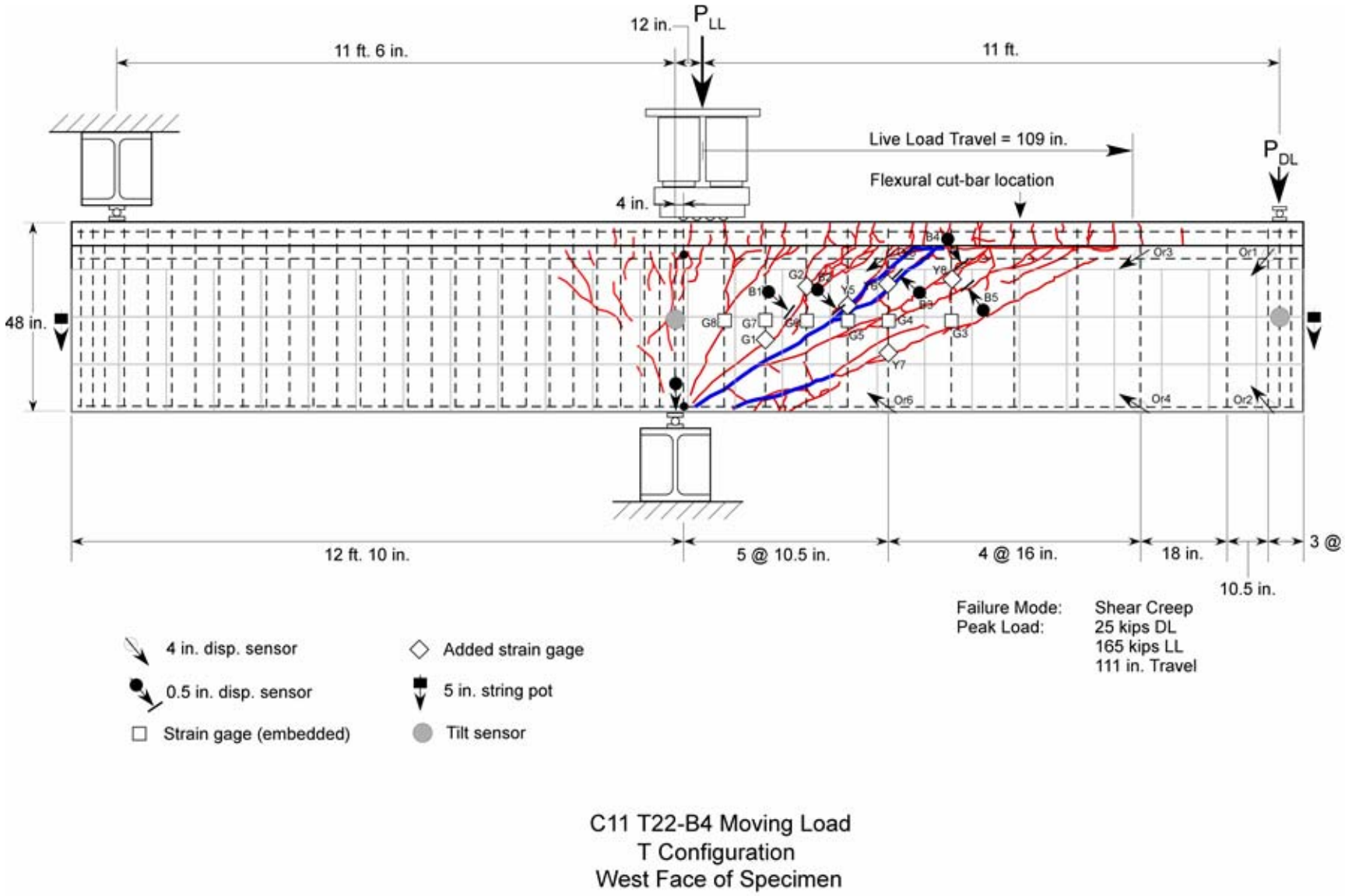

Figure 6.14: Support and loading conditions, instrumentation and crack map for Specimen C11T22-B4-ML. Bold blue line denotes failure crack.

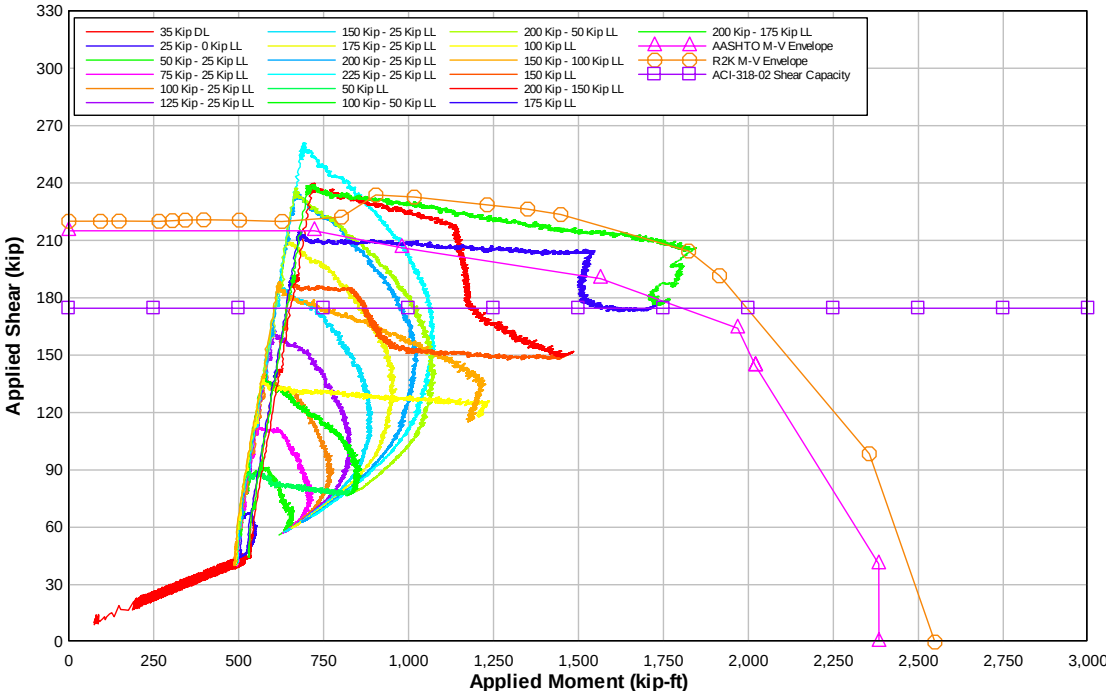

Figure 6.15: Shear-moment interaction diagram for Specimen C11T22-B4-ML for cut section located at face of support.

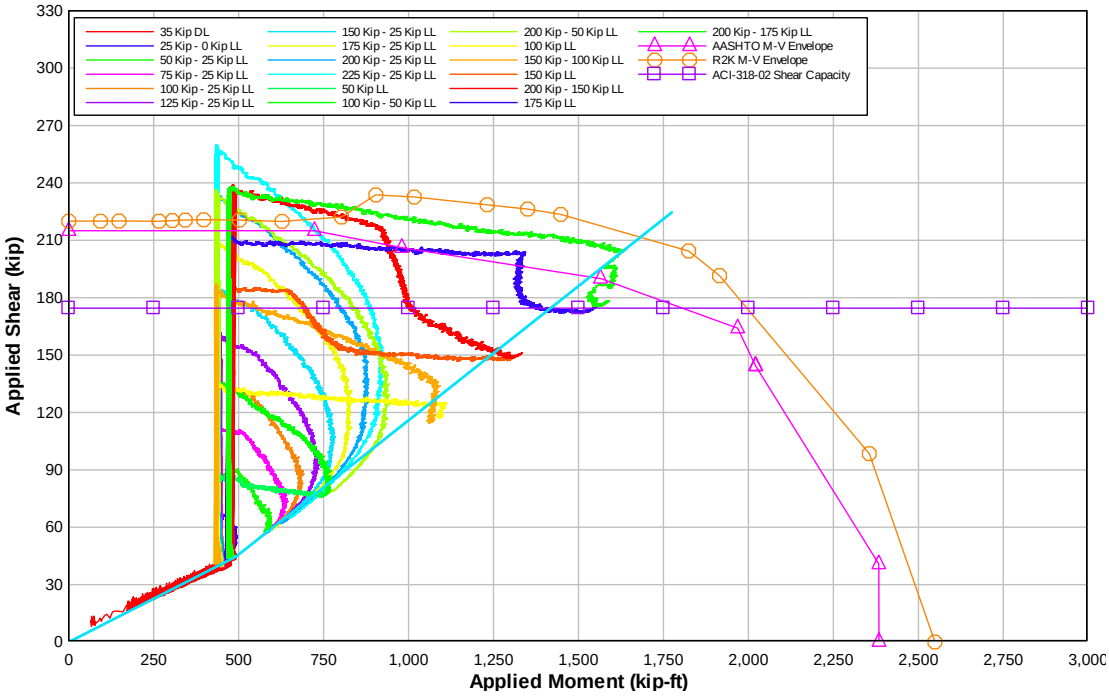

Figure 6.16: Shear-moment interaction diagram for Specimen C11T22-B4-ML for cut section located 1 foot from face of support.

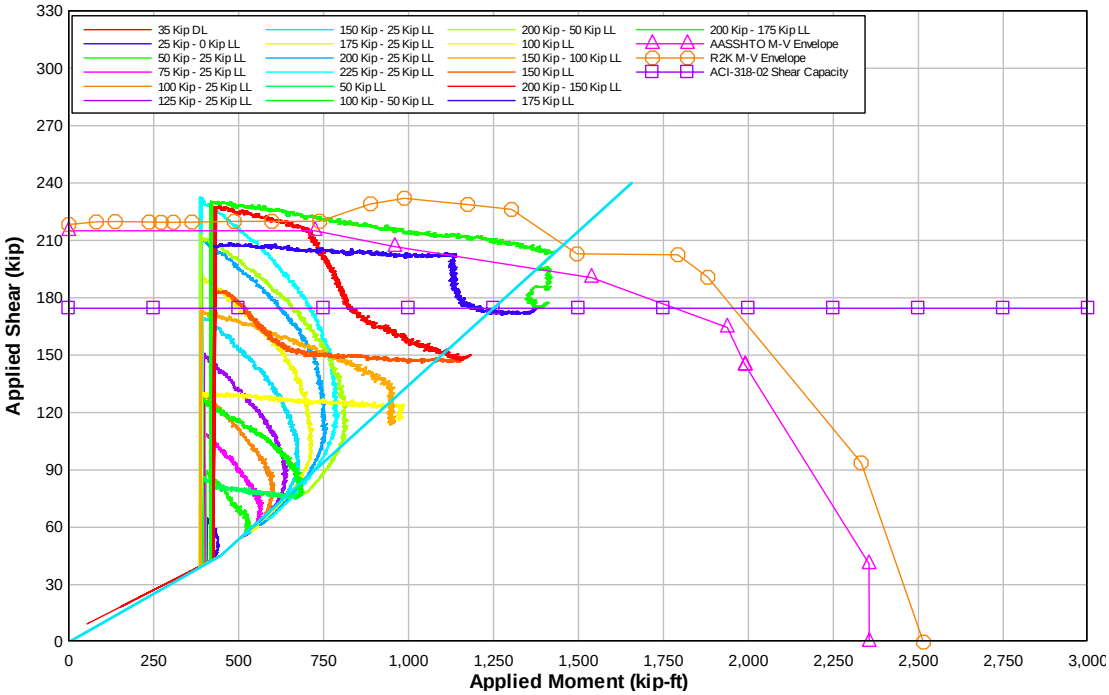

Figure 6.17: Shear-moment interaction diagram for Specimen C11T22-B4-ML for cut section located 2 feet from face of support.

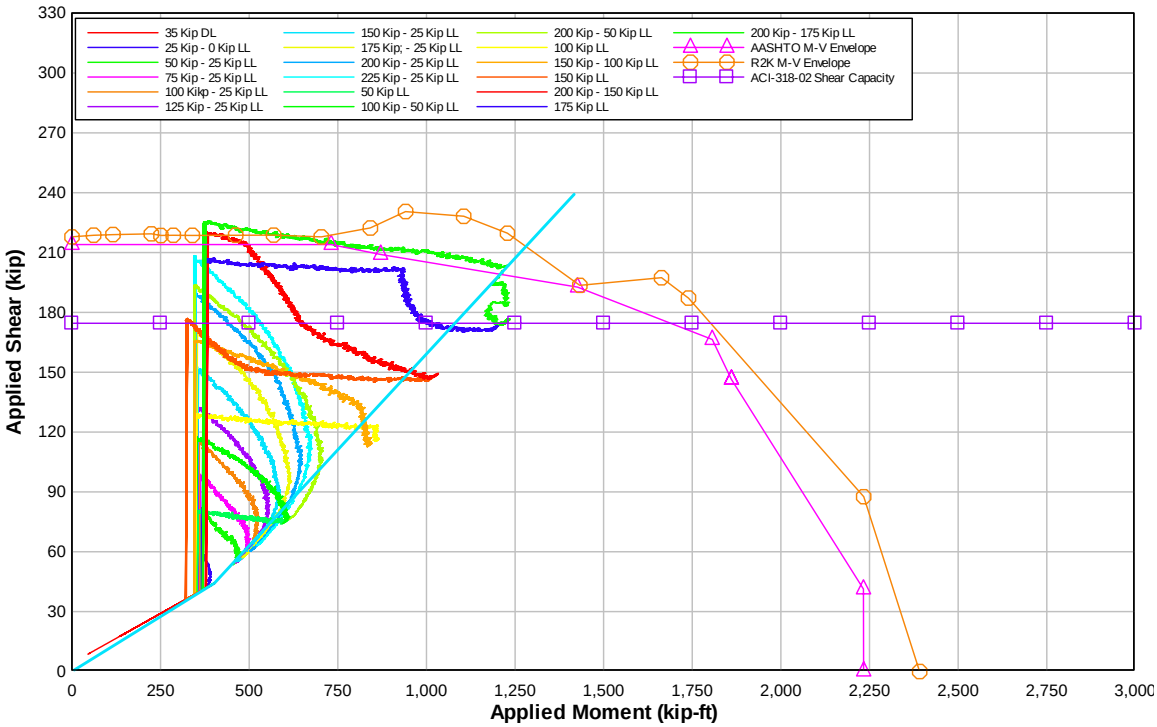

Figure 6.18: Shear-moment interaction diagram for Specimen C11T22-B4-ML for cut section located 3 feet from face of support.

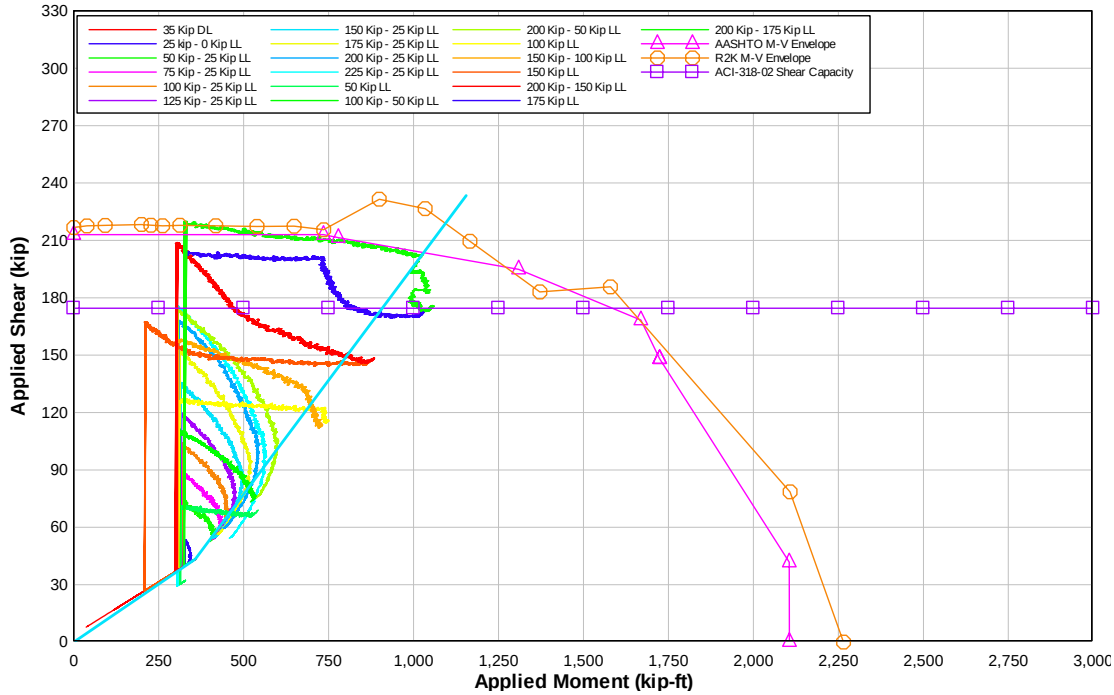

Figure 6.19 Shear-moment interaction diagram for Specimen C11T22-B4-ML for cut section located 4 feet from face of support.

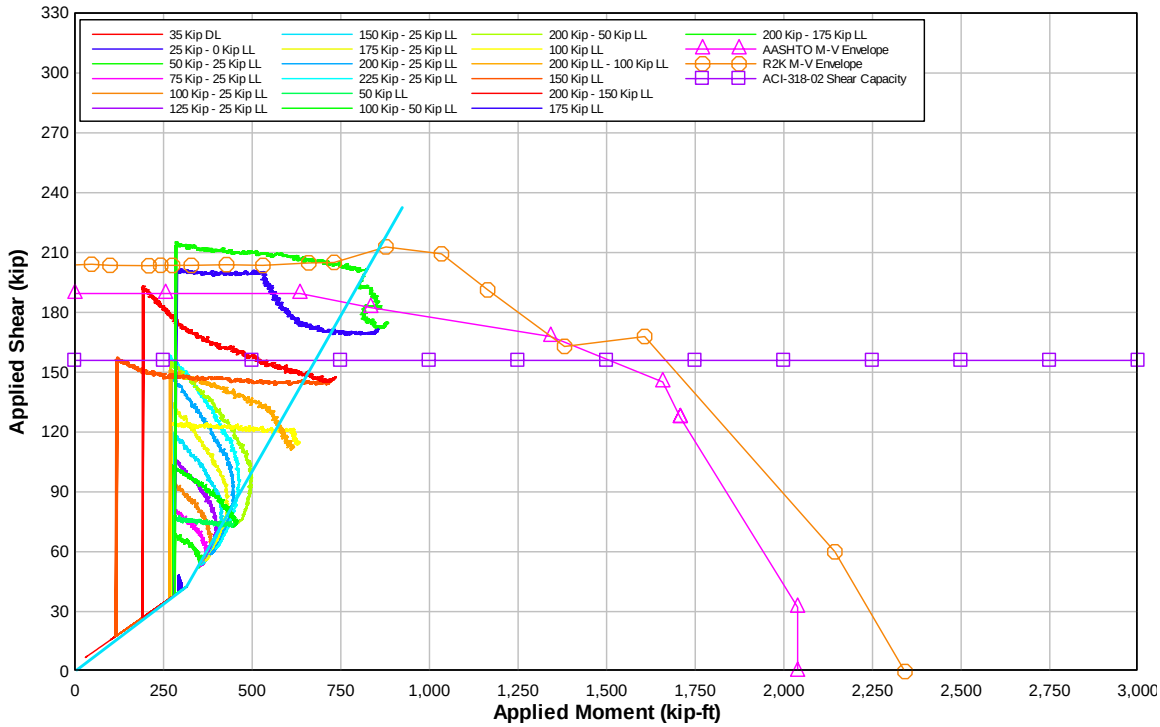

Figure 6.20: Shear-moment interaction diagram for Specimen C11T22-B4-ML for cut section located 5 feet from face of support.

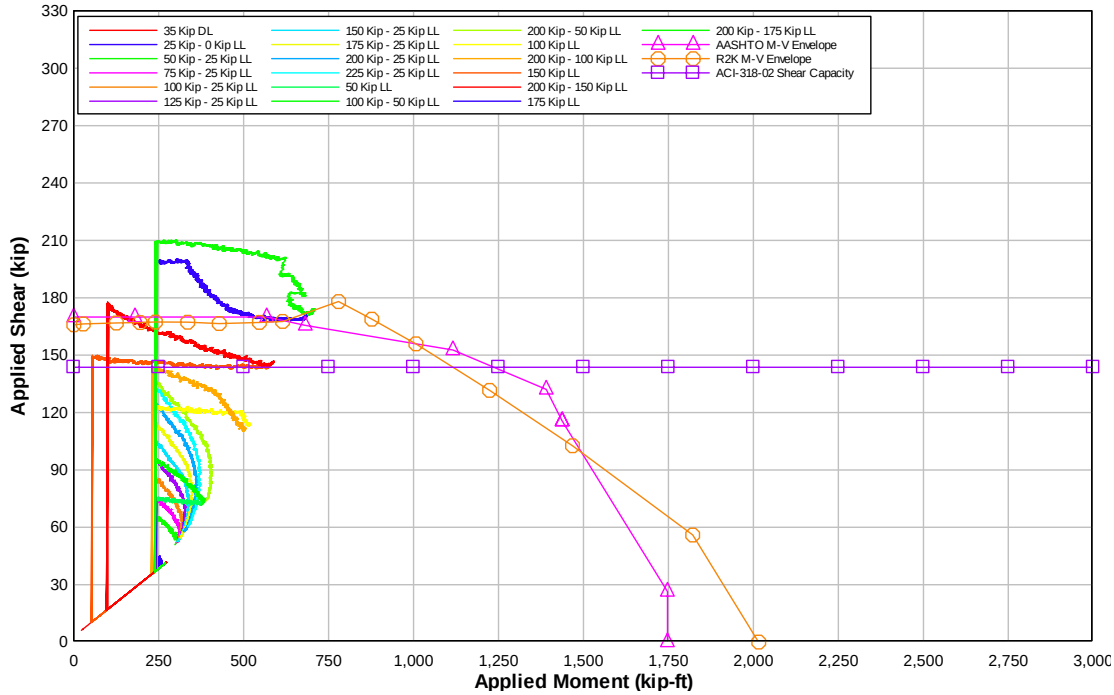

Figure 6.21: Shear-moment interaction diagram for Specimen C11T22-B4-ML for cut section located 6 feet from face of support.

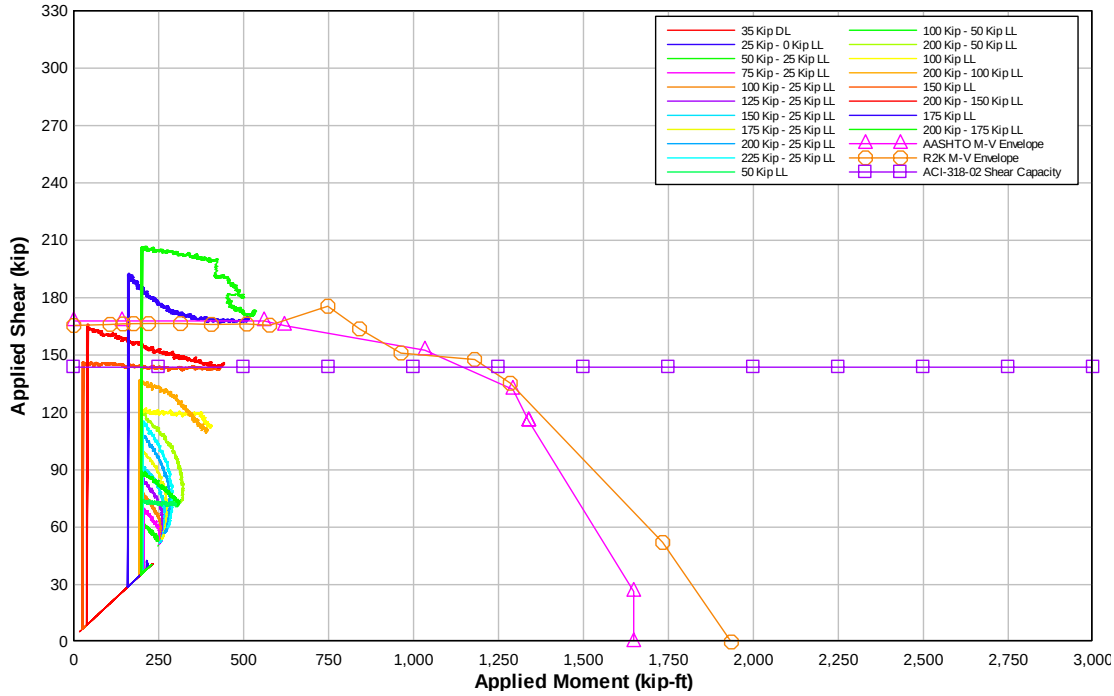

Figure 6.22: Shear-moment interaction diagram for Specimen C11T22-B4-ML for cut section located 7 feet from face of support.

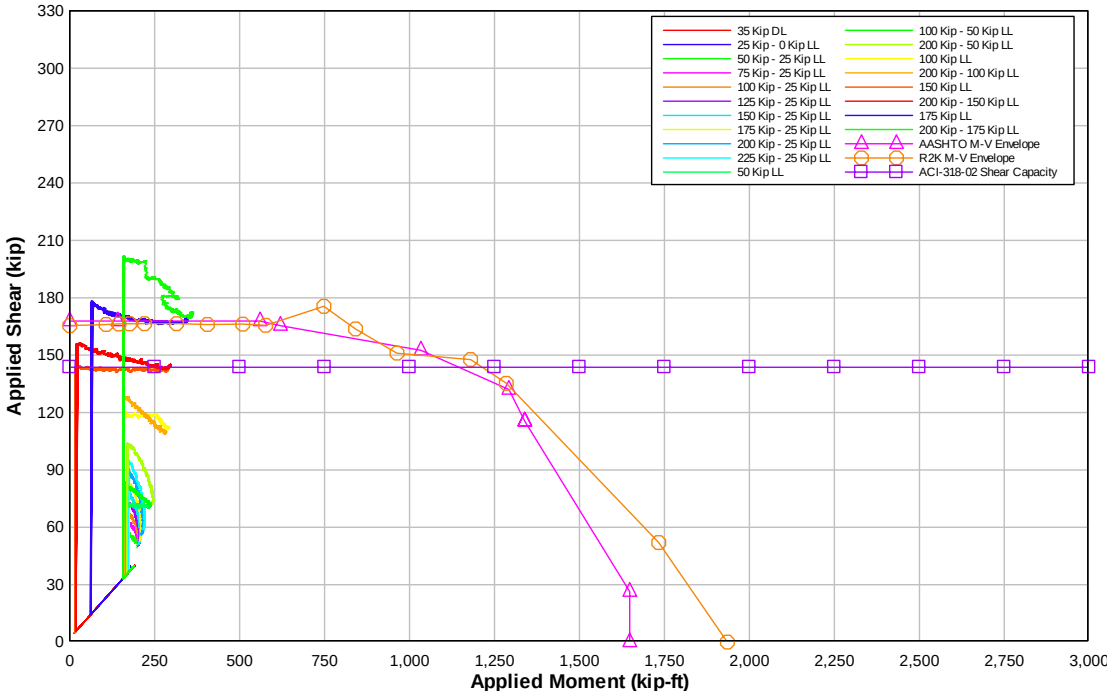

Figure 6.23: Shear-moment interaction diagram for Specimen C11T22-B4-ML for cut section located 8 feet from face of support.

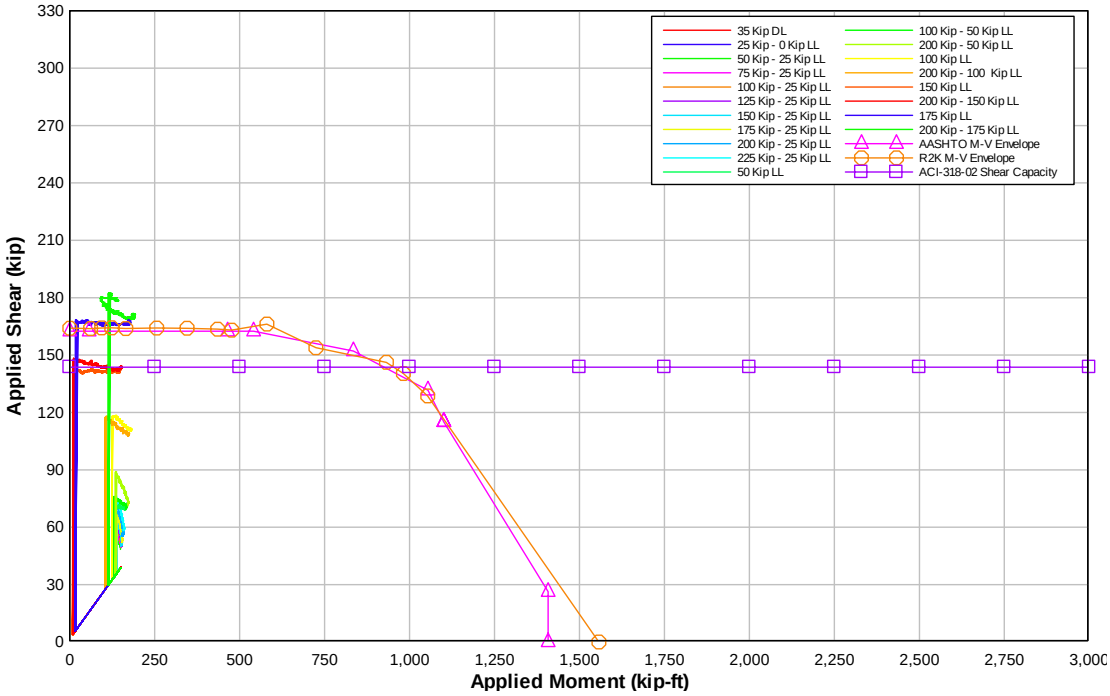

Figure 6.24: Shear-moment interaction diagram for Specimen C11T22-B4-ML for cut section located 9 feet from face of support.

6.2.3 C11T16.5-B2-ML

This specimen failed in shear-compression at an imposed live load of 109 kN (244 kips) located 1.91 m (6.25 ft) from the cantilever face of support. The concrete crack pattern and failure conditions are shown in Figure 6.25. The imposed shear-moment histories, shear-moment envelopes and ACI 318-02 predicted shear capacity at each section are shown in Figures 6.25 through 6.35. A diagonal failure crack extended from the face of support to a point approximately 1.22 m (4 ft) from the face of support. The shear-moment value at failure exceeded the Response 2000™ envelope at the face of support. The ultimate shear-moment value fell between the Response 2000™ and MCFT envelopes within the 0.30 m to 1.22 m (1 ft to 4 ft) range. *V*reasonably predicted the specimen shear-moment capacity at each section while MCFT provided a conservative estimate of shear-moment capacity. Beyond 1.22 m (4 ft), the induced shear-moment at failure greatly exceeded the Response 2000™ and MCFT envelopes as expected in regions of high shear-moment ratio. Again, ACI 318-02 greatly underestimated the specimen shear capacity at all sections.

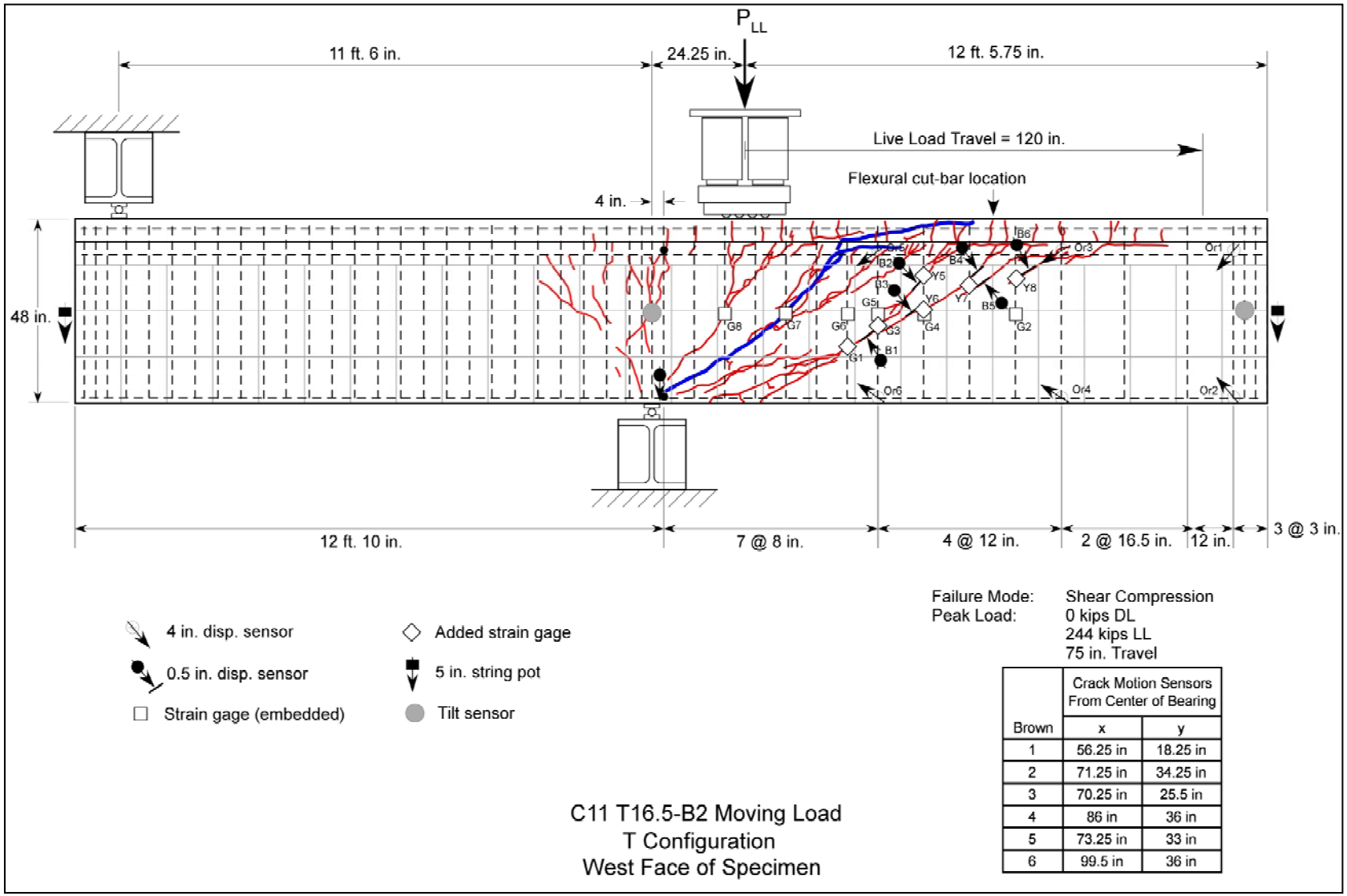

Brown	Crack Motion Sensors From Center of Bearing	
	x	y
1	56.25 in	18.25 in
2	71.25 in	34.25 in
3	70.25 in	25.5 in
4	86 in	36 in
5	73.25 in	33 in
6	99.5 in	36 in

Figure 6.25: Support and loading conditions, instrumentation and crack map for Specimen C11T16.5-B2-ML. Bold blue line denotes failure crack.

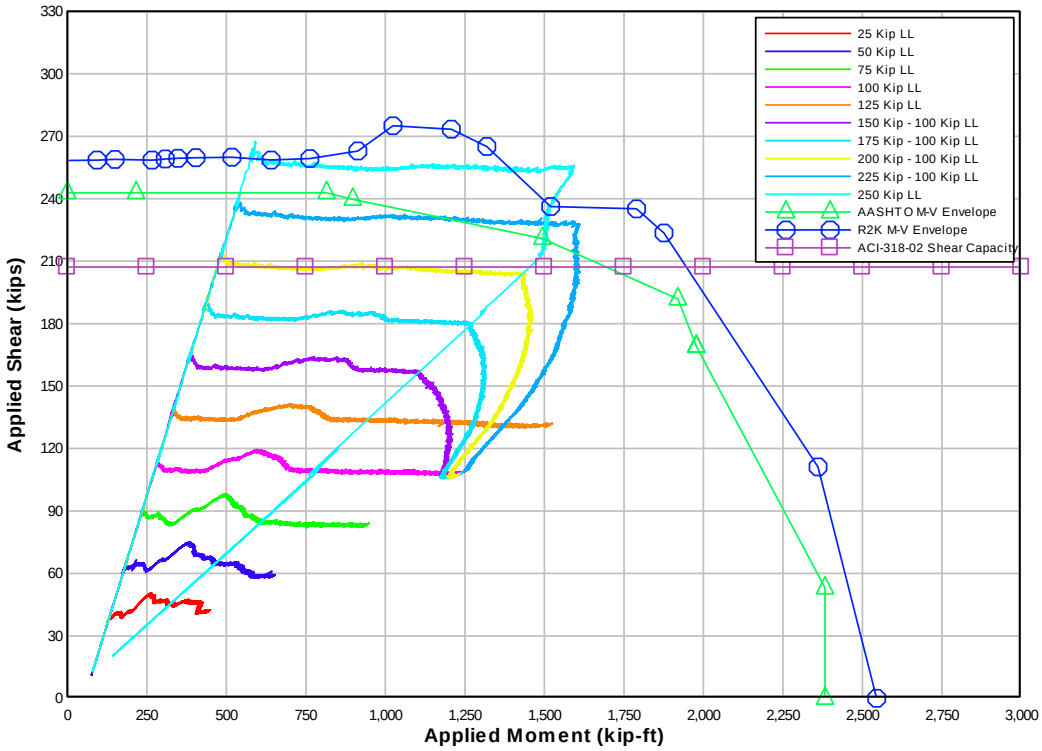

Figure 6.26: Shear-moment interaction diagram for Specimen C11T16.5-B2-ML at cut section located at face of support.

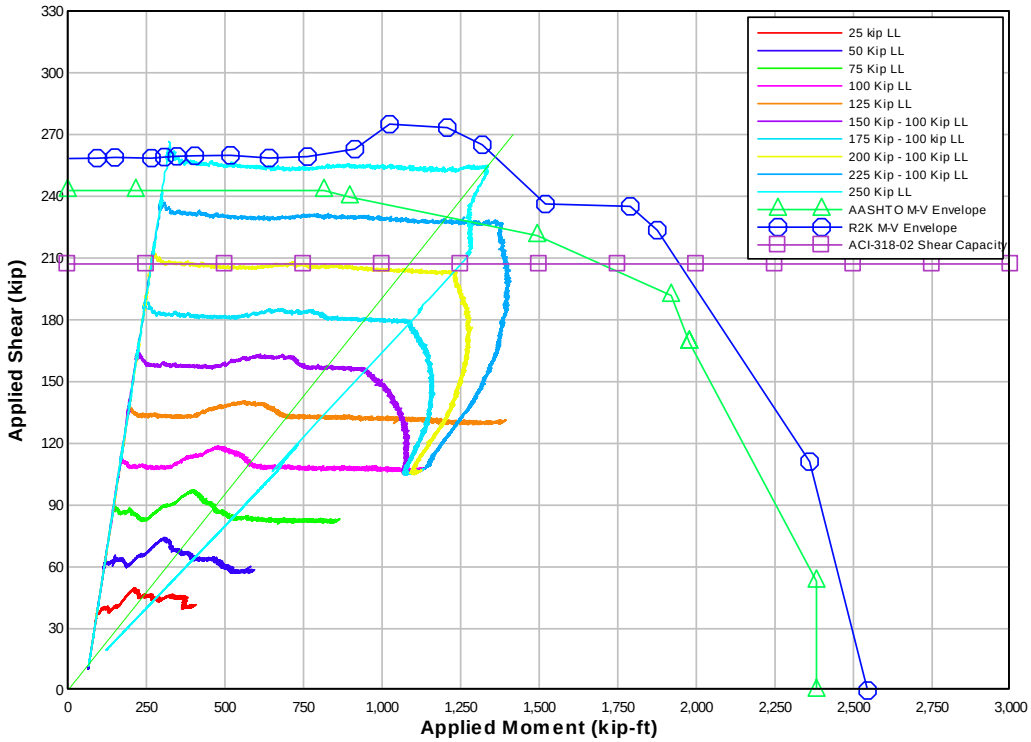

Figure 6.27: Shear-moment interaction diagram for Specimen C11T16.5-B2-ML at cut section located 1 foot from face of support.

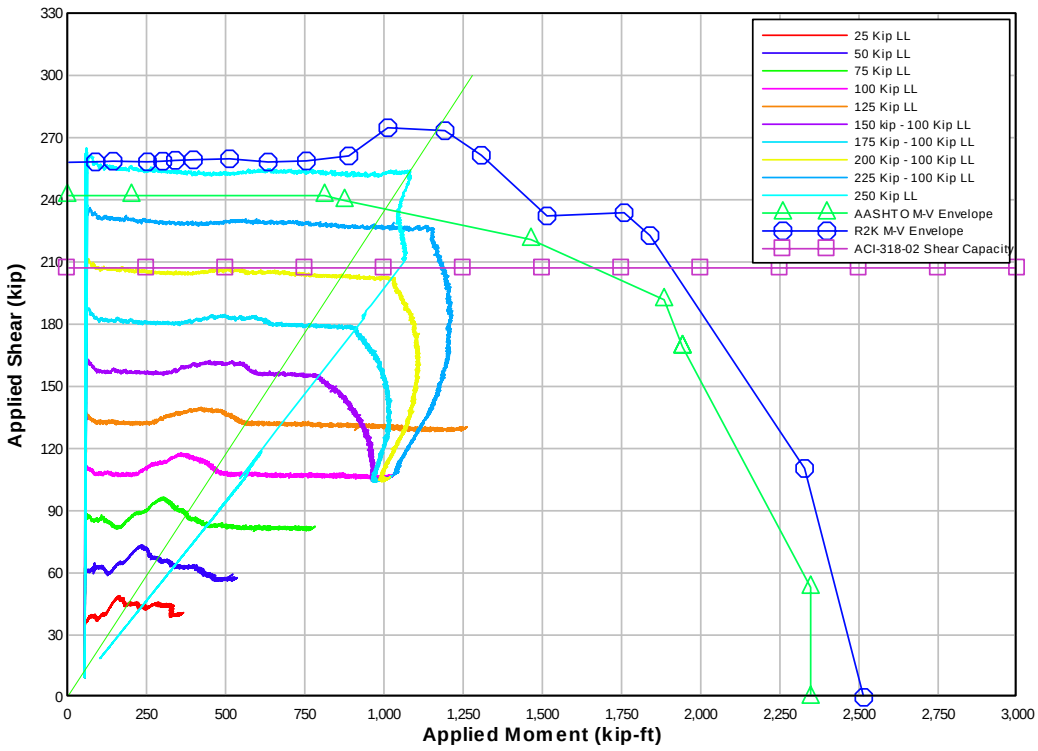

Figure 6.28: Shear-moment interaction diagram for Specimen C11T16.5-B2-ML at cut section located 2 feet from face of support.

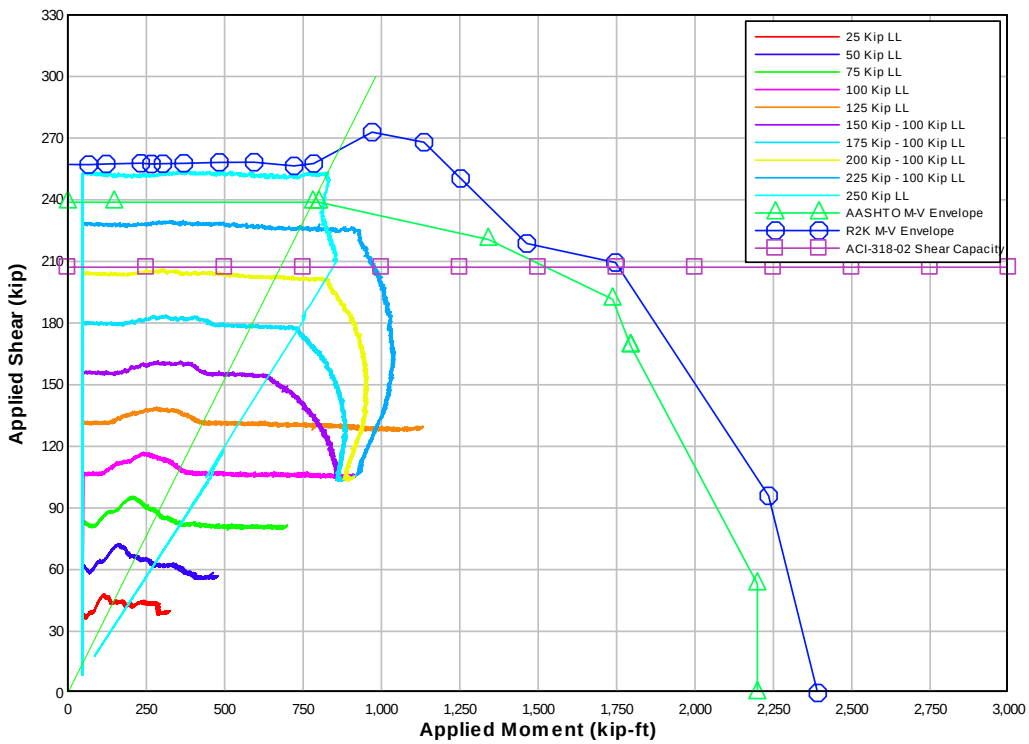

Figure 6.29: Shear-moment interaction diagram for Specimen C11T16.5-B2-ML at cut section located 3 feet from face of support.

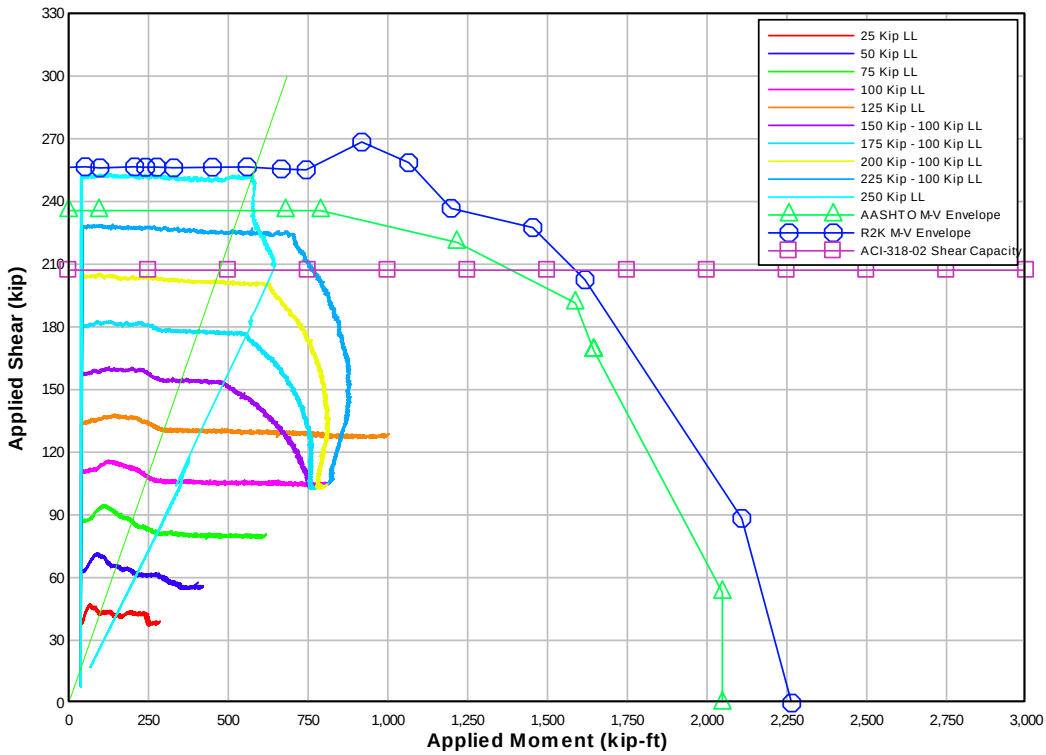

Figure 6.30: Shear-moment interaction diagram for Specimen C11T16.5-B2-ML at cut section located 4 feet from face of support.

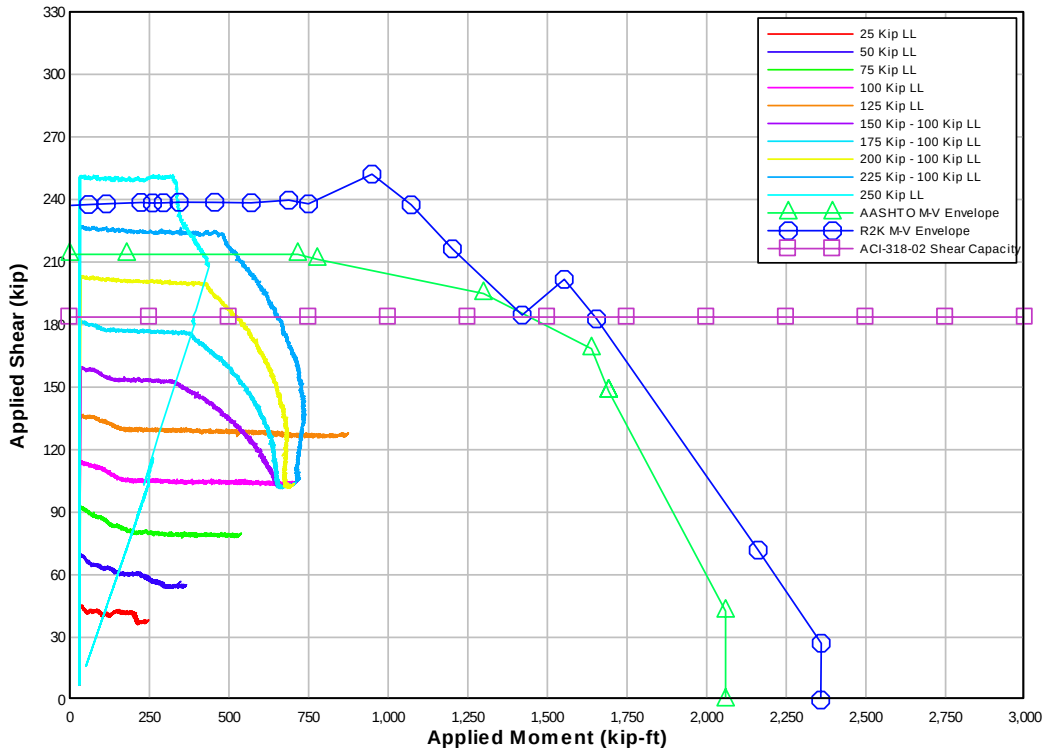

Figure 6.31: Shear-moment interaction diagram for Specimen C11T16.5-B2-ML at cut section located 5 feet from face of support.

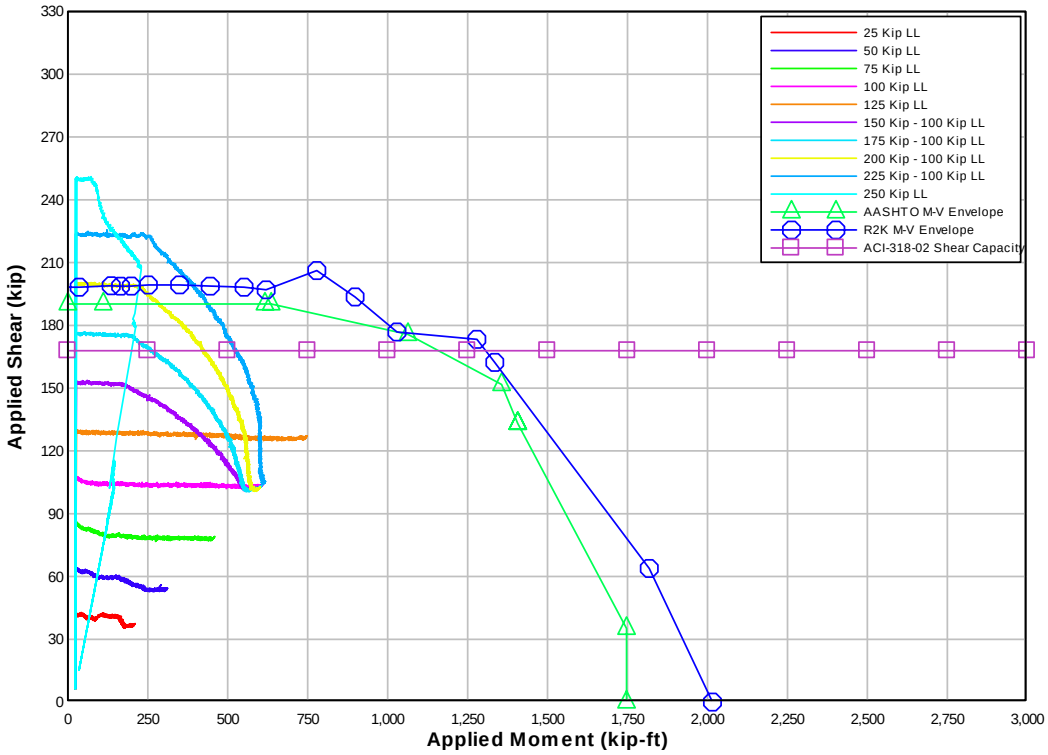

Figure 6.32: Shear-moment interaction diagram for Specimen C11T16.5-B2-ML at cut section located 6 feet from face of support.

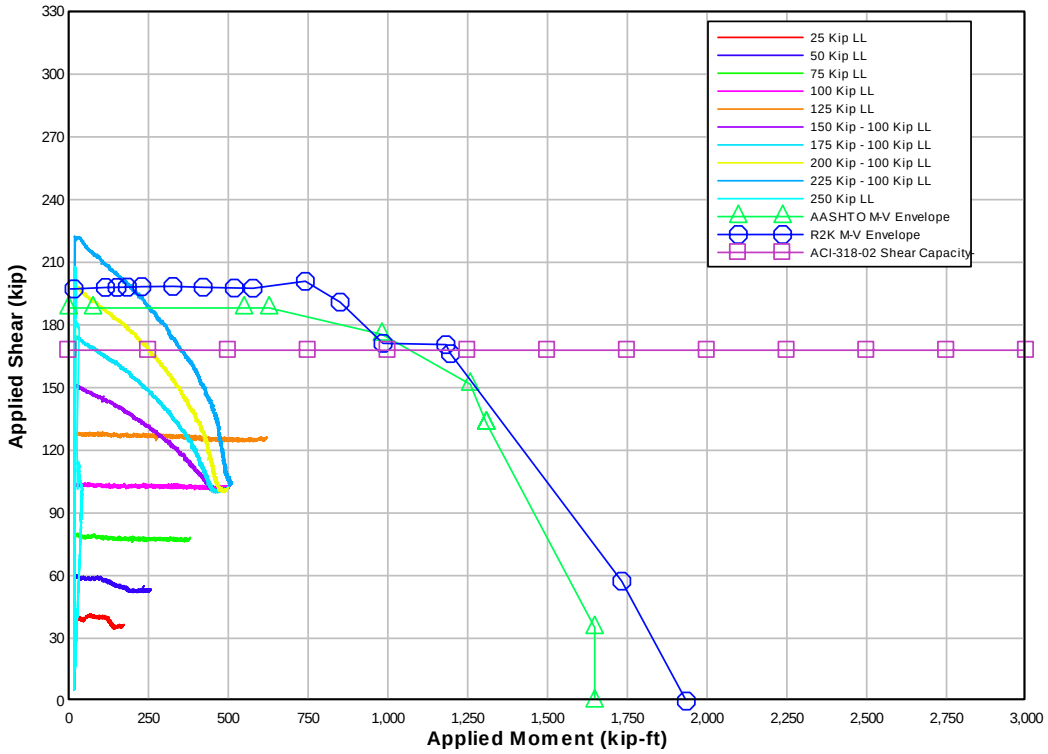

Figure 6.33: Shear-moment interaction diagram for Specimen C11T16.5-B2-ML at cut section located 7 feet from face of support.

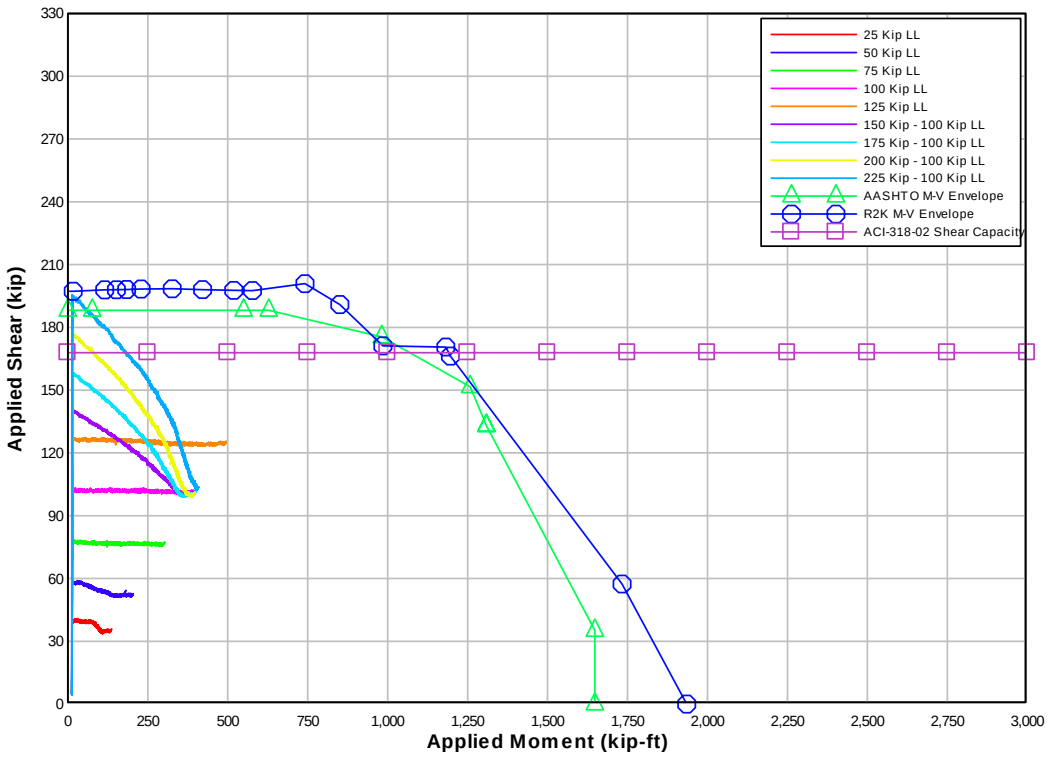

Figure 6.34: Shear-moment interaction diagram for Specimen C11T16.5-B2-ML at cut section located 8 feet from face of support.

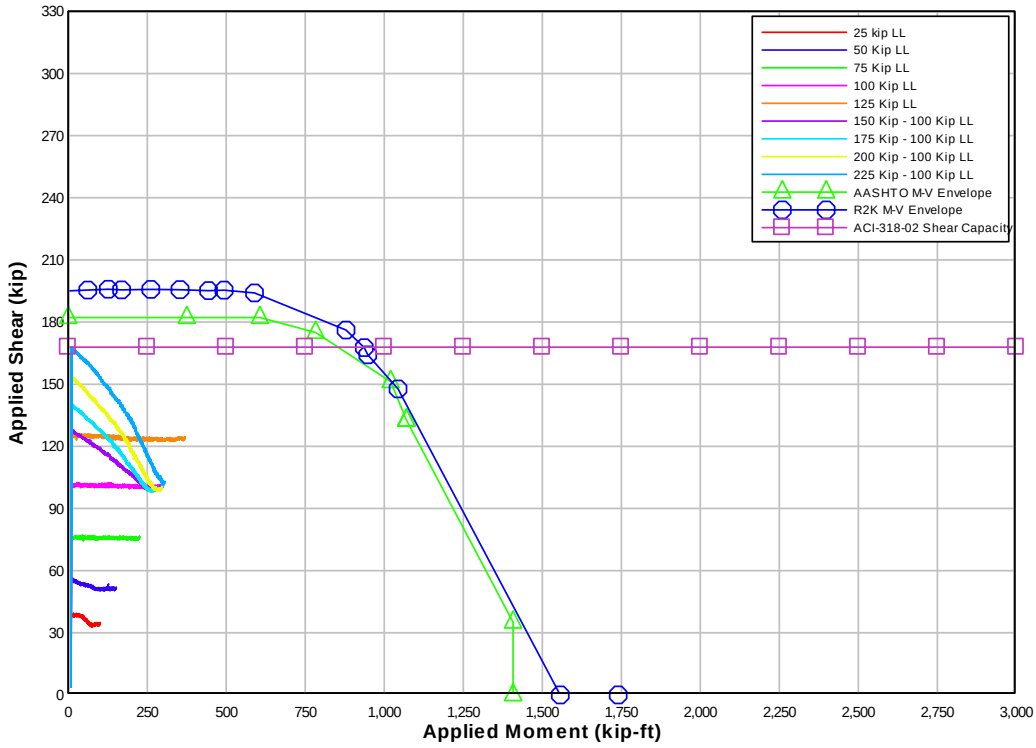

Figure 6.35: Shear-moment interaction diagram for Specimen C11T16.5-B2-ML at cut section located 9 feet from face of support.

6.2.4 C10T12-B2-ML

This specimen experienced a shear-dominated failure in the disturbed region near the left-hand support under an imposed live load of 971 kN (218.3 kips) located 1.50 m (4.91 ft) from the north face of support. The concrete crack pattern and failure conditions are shown in Figure 6.3. The peak imposed shear-moment values, shear-moment envelopes and ACI 318-02 shear capacity at each section are shown in Figures 6.36 through 6.45. Diagonal failure crack extended from the face of support upward at approximately 45º. The shear-moment at failure greatly exceeded the Response 2000™ and MCFT envelopes beginning at the face of support and extending approximately 2.13 m (7 ft) or two girder depths from the support, indicating the presence of truss/arch action within the disturbed region.

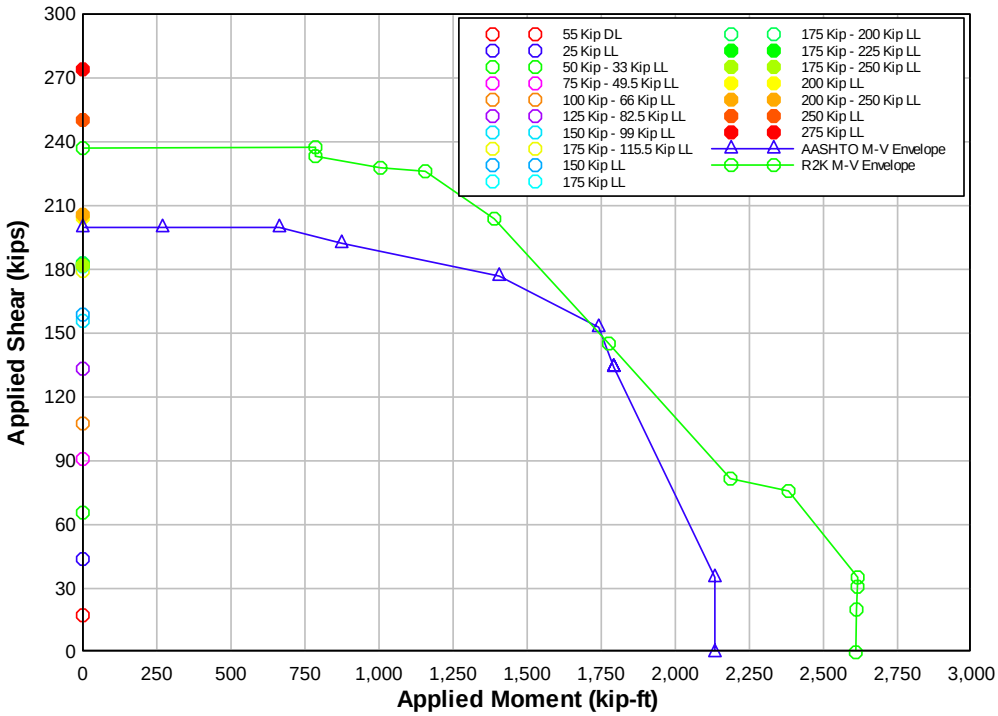

Figure 6.36: Shear-moment interaction diagram for Specimen C10T12-B2-ML at cut section located at face of support.

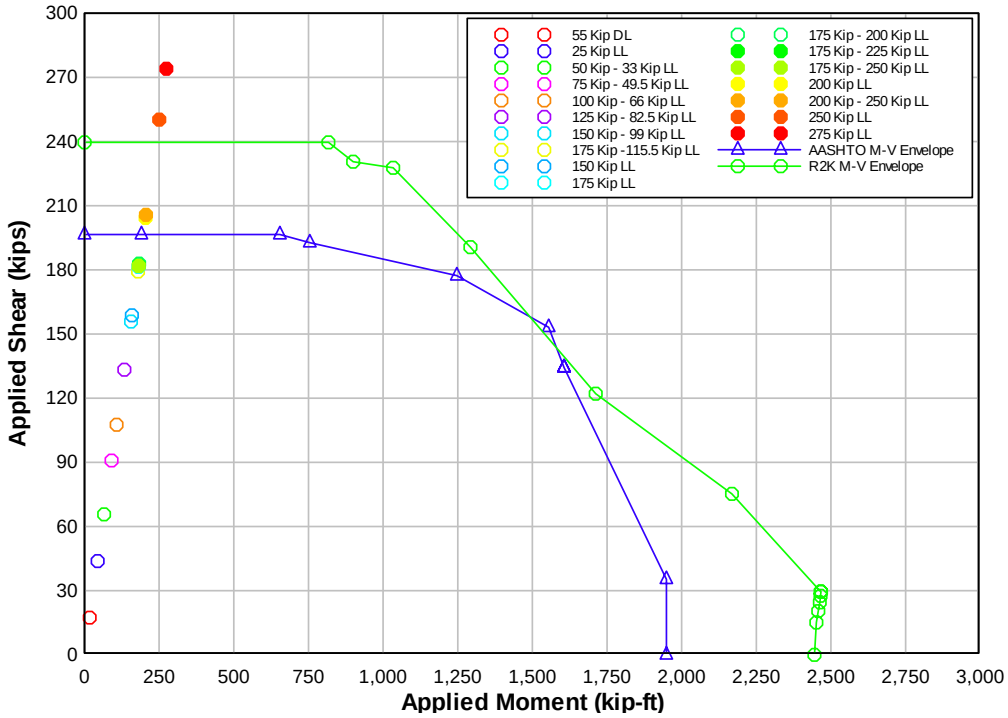

Figure 6.37: Shear-moment interaction diagram for Specimen C10T12-B2-ML at cut section located 1 foot from face of support.

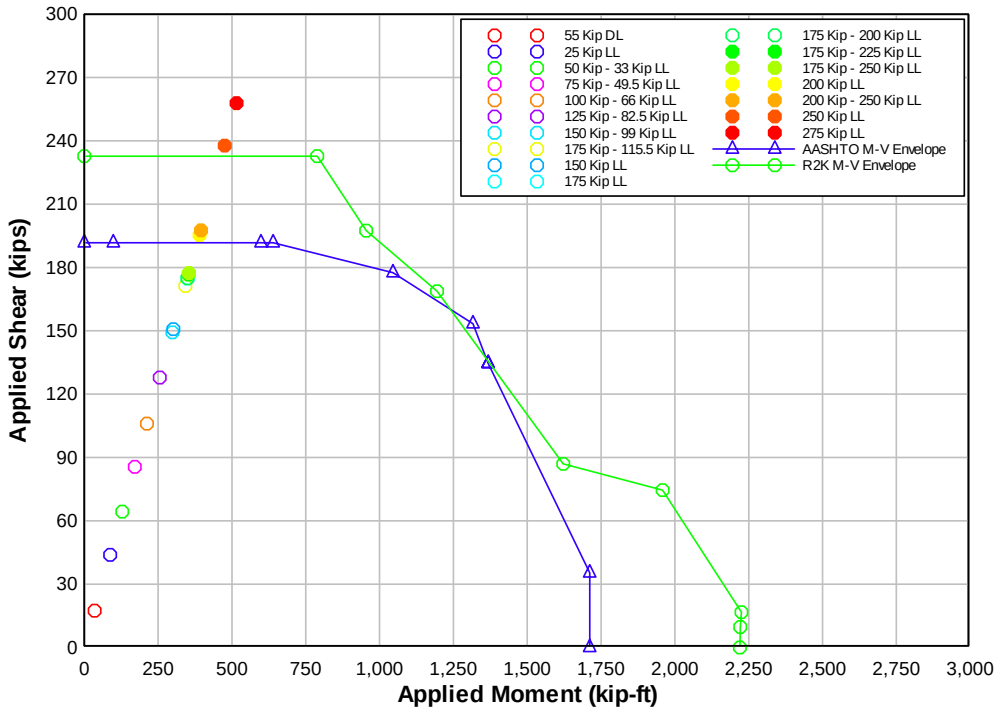

Figure 6.38: Shear-moment interaction diagram for Specimen C10T12-B2-ML at cut section located 2 feet from face of support.

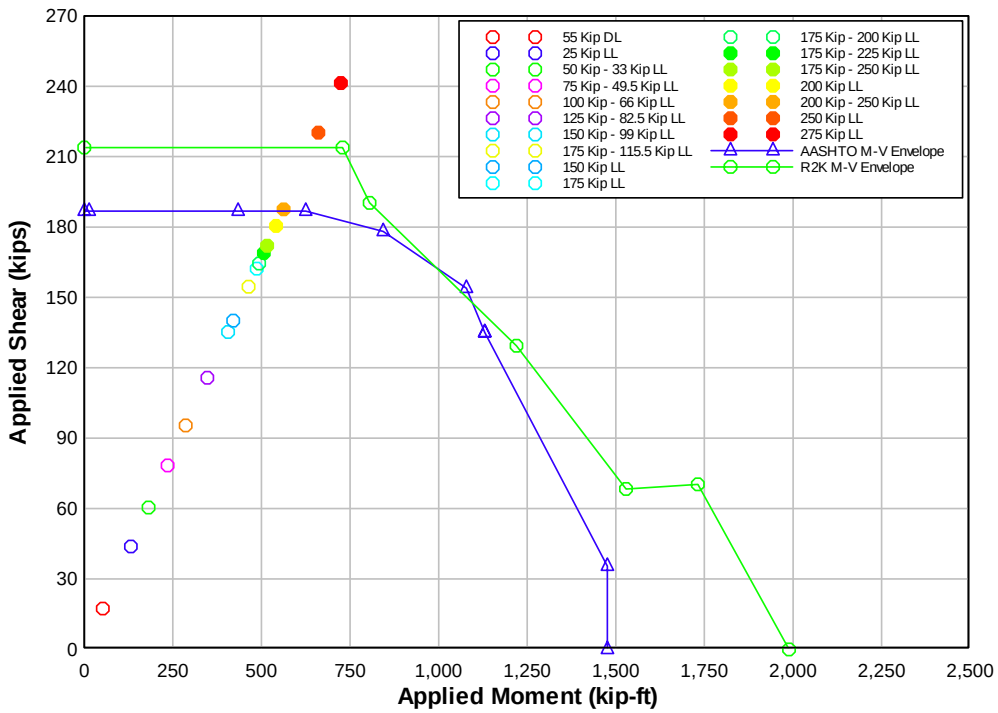

Figure 6.39: Shear-moment interaction diagram for Specimen C10T12-B2-ML at cut section located 3 feet from face of support.

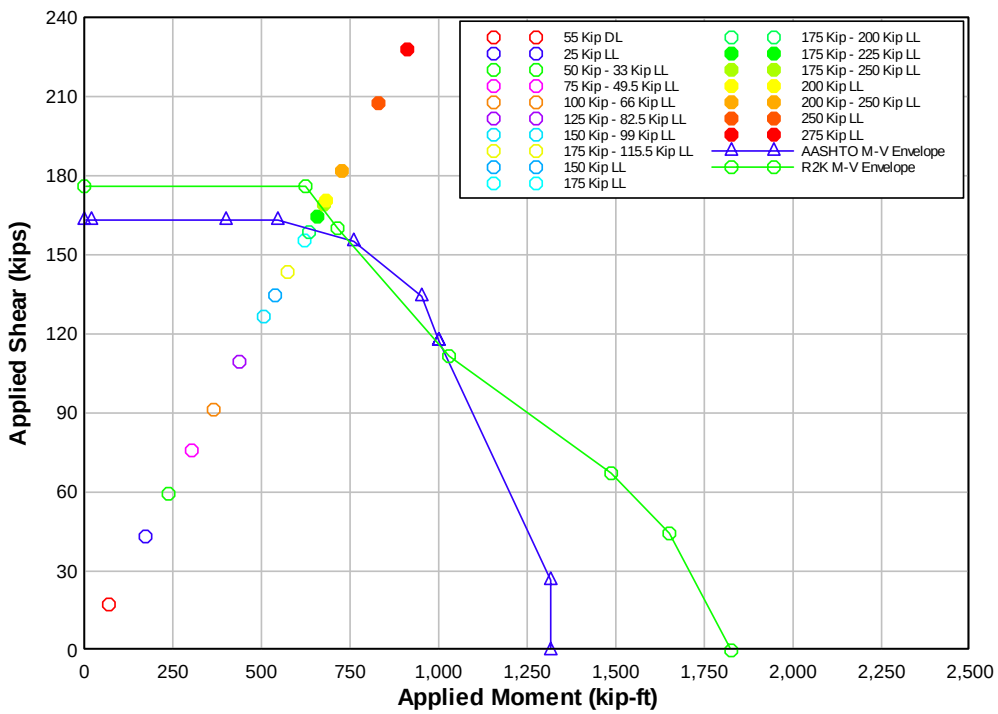

Figure 6.40: Shear-moment interaction diagram for Specimen C10T12-B2-ML at cut section located 4 feet from face of support.

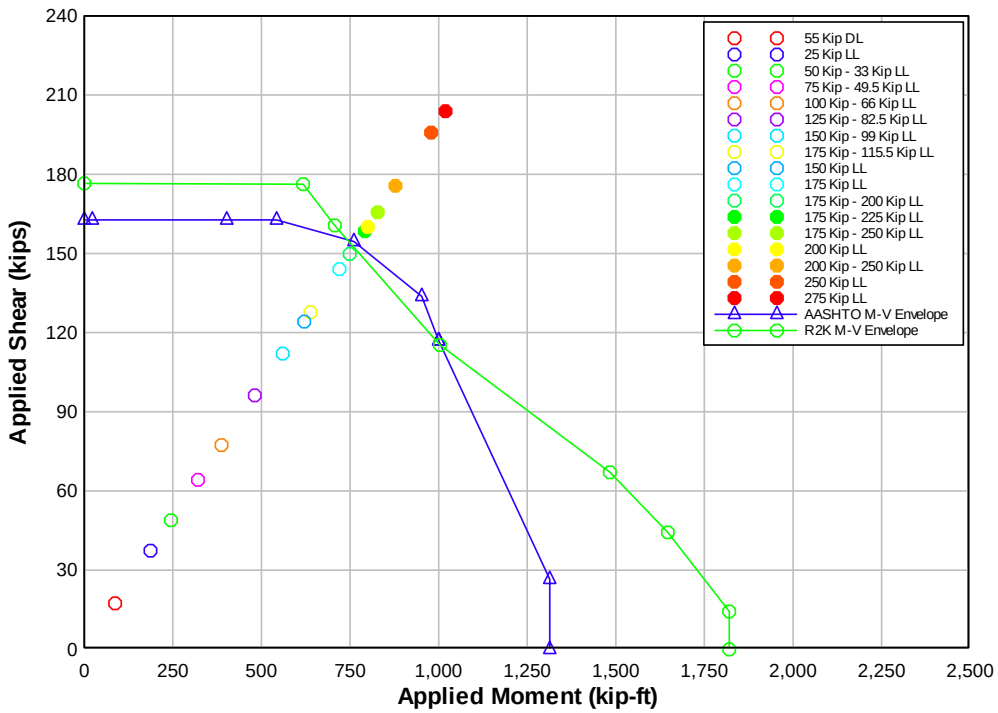

Figure 6.41: Shear-moment interaction diagram for Specimen C10T12-B2-ML at cut section located 5 feet from face of support.

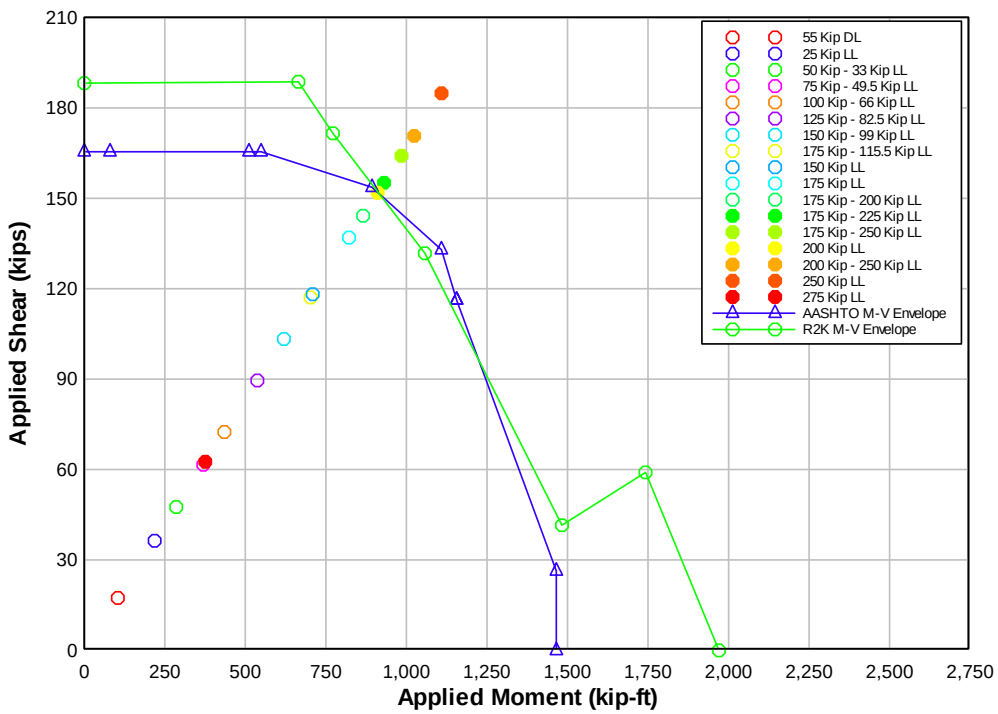

Figure 6.42: Shear-moment interaction diagram for Specimen C10T12-B2-ML at cut section located 6 feet from face of support.

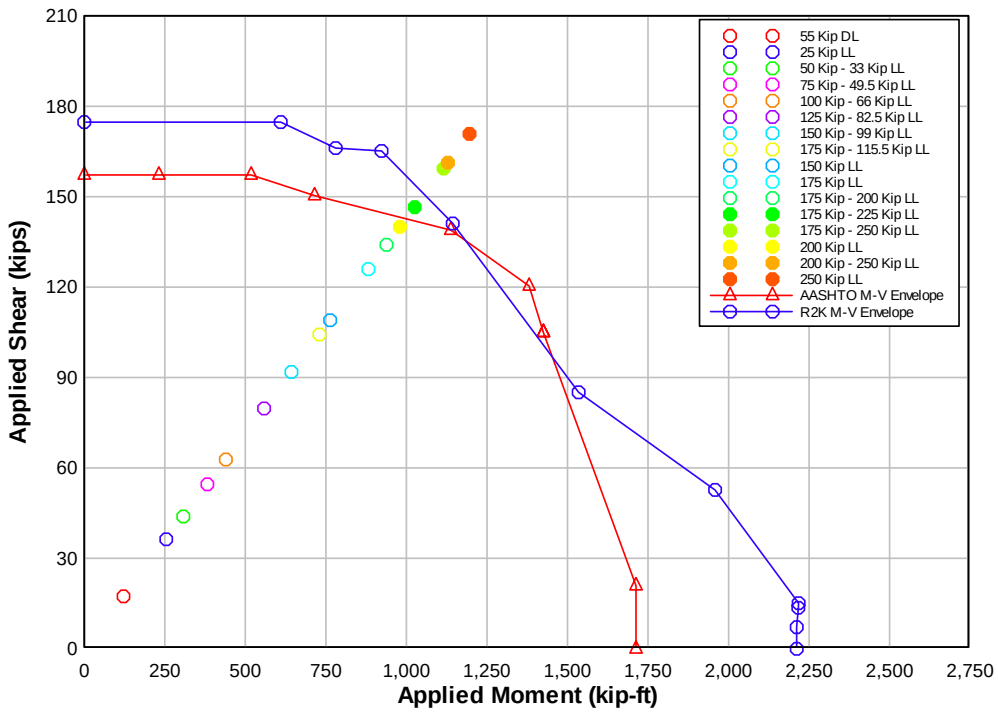

Figure 6.43: Shear-moment interaction diagram for Specimen C10T12-B2-ML at cut section located 7 feet from face of support.

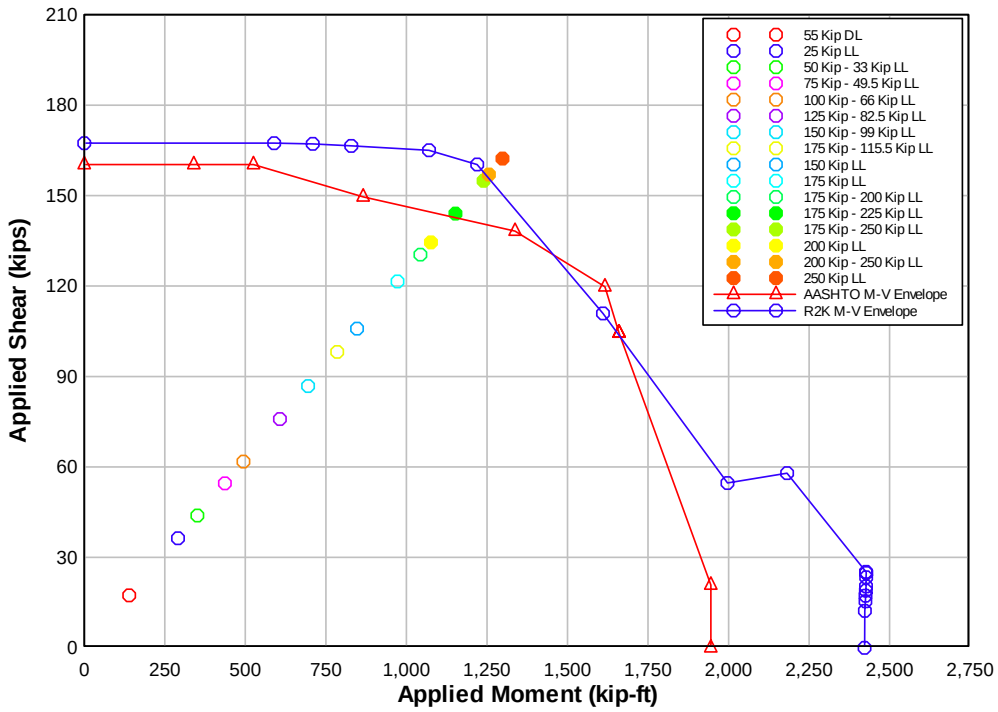

Figure 6.44: Shear-moment interaction diagram for Specimen C10T12-B2-ML at cut section located 8 feet from face of support.

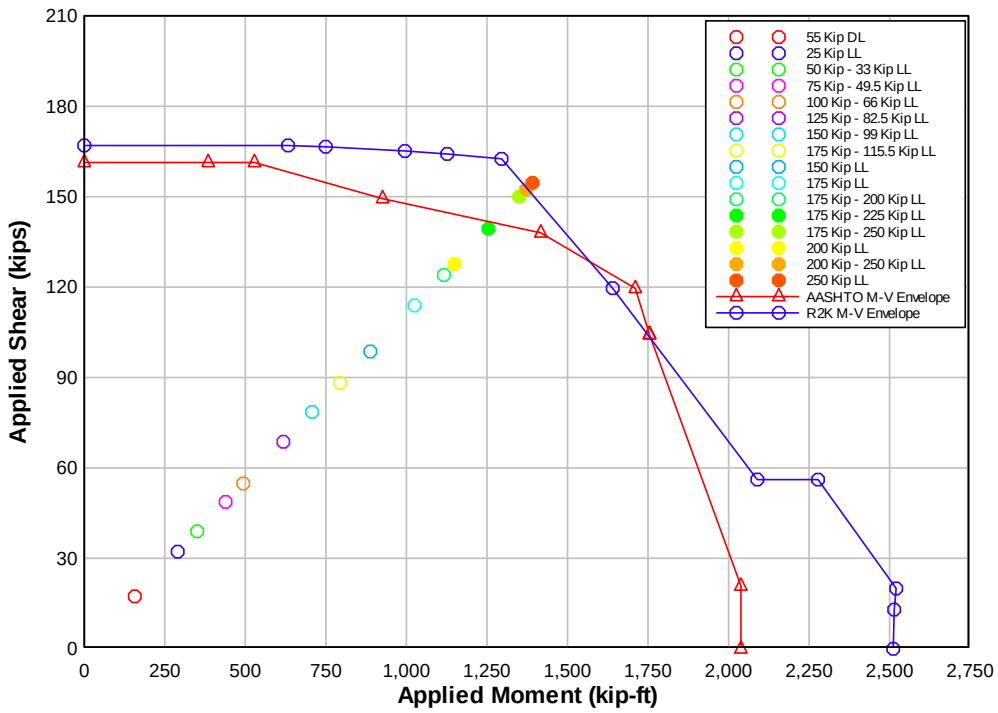

Figure 6.45: Shear-moment interaction diagram for Specimen C10T12-B2-ML at cut section located 9 feet from face of support.

The shear-moment value at failure exceeded the Response 2000™ and MCFT envelopes at the 2.44 m and 2.74 m (8 ft and 9 ft) sections during the 1110 kN (250 kip) load step. Failure might have occurred near the centerline of the specimen during the 1220 kN (275 kip) load step had the specimen not failed near the support early in the load step travel.

As previously noted, MCFT does not provide a good estimate of shear-moment capacity within disturbed regions. Therefore, two strut-and-tie models of the failed specimen (Figure 6.46) were used to evaluate the imposed live load capacity. Model A is a simple prismatic strut model that might be used in practice to evaluate the flexure-shear capacity of a deep beam. Model A yielded a predicted live load capacity of 365 kN (82 kips), 38% of the live load capacity actually achieved in the laboratory. The failure mode of Model A was controlled by the flexural tie anchorage capacity at Node B due to poor anchorage details and the long straight bar development lengths associated with #11 deformed bars. An improved model was developed by replacing the prismatic strut with four (4) struts arranged in an arch restrained by the three stirrups that cross the failure crack. Model B yielded an improved live load capacity prediction of 818 kN (184 kips), 84% of the capacity achieved in the laboratory.

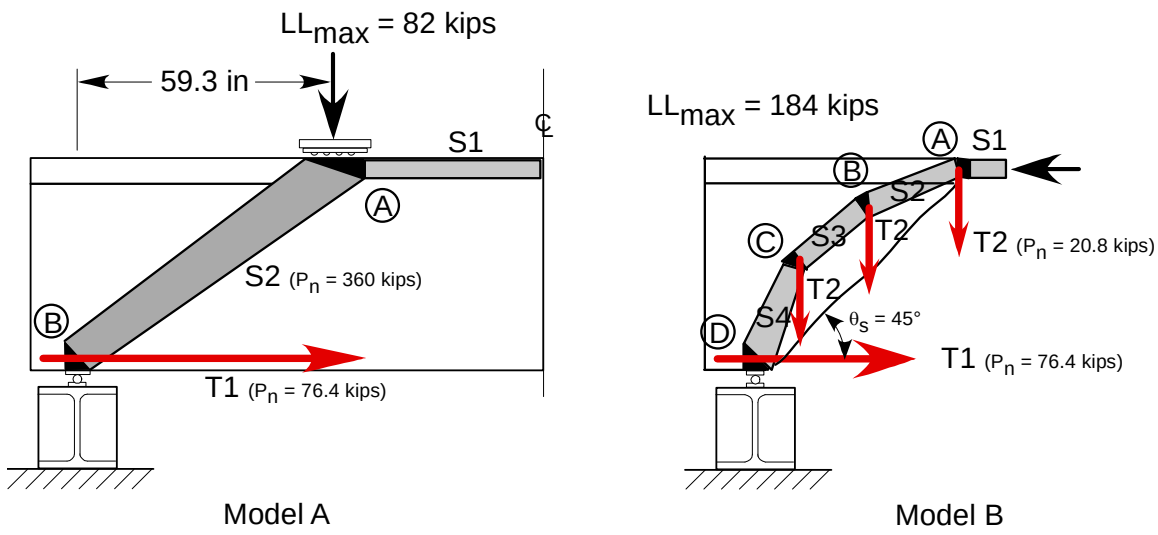

Figure 6.46: Strut and Tie used to estimate shear-dominated capacity near simple support of Specimen C10T16-B2-ML. Model A used a straight, prismatic strut. Model B used a series of struts restrained by stirrups.

6.2.5 C11IT16-B1-ML

This specimen failed in shear compression at an imposed live load of 1735 kN (390 kips). The concrete crack pattern and failure conditions are shown in Figure 6.1. The imposed shear-moment histories, shear-moment envelopes and ACI 318-02 shear capacity at each section of the north (right-hand) and south (left-hand) side of the simply supported span are shown in Figures 6.47 through 6.57 and Figures 6.58 through 6.67, respectively. Different shear-to-moment ratios were developed within each half of the specimen using the asymmetric supports shown in Figure 6.1. The specimen failed on the south side of the span at an applied shear of approximately 912 kN (205 kips). The failure crack extended from approximately 1.52 m to 2.74 m (5 ft to 9 ft) from the face of support. At 1.22 m (4 ft), the shear-moment value at failure exceeded the Response 2000™ envelope. At 1.52 m thru 2.44 m (5 ft thru 8 ft), the peak shear-moment value fell between the Response 2000™ and MCFT envelopes. The peak shear-moment values again exceeded the Response 2000™ envelope at 2.74 m (9ft). Response 2000™ appeared to reasonably predict the shear-moment capacity while MCFT provided a conservative estimate of the shear-moment capacity at all sections along the failure crack. Again, ACI 318-02 greatly underestimated the shear capacity at all sections.

From the face of support to 0.91 m (3 ft), where the left-hand span did not fail, the imposed shear dominated the imposed moment and the peak shear-moment value again greatly exceeded the Response 2000™ and MCFT envelopes. It is significant to note that in the right-hand span the peak shear-moment value exceeded the Response 2000™ envelope from the face of support thru 1.52 m (5 ft) and fell between the Response 200 and MCFT envelopes at 1.83 m, 2.74 m and 3.05 m (6 ft, 9 ft and 10 ft) but did not induce failure.

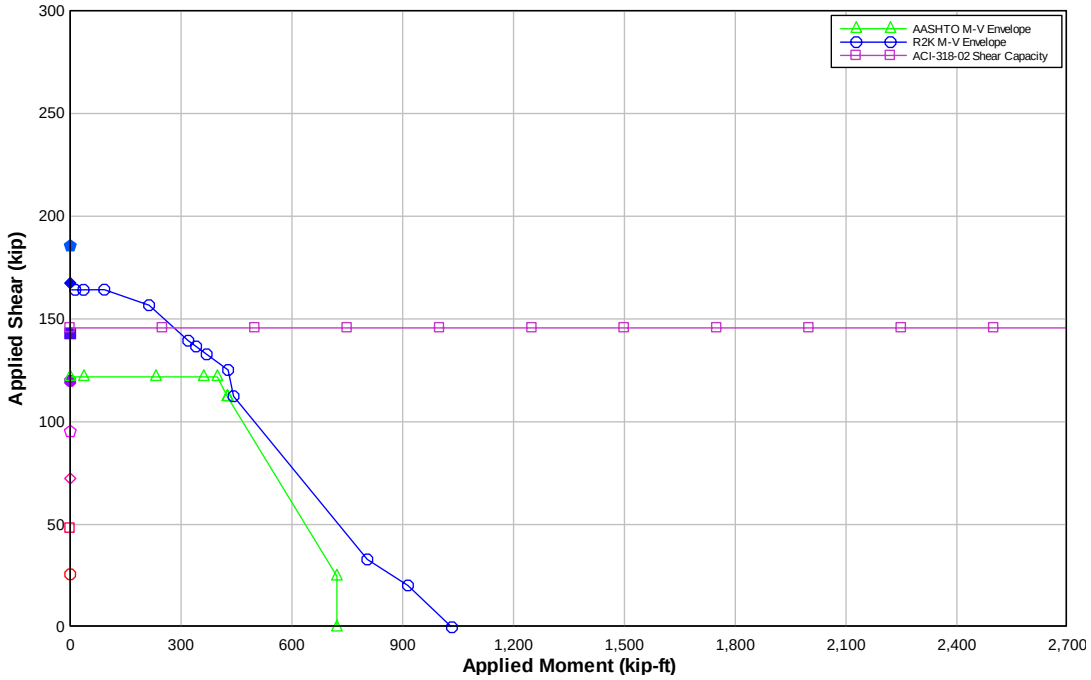

Figure 6.47: Shear-moment interaction diagram for the right-hand side of Specimen C11IT16-B1-ML at cut section located at the face of support

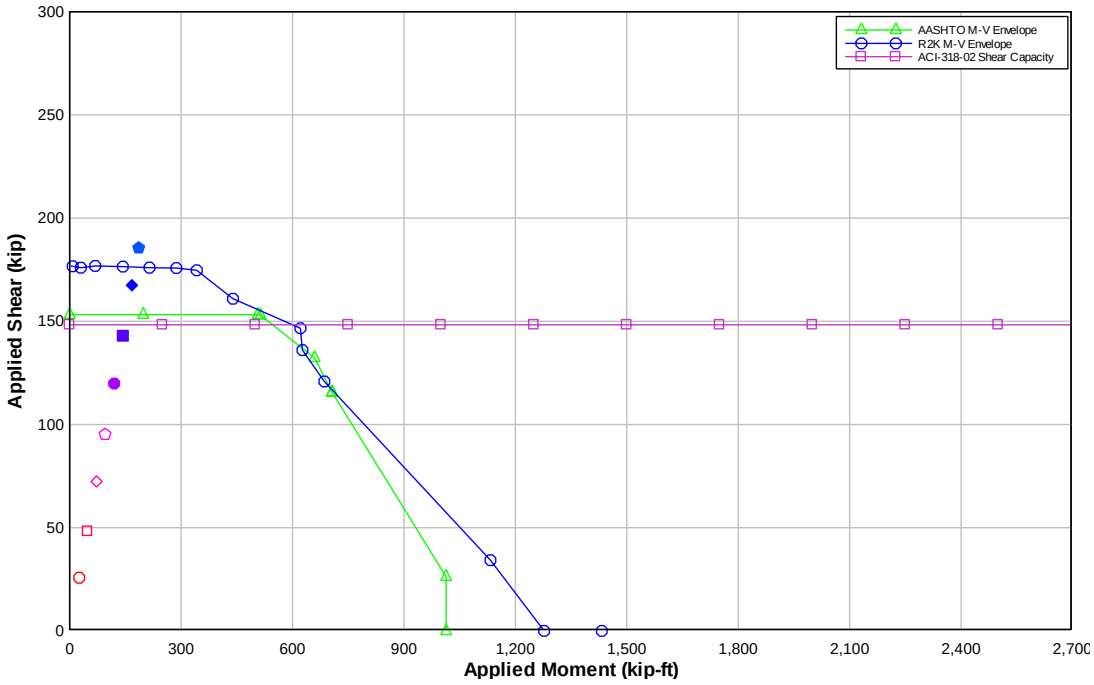

Figure 6.48: Shear-moment interaction diagram for the right-hand side of Specimen C11IT16-B1-ML at cut section located 1 foot from the face of support

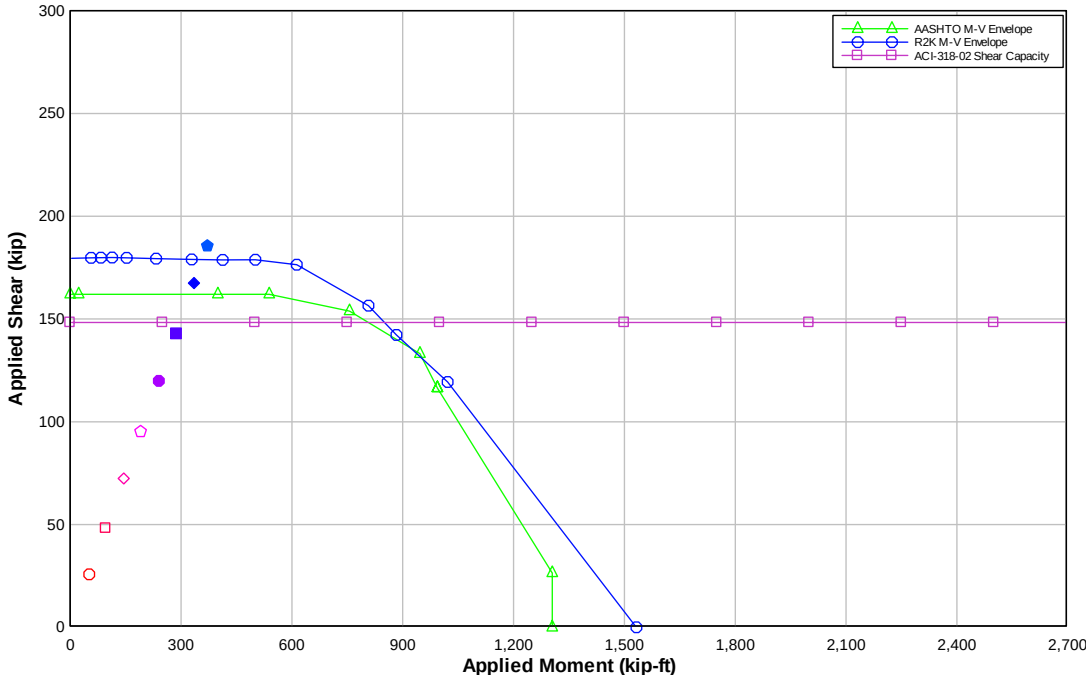

Figure 6.49: Shear-moment interaction diagram for the right-hand side of Specimen C11IT16-B1-ML at cut section located 2 feet from the face of support

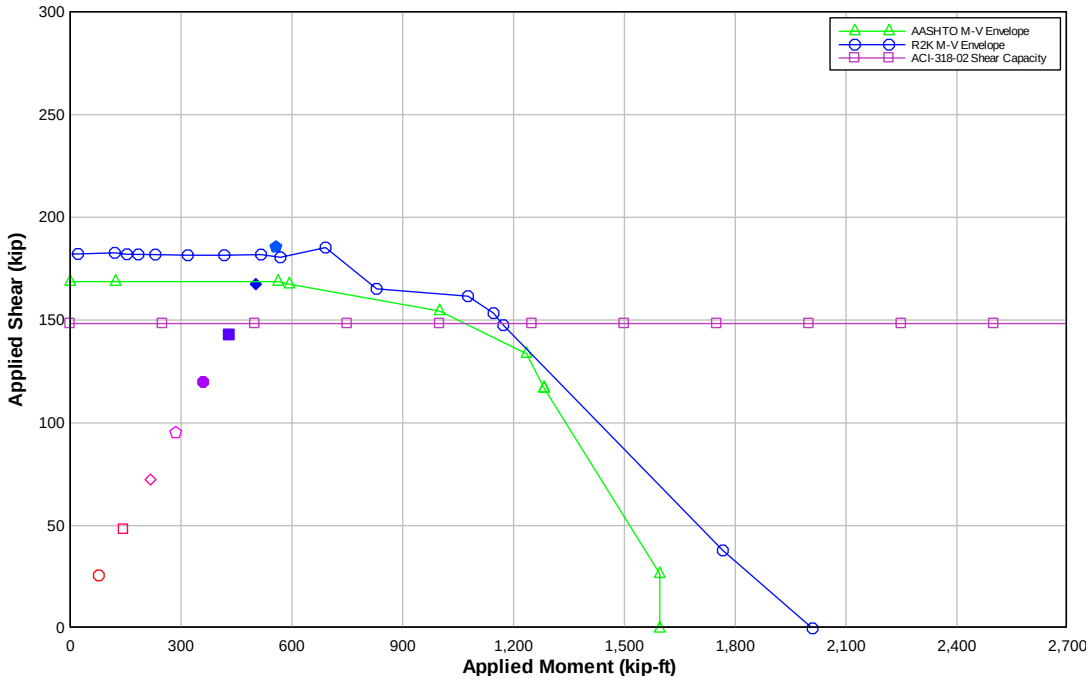

Figure 6.50: Shear-moment interaction diagram for the right-hand side of Specimen C11IT16-B1-ML at cut section located 3 feet from the face of support

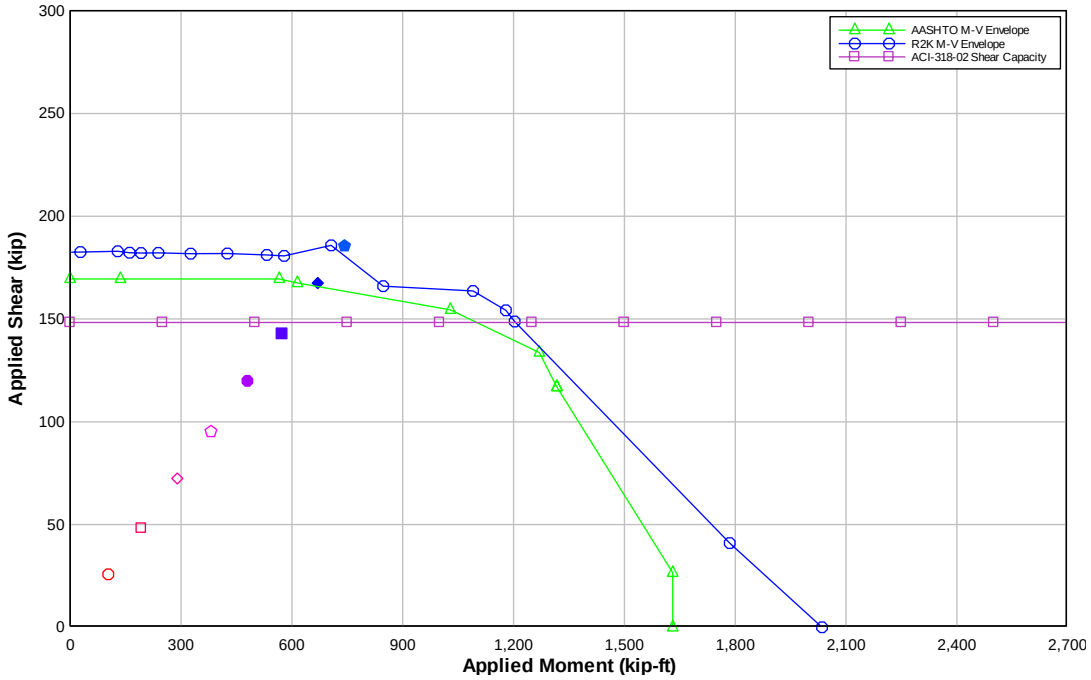

Figure 6.51: Shear-moment interaction diagram for the right-hand side of Specimen C11IT16-B1-ML at cut section located 4 feet from the face of support

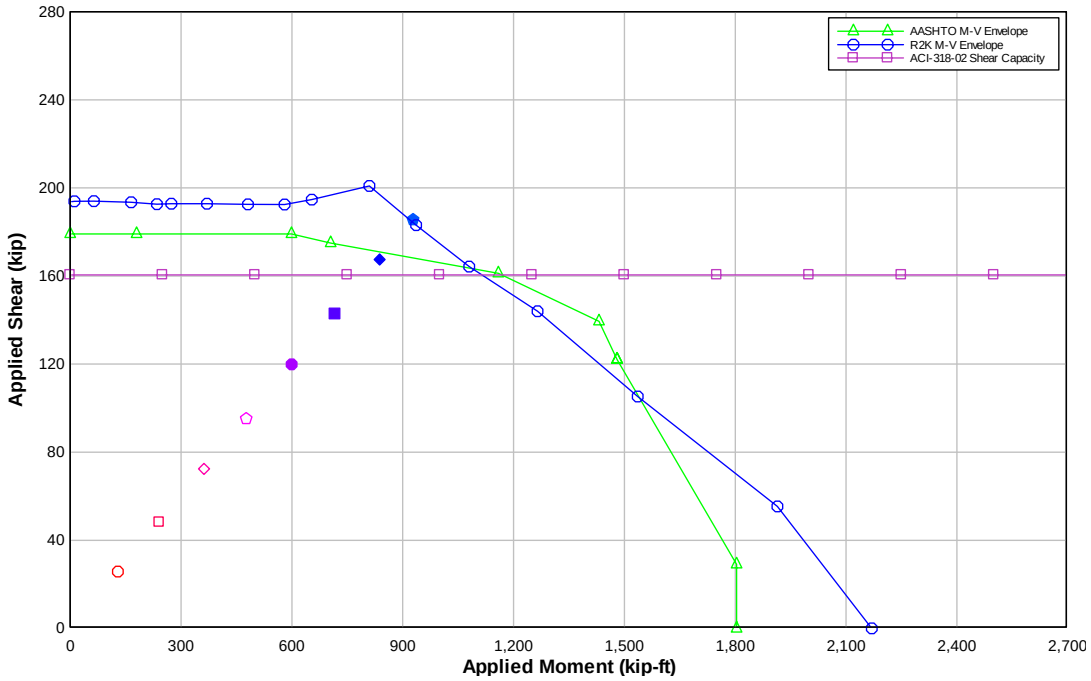

Figure 6.52: Shear-moment interaction diagram for the right-hand side of Specimen C11IT16-B1-ML at cut section located 5 feet from the face of support

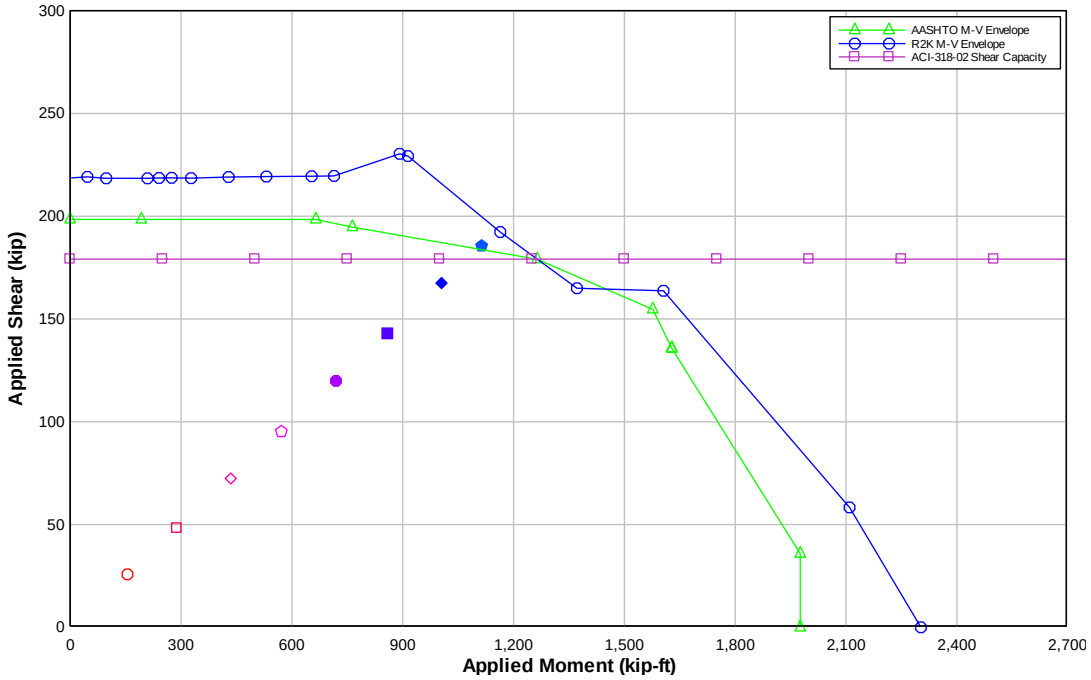

Figure 6.53: Shear-moment interaction diagram for the right-hand side of Specimen C11IT16-B1-ML at cut section located 6 feet from the face of support

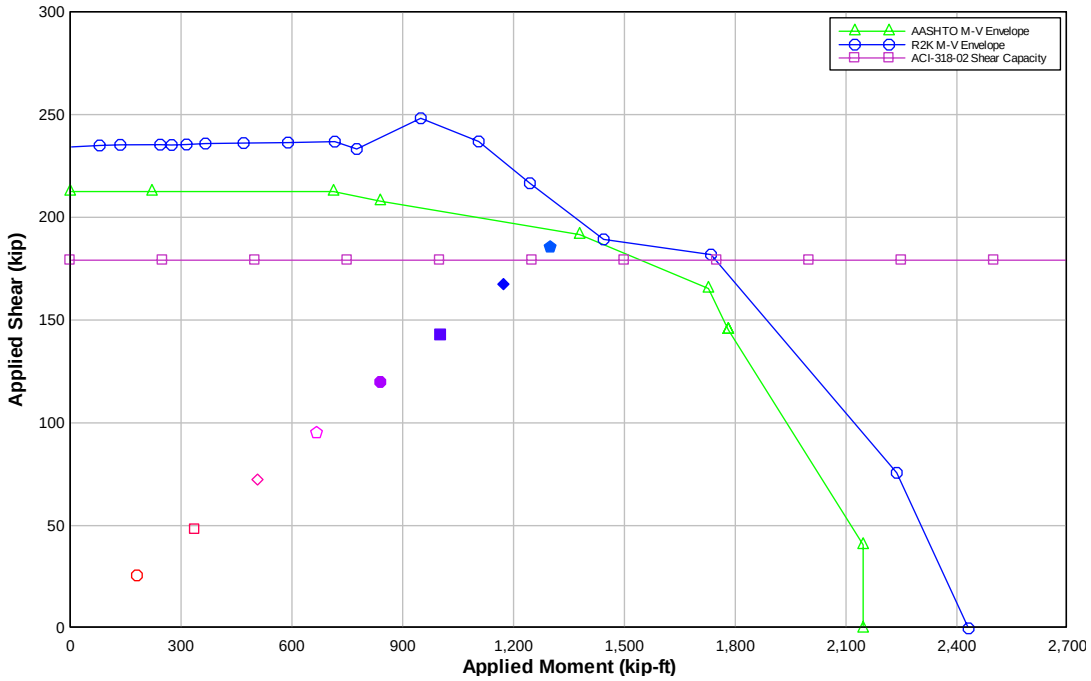

Figure 6.54: Shear-moment interaction diagram for the right-hand side of Specimen C11IT16-B1-ML at cut section located 7 feet from the face of support

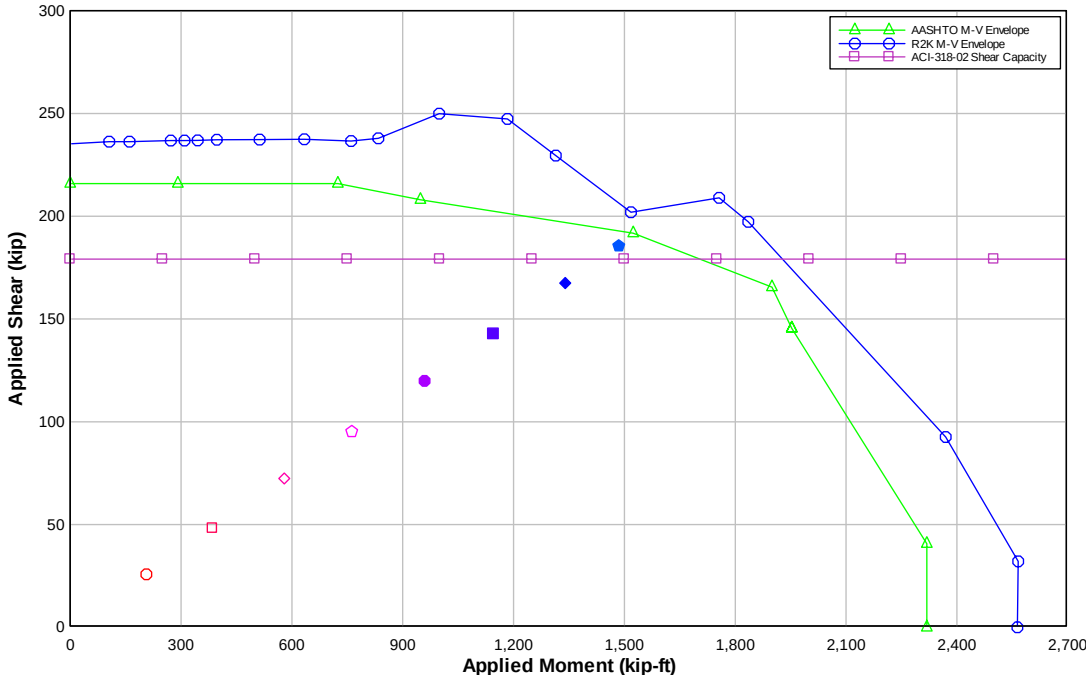

Figure 6.55: Shear-moment interaction diagram for the right-hand side of Specimen C11IT16-B1-ML at cut section located 8 feet from the face of support

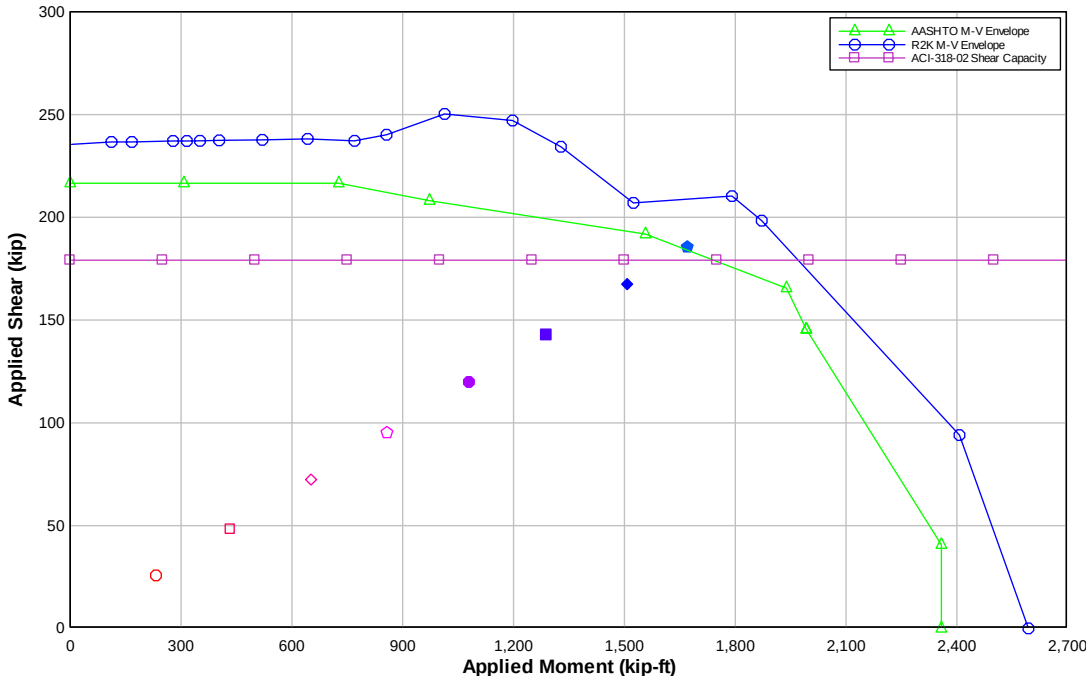

Figure 6.56: Shear-moment interaction diagram for the right-hand side of Specimen C11IT16-B1-ML at cut section located 9 feet from the face of support

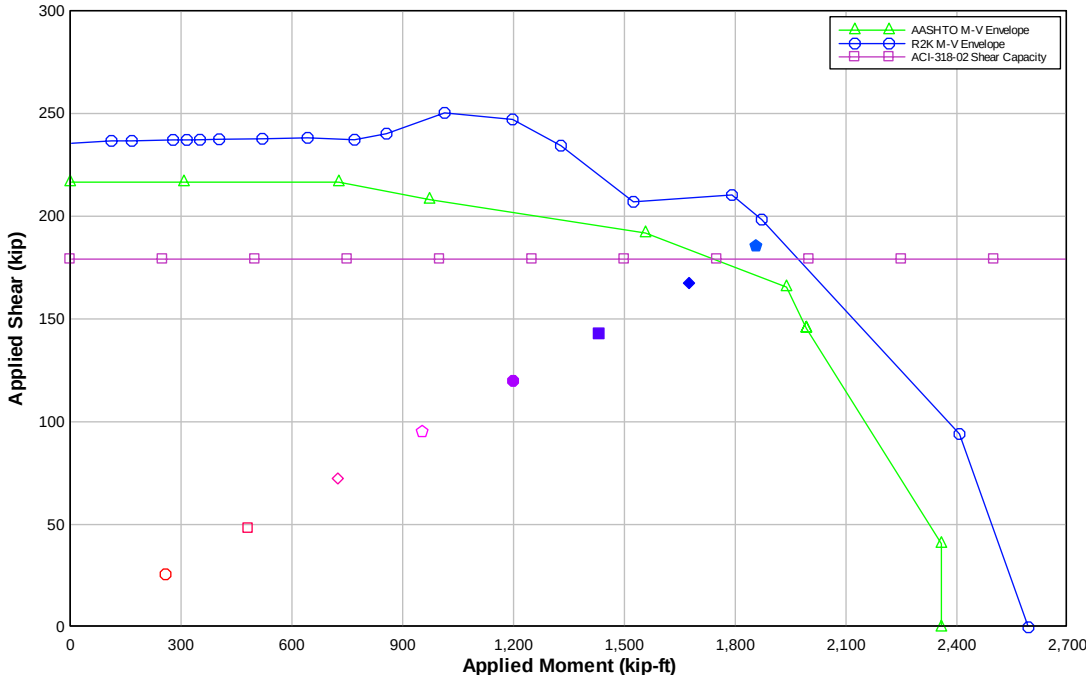

Figure 6.57: Shear-moment interaction diagram for the right-hand side of Specimen C11IT16-B1-ML at cut section located 10 feet from the face of support

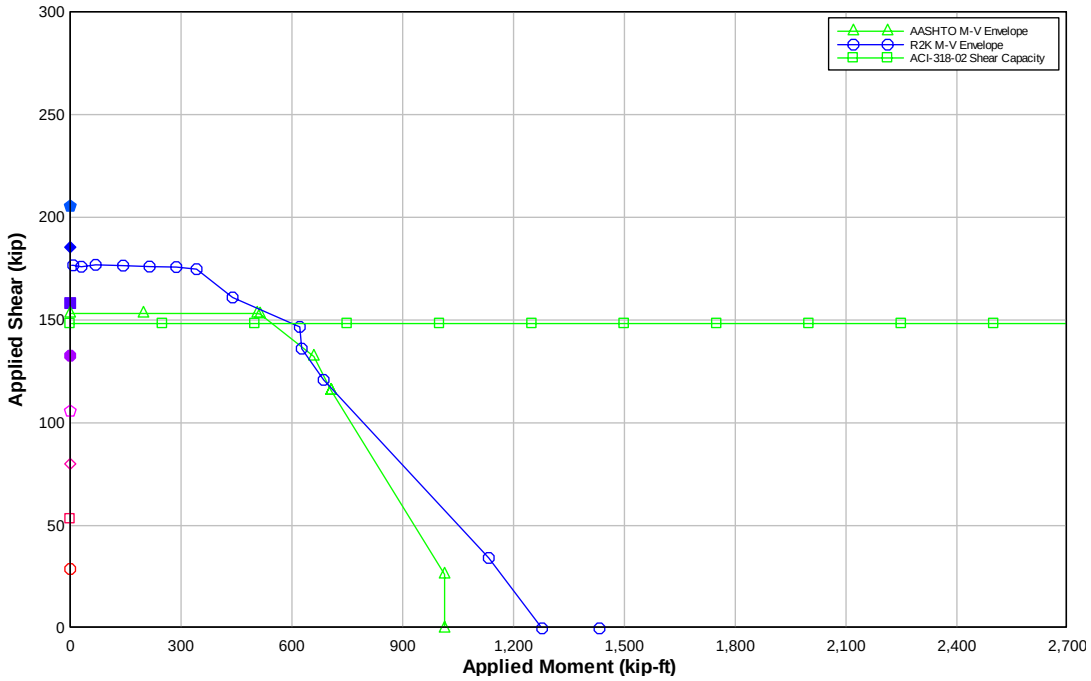

Figure 6.58: Shear-moment interaction diagram for left-hand side of Specimen C11IT16-B1-ML at cut section located at face of support.

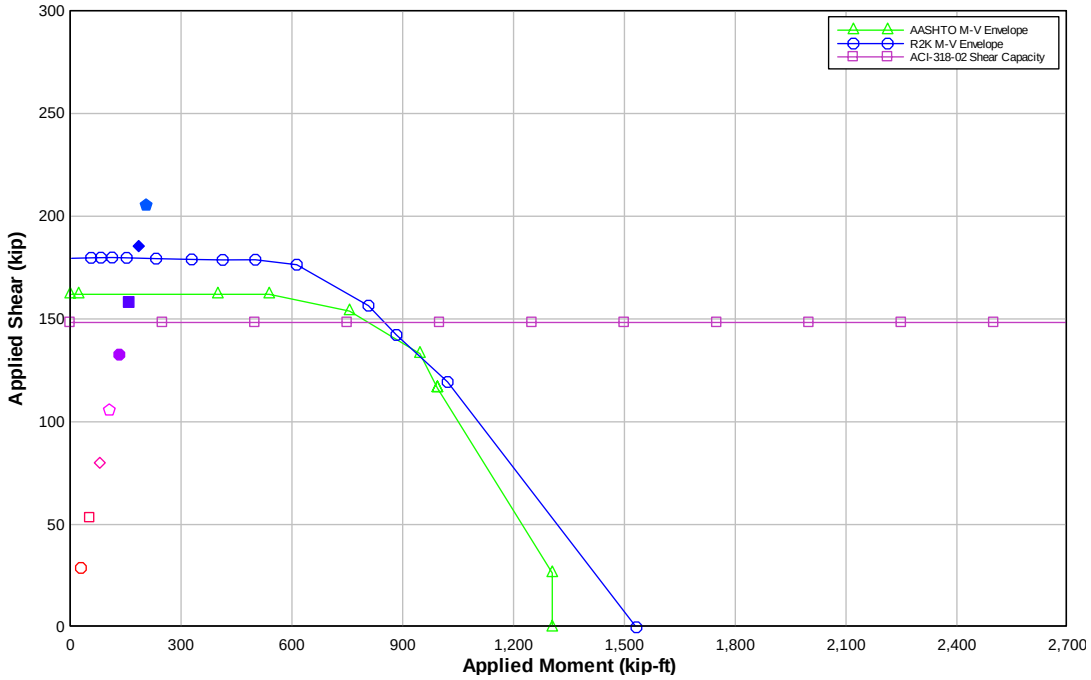

Figure 6.59: Shear-moment interaction diagram for left-hand side of Specimen C11IT16-B1-ML 1 foot from cut section located at face of support.

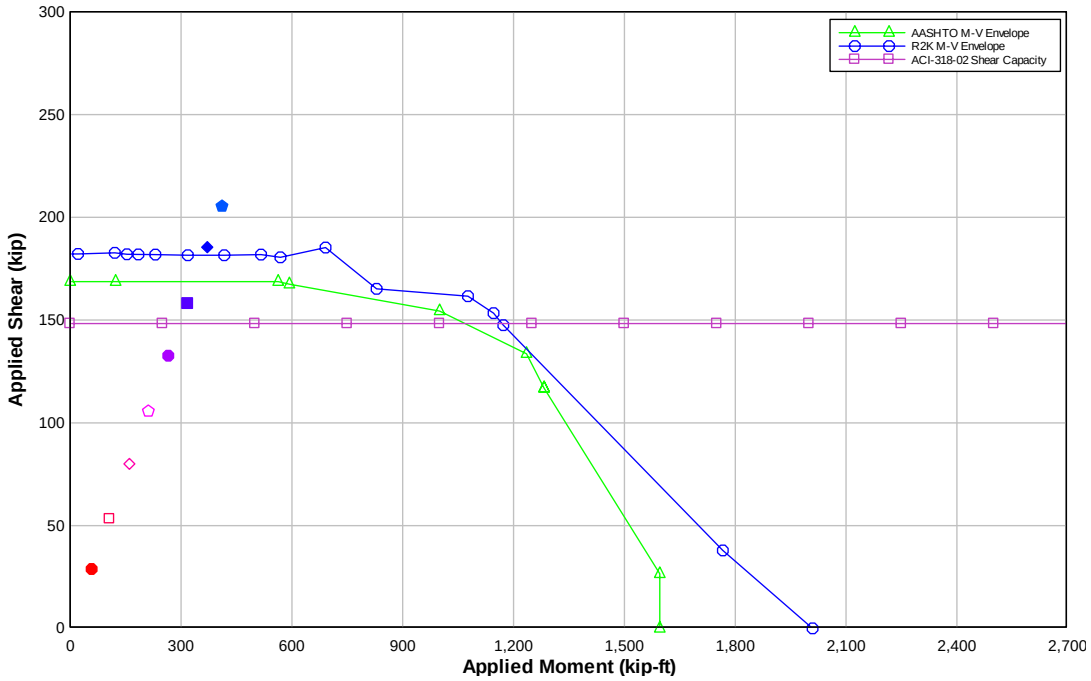

Figure 6.60: Shear-moment interaction diagram for left-hand side of Specimen C11IT16-B1-ML 2 feet from cut section located at face of support.

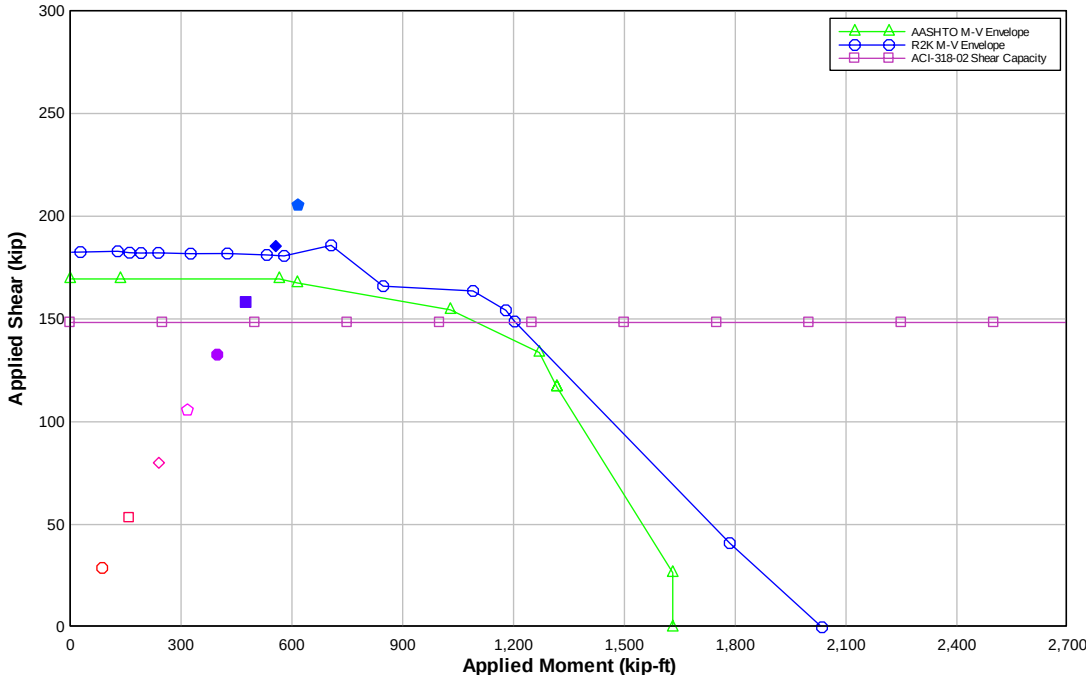

Figure 6.61: Shear-moment interaction diagram for left-hand side of Specimen C11IT16-B1-ML 3 feet from cut section located at face of support.

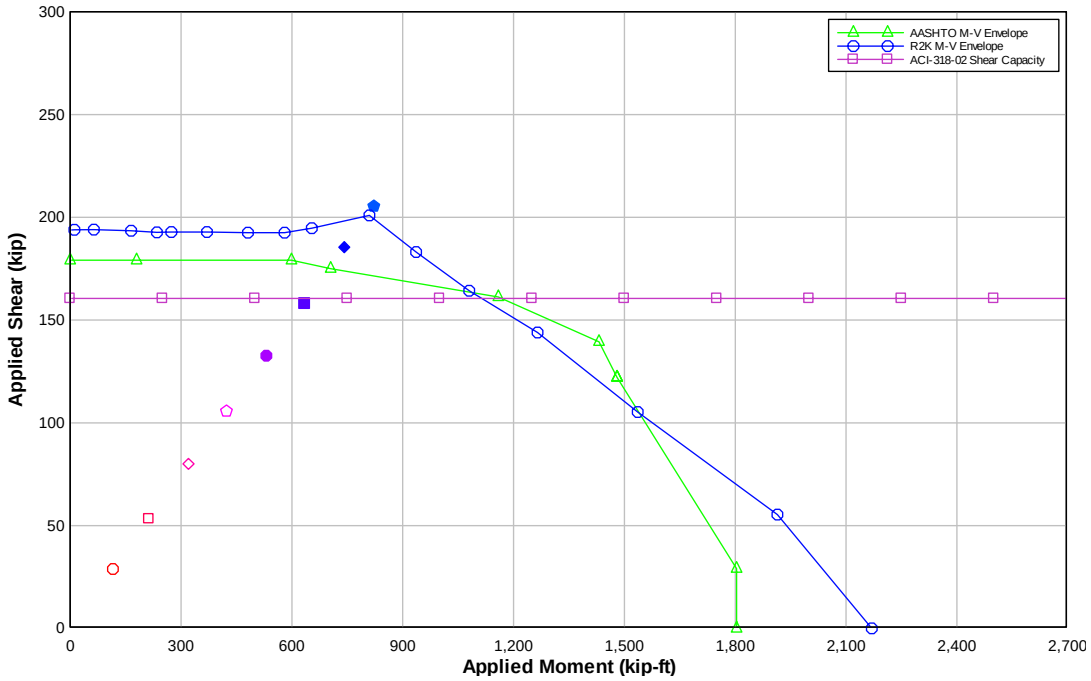

Figure 6.62: Shear-moment interaction diagram for left-hand side of Specimen C11IT16-B1-ML 4 feet from cut section located at face of support.

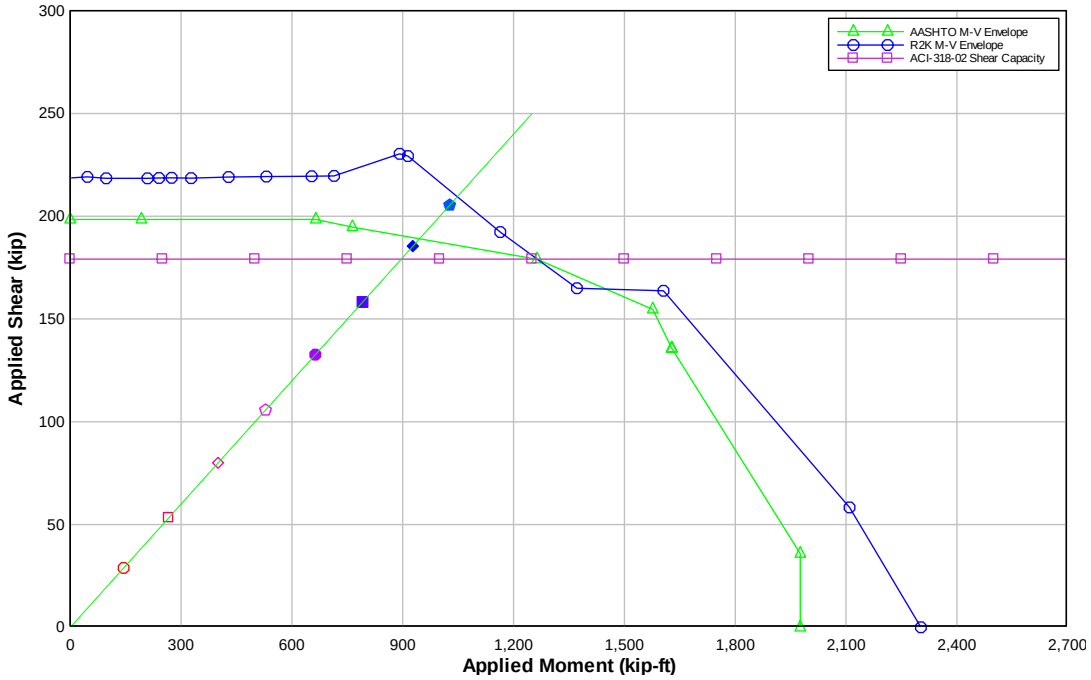

Figure 6.63: Shear-moment interaction diagram for left-hand side of Specimen C11IT16-B1-ML 5 feet from cut section located at face of support.

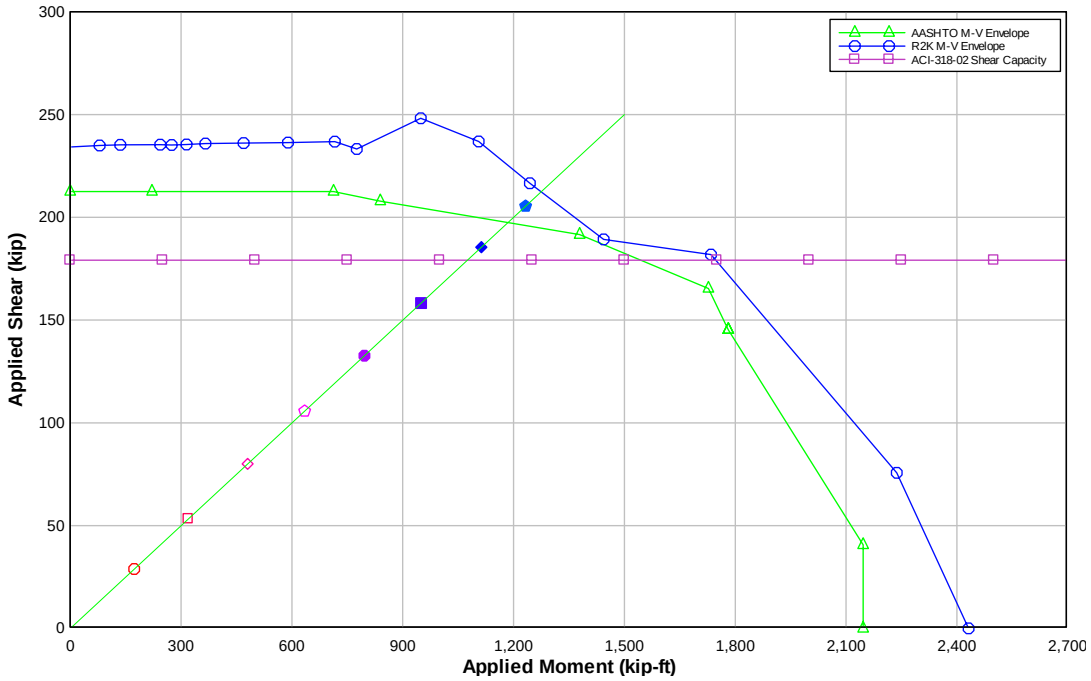

Figure 6.64: Shear-moment interaction diagram for left-hand side of Specimen C11IT16-B1-ML 6 feet from cut section located at face of support.

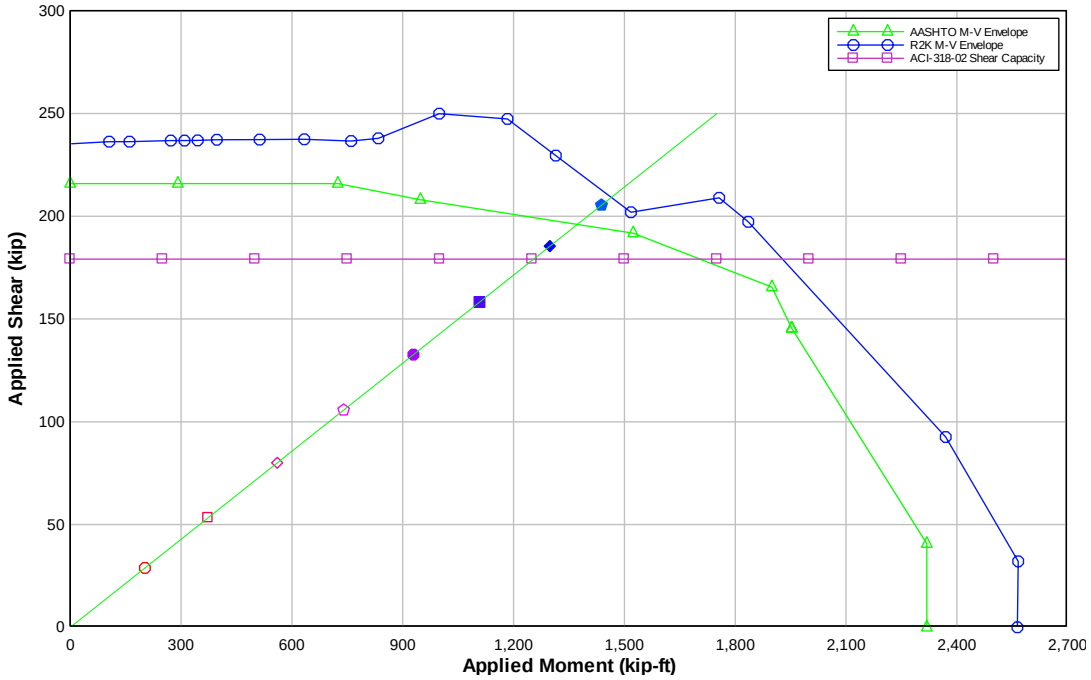

Figure 6.65: Shear-moment interaction diagram for left-hand side of Specimen C11IT16-B1-ML 7 feet from cut section located at face of support.

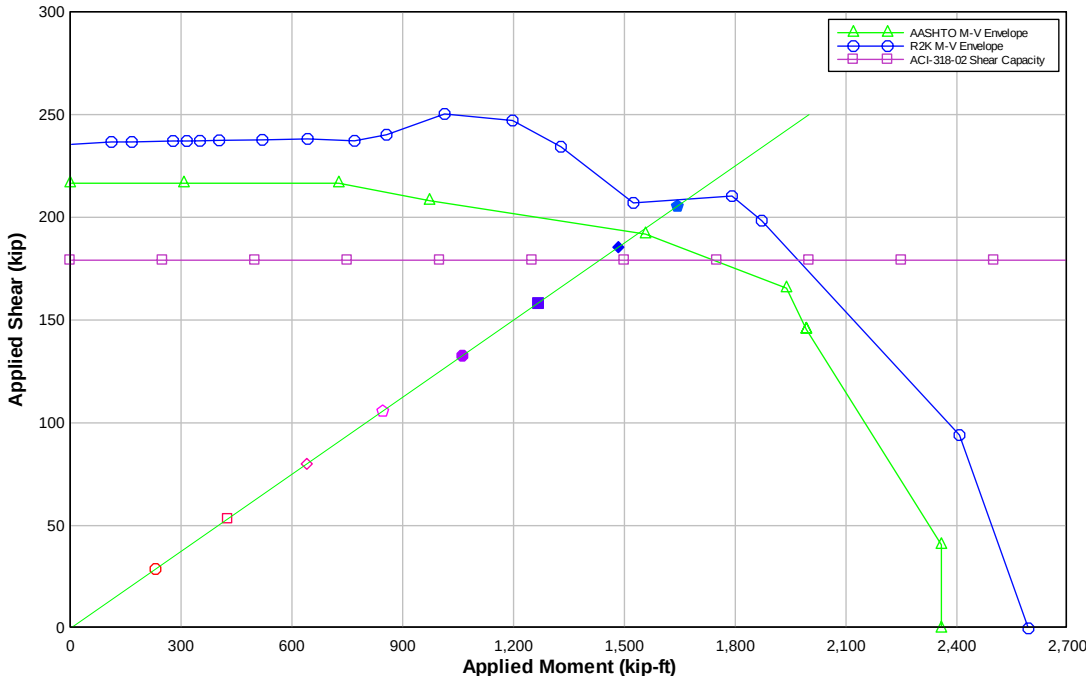

Figure 6.66: Shear-moment interaction diagram for left-hand side of Specimen C11IT16-B1-ML 8 feet from cut section located at face of support.

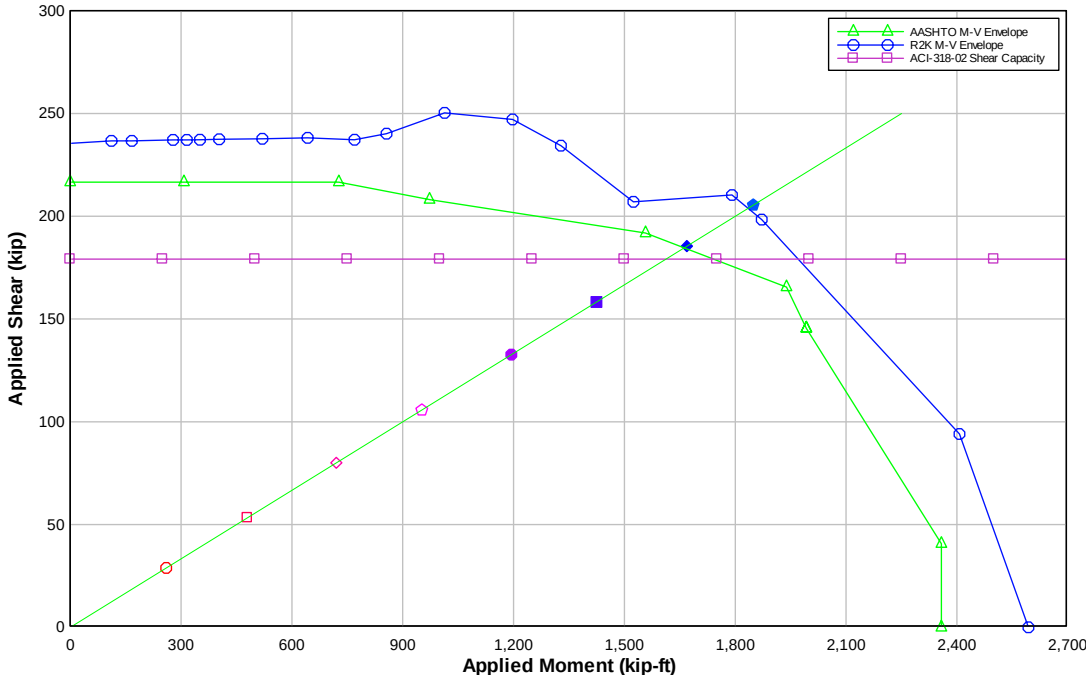

Figure 6.67: Shear-moment interaction diagram for left-hand side of Specimen C11IT16-B1-ML 9 feet from cut section located at face of support.

6.3 COMPARISON OF MOVING LOAD AND STATIONARY LOAD SPECIMEN CAPACITIES

A quantitative analysis of moving load shear-moment capacity was performed by comparing the ratio of peak applied shear to predicted shear for five previously tested monotonic specimens, presented in Chapter 3, the moving load control specimen (Specimen C11IT16-B1-ML) and the three moving load specimens that failed in combined shear-flexure (Specimens C11T16.5-B2-ML, C11T22-B3-ML and C11T22-B4-ML). Shear capacities were predicted using Response 2000™, MCFT and ACI 318-02. The results are compiled in Table 6.1.

Table 6.1: Statistical analysis of moving load shear-moment capacities. The ratio of peak applied shear to predicted shear was compared for five previously tested monotonic specimens, the moving load control specimen(C11IT16-B1-ML) and three moving load specimens using Response 2000™, MCFT and ACI 318-02.

Specimen	f'_c (psi)	V_{APP} (kips)	S (in)	M/V (ft)	V_{ACI1} (kips)	V_{R2K} (kips)	V_{AASHTO} (kips)	V_{APP}/V_{ACI1}	V_{APP}/V_{R2K}	V_{APP}/C_{MCFT}
Monotonic Specimens										
1T18	4925	169.8	18	7.58	134.5	171.5	151	1.26	0.99	1.12
1IT18	4550	158.8	18	7.44	136.9	176.4	157	1.16	0.90	1.01
2T10	3550	205.3	10	7.58	160.9	212.2	178	1.28	0.97	1.16
2T12	3520	192.9	12	7.58	145.9	197.1	164	1.32	0.98	1.18
3T18	3970	153.3	18	7.58	125.8	166.0	144	1.22	0.92	1.06
							Mean	**1.25**	**0.95**	**1.11**
							SD	0.055	0.034	0.060
11IT16 – Monotonic Control Specimen										
5’	4635	205.4	10.5	5.0	179.1	209.4	189	1.15	0.98	1.09
6’	4635	205.4	10.5	6.0	179.1	212.4	197	**1.15**	**0.97**	**1.04**
7’	4635	205.4	10.5	7.0	179.1	209.2	196	**1.15**	**0.98**	**1.05**
8’	4635	205.4	10.5	8.0	179.1	208.9	192	1.15	0.98	1.07
9’	4635	205.4	10.5	9.0	179.1	203.8	185	1.15	1.01	1.11
							Mean	1.15	0.98	1.07
							SD	0.0	0.015	0.029
							Interpolated Values @ Crack Midheight	**1.15**	**0.98**	**1.05**
Moving Load Specimens										
11T16.5										
1’	4970	254.1	8	5.2	207.2	259.2	230	1.23	0.98	1.10
2’	4970	253.4	8	4.3	207.2	273.5	236	1.22	0.93	1.08
3’	4970	252.6	8	3.3	207.2	264.3	239	**1.22**	**0.96**	**1.06**
4’	4970	251.7	8	2.3	207.2	256.3	236	1.21	0.98	1.07
							Mean	1.22	0.96	1.08
							SD	0.005	0.026	0.020
							Interpolated Values @ Crack Midheight	1.22	0.96	1.06
11T22-B3										
3’	4470	216.3	10.5	6.0	174.5	213.3	199	1.24	1.01	1.09
4’	4470	215.5	11.9	5.0	174.5	219.2	204	1.23	0.98	1.06
5’	4470	214.9	14.6	4.0	155.8	211.5	184	**1.38**	**1.02**	**1.17**
6’	4470	213.8	16	3.0	143.7	167.3	170	1.49	1.28	1.26
							Mean	1.34	1.07	1.14
							SD	0.122	0.138	0.090
							Interpolated Values @ Crack Midheight	1.38	1.02	1.17
11T22-B4										
1’	4750	205.3	10.5	8.0	174.5	211.6	191	1.18	0.97	1.08
2’	4750	203.6	10.5	7.0	174.5	207.7	195	1.17	0.98	1.04
3’	4750	202.6	10.5	6.1	174.5	213.0	199	**1.16**	**0.95**	**1.02**
4’	4750	201.8	10.5	5.1	174.5	218.8	204	**1.16**	**0.92**	**0.99**
5’	4750	200.8	16	4.1	155.9	211.9	185	1.29	0.95	1.09
							Mean	1.24	0.99	1.08
							SD	0.094	0.090	0.068
							Interpolated Values @ Crack Midheight	1.16	0.94	1.00
							Mean	**1.25**	**0.97**	**1.08**
							SD	**0.114**	**0.043**	**0.084**

Response 2000™ provided the best prediction of monotonic and moving load shear-moment capacities. The mean applied-shear-to-predicted-shear ratio for the moving load specimens was 0.97, compared to 0.98 for the moving load control specimen, and 0.95 for the monotonic specimens. All data groups had low standard deviations. While Response 2000™ tended to slightly overpredict (non-conservative) the shear capacities of all three data groups, the mean applied-shear-to-predicted-shear ratios for the moving load specimens and moving load control specimen were reasonably close to 1.0 and are similar to one another. Response 2000™ tended to over predict (non-conservative) the shear capacity of the monotonic specimens by about 5%. MCFT consistently provided a conservative estimate of capacity for all data groups. The mean applied-shear-to-predicted-shear ratios of 1.08 for the moving load specimens and 1.05 for the moving load control specimen are similar. MCFT tended to under predict the capacity of the monotonic specimens, a difference of about 3% from the moving load and control specimen.

ACI 318-02 greatly underestimated (conservative) the shear capacities of all three data groups. ACI 318-02 resulted in an average applied-shear-to-predicted-shear ratio of 1.24 for moving load specimens, compared to 1.15 for the moving load control specimen and 1.25 for the monotonic specimens.

6.4 CRACK MOTION

Diagonal crack motions in the moving load specimens were observed to differ significantly from the crack motions observed in the monotonically loaded control specimen. In the control specimen, cracks continually increased in width as the applied load increased, with the majority of crack motion occurring transverse to the direction of the crack. This observation is consistent with previously tested monotonic specimens. In the moving load specimens, the moving load was seen to compress the diagonal cracks as the load approached, as shown in Figure 6.68. The compression of the cracks forced the crack faces into bearing. As the load passed both transverse and longitudinal crack motions were observed, with the crack faces remaining in bearing. The interlocking of the crack features appeared to resist the longitudinal crack motion, as evident by the spalled surface features and raveling in Figure 6.68(c) and Figure 6.68(d). The observed crack motion indicates the presence of aggregate interlock across diagonal cracks subjected to moving loads.

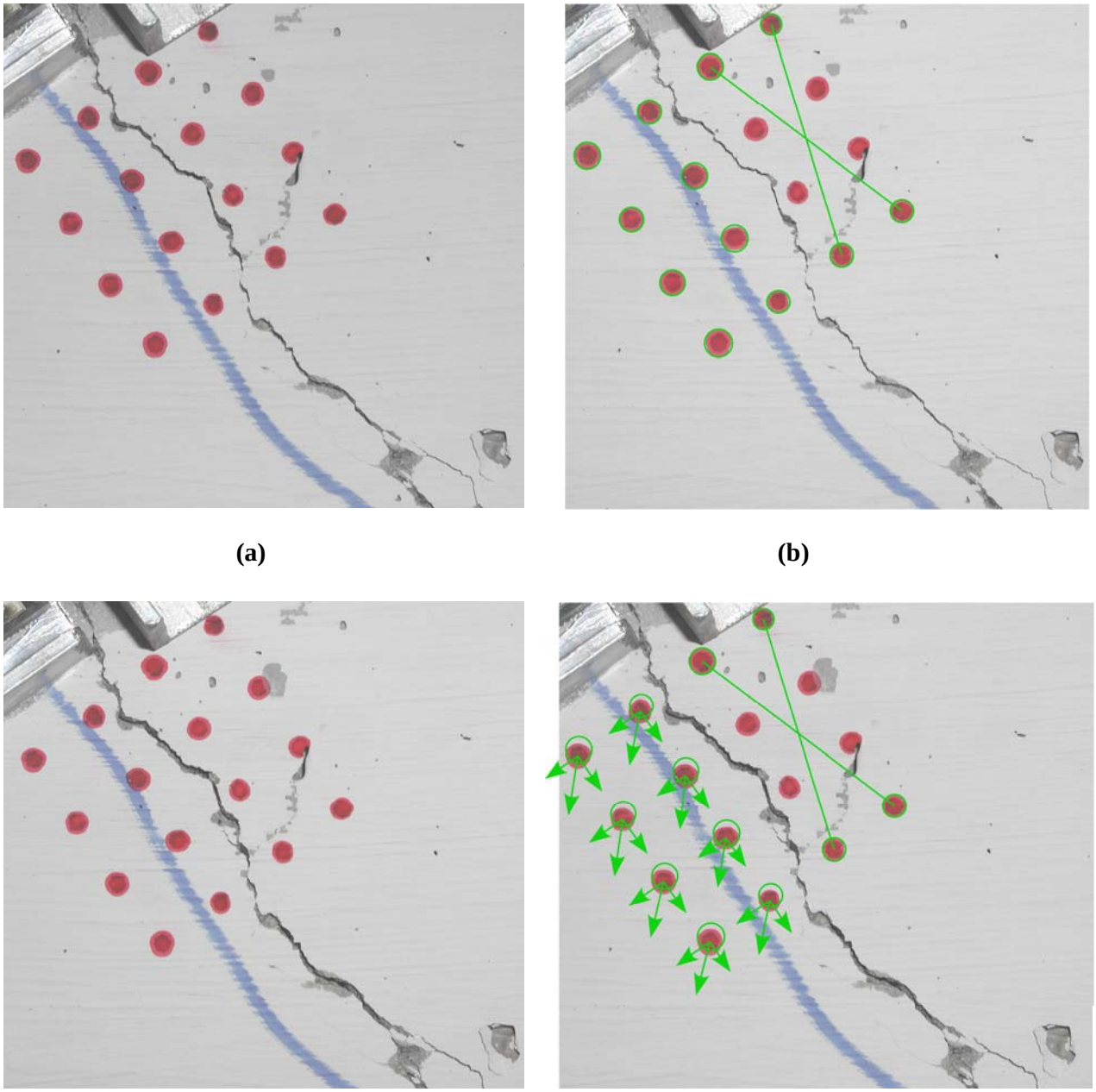

Figure 6.68: Shear crack motion under moving load. (a) Initial crack position. (b) Crack compression as the moving load approaches the test position. Crack features are forced into bearing. (c) Transverse and longitudinal crack motion as the load moves away from the test position. Note the spalling along points of bearing. (d) Final crack position at the end of live load travel. Green arrows denote relative crack motion parallel and transverse to the crack.

6.5 STIRRUP COMPRESSION DUE TO MOVING LOADS

Examples of the strain behavior of stirrups in the moving load specimens and exposed stirrups in an existing CRC deck-girder bridge are shown in Figure 6.69. In general, stirrups in the moving load specimens underwent significant strain reversal (but not necessarily into the compressive range) as the moving load approached the stirrup location, followed by tensile strain once the load passed the crack tip. This is consistent with the crack motions observed above. The laboratory observation is also consistent with stirrup behavior observed in the field, except that the laboratory specimens produced strain reversals of much greater magnitude. Considering only elastic strain data, laboratory stirrup strain reversal values were observed in the range of 40% to 90% of the total elastic stirrup strain at each load step compared to 8% to 15% of the total elastic stirrup strain measured in the field.

Stirrup strain reversal was observed in both embedded and exposed stirrups, although the magnitude of strain reversal was more pronounced in the exposed gages. In general, stirrup strain reversal is a function of the proximity of cracking, crack width, live load magnitude, live load position, load distribution and the redistribution of stresses resulting from progressive cracking.

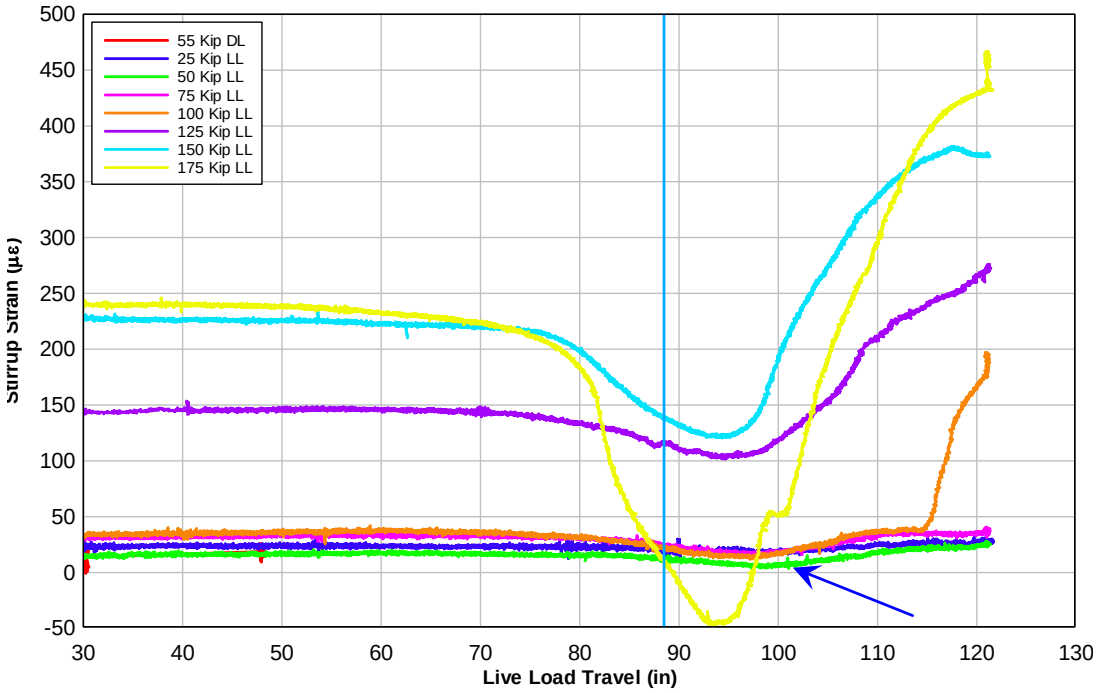

(a)

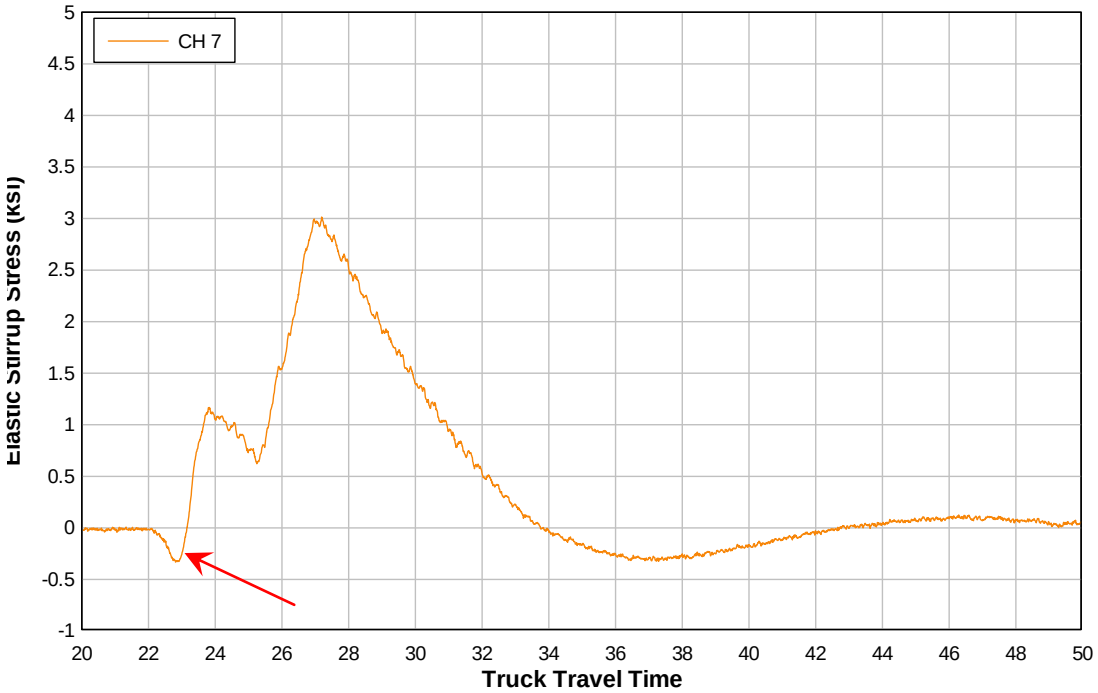

(b)

Figure 6.69: Moving load stirrup behavior in **(a)** a moving load specimen subjected to loads of increasing magnitude, and **(b)** an existing bridge subjected to ambient truck traffic. Stirrup compression accounted for 8% to 15% of the total elastic stirrup strain measured in the field (red arrow) and 40% to 90% of the total elastic stirrup strain measured in the laboratory (blue arrow).

7.0 CONCLUSIONS

A research program was conducted to evaluate structural performance of simulated RCDG bridge girders subjected to moving loads. Responses were compared with tests and analysis developed from stationary loading. Analyses were performed using four different methods to predict specimen shear-moment capacities. The analyses included: Response 2000™, MCFT, ACI 318-02 and Strut-and-Tie. The experimental and predicted shear-moment capacities of specimens were compared. Based on the laboratory tests and companion analyses, the following conclusions are made:

- CRC girders subjected to moving loads exhibited different cracking patterns than those subjected to stationary loading. Cracks on girder specimens subjected to moving loads tended to be more vertically oriented, more widely spaced.
- Application of laboratory moving loads can produce load effects in CRC girders that are more representative of that found in real bridge girders subjected to truck loads than those produced by stationary loading.
- Sectional analysis requires computation of capacity interactions at multiple sections to assess capacity for moving loads.
- Response 2000™ reasonably predicted the shear-moment capacity of CRC girder specimens subjected to moving loads for locations away from disturbed regions.
- Shear-moment values imposed on CRC specimens exceeded the capacity envelope predicted by Response 2000™ on one or more sections without inducing failure.
- AASHTO LRFD (MCFT) provided a conservative estimate of the shear-moment capacity of CRC girder specimens subjected to moving loads away from disturbed regions.
- ACI 318-02 provided an overly conservative estimate of the shear capacity of CRC girder specimens subjected to moving loads at all sections.
- The strut and tie models considered, provided conservative estimates of shear capacity in CRC girders in regions with shear-to-moment ratios below 2. The strut and tie capacity prediction was greatly improved with foreknowledge of the failure mode.
- There was no significant difference between the ultimate capacity of CRC girders subjected to stationary loads and those subjected to moving loads.
- Moving loads produced longitudinal motions along diagonal cracks that were equal to or greater than the observed transverse motion. These crack motions may enhance aggregate interlock at diagonal cracks.
- Moving loads can produce live load strain reversals in stirrups that may increase the range of strain for fatigue considerations as compared with stationary loading.

8.0 REFERENCES

ASTM A305-50T, (1950a). "Tentative Specifications for Minimum Requirements of the Deformations of Deformed Steel Bars for Concrete Reinforcement," ASTM, Philadelphia, PA.

ASTM A15-50T, (1950b). "Tentative Specifications for Billet-Steel Bars for Concrete Reinforcement," ASTM, Philadelphia, PA.

ASTM A16-50T, (1950c). "Tentative Specifications for Rail Steel Bars for Concrete Reinforcement," ASTM, Philadelphia, PA.

ACI 318-02, (2002). "Building Code Requirements for Structural Concrete," American Concrete Institute, Farmington Hills, Michigan.

AASHTO LRFD, (2003). "LRFD Bridge Design Specifications" 2nd Edition with Interims, AASHTO, Washington, D.C.

AASHTO, (2002). "Standard Specification for Highway Bridges" 17th Edition, AASHTO, Washington, D.C.

Bentz, E., (2000). "Sectional Analysis of Reinforced Concrete Members," Ph.D. Thesis, Department of Civil Engineering, University of Toronto.

Higgins, C., Yim, S.C., Miller, T.H., Robelo, M.J., and Potisuk, T., (2004). "Remaining Life of Reinforced Concrete Beams with Diagonal-Tension Cracks," *Report No. FHWA-OR-RD-04-12*, Federal Highway Administration, Washington, D.C.

Kawaguchi, M., "Experiment Relating to Fatigue Strength of Model Reinforced Concrete Beams with Respect to Running Load," Papers on Structural Engineering, Vol. 38A (1992), pp. 1265-1274.

Tadashi, A., "Effects of Running Load on Flexural Load-Carrying Capacity of Reinforced Concrete Beams and Dynamic Effects," Transactions of the Japan Concrete Institute, Vol. 22 (2000), pp. 345-352.

Tadashi, A., "Experimental Research Relating to the Effect of Running Loads on the Flexural Load-Carrying Capacity of Reinforced Concrete Beams," Concrete Journal, Annual Symposium Papers, Vol. 21, No. 3 (1999), pp. 211-216.